

Timo Juuti

THE PRECIPITATION OF
LAVES PHASE AND ITS
CONTRIBUTION TO
MECHANICAL PROPERTIES
IN NOVEL HIGH-CR FERRITIC
STAINLESS STEELS

UNIVERSITY OF OULU GRADUATE SCHOOL;
UNIVERSITY OF OULU,
FACULTY OF TECHNOLOGY



ACTA UNIVERSITATIS OULUENSIS
C Technica 741

TIMO JUUTI

**THE PRECIPITATION OF LAVES
PHASE AND ITS CONTRIBUTION
TO MECHANICAL PROPERTIES
IN NOVEL HIGH-CR FERRITIC
STAINLESS STEELS**

Academic dissertation to be presented with the assent of the Doctoral Training Committee of Technology and Natural Sciences of the University of Oulu for public defence in Auditorium L2 Linnanmaa, on 2 October 2020, at 13 p.m.

UNIVERSITY OF OULU, OULU 2020

Copyright © 2020
Acta Univ. Oul. C 741, 2020

Supervised by
Professor David Porter

Reviewed by
Professor Amaia Iza-Mendia
Associate Professor Silvia Barella

Opponents
Doctor Niilo Suutala
Associate Professor Silvia Barella

ISBN 978-952-62-2565-4 (Paperback)
ISBN 978-952-62-2566-1 (PDF)

ISSN 0355-3213 (Printed)
ISSN 1796-2226 (Online)

Cover Design
Raimo Ahonen

PUNAMUSTA
TAMPERE 2020

Juuti, Timo, The precipitation of Laves phase and its contribution to mechanical properties in novel high-Cr ferritic stainless steels.

University of Oulu Graduate School; University of Oulu, Faculty of Technology

Acta Univ. Oul. C 741, 2020

University of Oulu, P.O. Box 8000, FI-90014 University of Oulu, Finland

Abstract

Titanium-niobium dual stabilized ferritic stainless steels used in high-temperature applications can undergo microstructural changes affecting the steel's properties, such as yield strength and creep resistance. Microstructure evolution in such steels has been simulated both numerically, using the thermodynamic software Thermo-Calc, and physically, using a Gleeble thermomechanical simulator and conventional furnace heat treatments with peak temperatures from 450 to 1050 °C for up to 120 hours.

Thermodynamic simulations for high temperatures predicted the precipitation of MX type carbides and carbonitrides containing Nb and Ti, as well as intermetallic Laves (η), Chi (χ) and sigma (σ) phases. After heat treatments, depending on the temperature and time, all of the above phases apart from χ -phase were found. The composition and morphology of the η -phase was analysed from extracted and in situ particles. It was identified as hexagonal $(\text{FeCrSi})_2(\text{MoNb})$ with either plate-like or equiaxed morphology depending on whether or not the particle had an orientation relationship with the matrix.

The effect of precipitation on yield stress at ambient temperature and at 600 °C was investigated through a breakdown of the strengthening mechanisms such as solid solution and precipitation strengthening. Yield stress at ambient temperature increased as a result of heat treatment at 600 °C due to precipitation strengthening. However, the effect was the opposite regarding the yield stress at 600 °C, due to the different temperature sensitivity of the strengthening mechanisms. The solid solution strengthening coefficient of Nb in α -Fe needed for the calculations was estimated using analysis of literature data to be 16 MPa / at.%.

The experimental results together with comprehensive numerical simulations were used to design a new type of steel with excellent creep resistance at very high temperatures. It is based on the optimal precipitation of the η -phase achieved by alloying Nb, Si and Mo to raise the solvus temperature of the η -phase and results in dispersion strengthening and/or grain boundary pinning, depending on the dominant creep mechanism. The validity of the new approach was confirmed by the use of high-temperature sag tests, which showed that the new steel composition gave significantly better results than can be obtained with commercially available ferritic stainless steels.

Keywords: creep resistance, ferritic stainless steel, high-temperature applications, intermetallic phases, Laves-phase, precipitation, thermodynamic simulations

Juuti, Timo, Laves faasin erkautumisen vaikutus uusien korkeakromisten ferriittisten ruostumattomien terästen mekaanisiin ominaisuuksiin.

Oulun yliopiston tutkijakoulu; Oulun yliopisto, Teknillinen tiedekunta

Acta Univ. Oul. C 741, 2020

Oulun yliopisto, PL 8000, 90014 Oulun yliopisto

Tiivistelmä

Korkeissa lämpötiloissa käytettävät titaanilla ja niobilla stabiloidut ferriittiset ruostumattomat teräkset altistuvat käyttökohteissaan mikrorakenteen muutoksille, jotka voivat vaikuttaa teräksen ominaisuuksiin, kuten myötölujuuteen sekä virumiskestoan.

Mikrorakenteen muutoksia kyseisissä teräksissä on tässä työssä simuloitu numeerisesti Thermo-Calc mallinnusohjelmistolla, fysikaalisesti Gleeble laitteistolla, sekä perinteisellä uunilla 450 – 1050 °C lämpötiloissa jopa 120 tuntia kestäneillä lämpökäsittelyillä.

Mallinnuksen tulokset ennustivat MX tyypisten Nb ja Ti sisältävien karbidien, karbonitridien sekä Laves (η), Chi (χ) ja sigma (σ) -faasien erkautumisen. Lämpökäsittelyjen aikana lämpötilasta ja pitoajasta riippuen teräkseen erkaantui kaikkia yllämainittuja faaseja, paitsi χ -faasia. η -faasin koostumus ja morfologia analysoitiin in situ -partikkeleista sekä teräksestä syövyttämällä irrotetuista partikkeleista. η -faasin kiderakenne on analyysin perusteella heksagonaalinen ja koostumus $(\text{FeCrSi})_2 (\text{MoNb})$. Partikkelit olivat partikkelin ja matriisin orientaatio-suhteesta riippuen joko levyjäisiä tai tasa-akisia.

Erkautumisen vaikutusta myötölujuuteen huoneenlämpötilassa ja 600 °C lämpötilassa tutkittiin jakamalla myötölujuus eri lujitusmekanismeihin, kuten liuoslujittamiseen sekä erkaumalujittamiseen, ja tarkastelemalla mekanismeja erikseen. Huoneenlämpötilassa mitattu myötölujuus nousi lämpökäsittelyissä tapahtuneen erkautumisen ja siitä seuranneen erkautumislujittamisen vuoksi. 600 °C lämpötilassa erkautumisen vaikutus myötölujuuteen oli kuitenkin päinvastainen lujitusmekanismien erilaisen lämpötilariippuvuuden vuoksi. Liuoslujittamisen arvioimiseen tarvittiin niobin lujituskerroin, joka määritettiin kirjallisuudesta saadun datan perusteella olevan 16 MPa / at. %.

Kokeellisesti mitattuja sekä mallinnuksella saatuja tuloksia käytettiin uudenlaisen, korkeisiin lämpötiloihin soveltuvan ja virumiskestoltaan erinomaisen teräksen kehittämiseen. Teräksen hyvä virumiskesto perustuu η -faasin optimaaliseen erkautumiseen seostamalla oikeassa suhteessa niobia, piitä sekä molybdeenia. Seostus nostaa η -faasin liukenemislämpötilaa, sekä lisää erkautumislujittamista ja/tai raerajalukitsemista riippuen virumismekanismista. Virumiskeston todettiin parantuneen korkean lämpötilan Sag testien perusteella. Kehitetyn teräksen Sag testin tulokset olivat huomattavasti parempia verrattuna muihin saatavilla oleviin korkean lämpötilan käyttökohteissa tyypillisesti käytettäviin teräksiin.

Asiasanat: erkautuminen, ferriittiset ruostumattomat teräkset, korkean lämpötilan sovellukset, Laves-faasi, metallien väliset faasit, termodynaaminen mallinnus, virumiskesto

Omistettu Reealle, Liisille ja Saimille

Acknowledgements

This thesis was carried out in the Materials and Mechanical Engineering research unit of the Centre of Advanced Steel Research (CASR) at the University of Oulu between 2011 and 2019. The research was funded by the Finnish Funding Agency for Technology and Innovation (Tekes) under the Demanding Applications program and Breakthrough Steels Applications (BSA) of the Finnish Metals and Engineering Competence Cluster (FIMECC Ltd.), and by Companhia Brasileira de Metalurgia e Mineração and the Academy of Finland through project #311943. The experimental materials used in the research were provided by Outokumpu Stainless Oyj. The research was also supported by grants awarded by Tauno Tönningin säätiö, Riitta ja Jorma Takasen säätiö, Jenny ja Antti Wihurin rahasto, Metallinjalostajien säätiö, Tekniikan edistämissäätiö and Oulun Yliopiston tukisäätiö.

I would like to acknowledge all those who have expressed their support and guided me during these years. I have also been fortunate to be surrounded by several experts for whose contribution I am grateful. I would like to thank my supervisor, Professor David Porter, for the long-lasting collaboration, his valuable comments, guidance and perceptive observations regarding my research topic. I would also like to thank Professor Emeritus Pentti Karjalainen and Professor Jukka Kömi for supporting my pursuit of the doctoral degree. The research was done in collaboration with Outokumpu Stainless Oyj from where I would especially like to thank Mr. Timo Manninen for sharing the interest and dedication towards the topic of this thesis. I want to express my thanks to Professor Amaia Iza-Mendia and Associate Professor Silvia Barella for the pre-examination of the thesis and their comments and suggestions. I also wish to thank Doctor Ludovica Rovatti for the TEM analysis and contribution to two of the articles.

For the supportive work environment and valuable comments, I thank my former colleagues at the Materials and Mechanical Engineering Research Group including Mr. Ilpo Alasaarela and Mr. Tun Tun Nyo, who were also involved in the research via technical support in workshop and sample preparation. I want to present special thanks to Doctor Antti Kaijalainen for our enlightening conversations over the years whether at the Research Group or at the Squash court.

The biggest thanks are devoted to my parents and family, especially my wife Reea and my two lovely daughters, for their continuous support and encouragement.

Oulu, August 2019

Timo Juuti

Abbreviations and symbols

α -Fe	ferrite
β^*	rate at which atoms attach to the critical nucleus
γ	interface energy
γ -Fe	austenite
ΔE_s	energy of solution in a multicomponent system
ΔG	free energy change
ΔG^*	Gibbs energy for formation of critical nucleus
ΔG_m	molar free energy change
ΔG_v	Gibbs chemical free energy
ΔG_e	misfit strain energy
ε	micro strain
ζ	half-width of the dislocation
η	Laves Phase
κ	Boltzmann constant
λ	the interplanar spacing
μ	shear modulus
ρ	dislocation density
σ	sigma phase
σ_d	dislocation strengthening
σ_i	friction stress
σ_{ppt}	precipitation strengthening
σ_{ss}	solid solution strengthening
σ_y	yield strength
τ	incubation time for steady state nucleation
τ	shear stress
φ	scaling factor for solid solution strengthening
χ	chi phase
ω_p	friction energy
a	lattice parameter
A	aspect ratio
b	Burgers vector
B	bowing force
c	lattice parameter
C	concentration of a solute

d	grain size/material density
D	diffusion coefficient
f	volume fraction
g	acceleration of gravity
J_s	steady state nucleation rate
k	geometrical constant for Williamson & Hall eq.
K	solid solution strengthening coefficient
k_y	Hall-Petch coefficient
L	spacing between particles
L_c	crystallite size
M	Taylor factor
n	material factor for Williamson & Hall eq.
N_A	Avogadro number
n_s	atoms per unit area at the interface
N_0	number of nucleation sites
R	gas constant
r^*	critical embryo radius
R_{eH}	upper yield point
$R_{p0.2}$	yield stress at 0.2% plastic strain
t	thickness of sample
T	temperature
T_d	line tension of a dislocation
T_m	melting point
v	Poisson's ratio
V_m	molar volume
x	diameter of particles on the plane of intersection
X	true particle diameter
X_i	mole fraction of element i
Z	Zeldovich factor
z_s	number of bonds per atom crossing the interface

AOD	Argon-oxygen decarburization
at. %	atomic percent
avg.	average
b.c.c.	body centred cubic
BSE	backscatter electron
CNT	classical nucleation theory

DSA	dynamic strain aging
ECD	estimated circle diameter
e.g.	exempli gratia
EDS	energy dispersive spectroscopy
etc.	et cetera
f.c.c.	face centred cubic
FESEM	field emission scanning electron microscope
FP	fundamental parameter
h.c.p.	hexagonal close-packed
HR-TEM	high resolution transmission electron microscope
i.e.	id est
JCPDS	joint committee on powder diffraction standards
SOFC	solid oxide fuel cell
STEM	scanning transmission electron microscopy
TEM	transmission electron microscopy
VOD	vacuum-oxygen decarburization
WPPF	whole powder pattern fitting
wt.%	weight percent
XRD	X-ray diffractometer

List of original publications

This thesis is based on the following publications, which are referred throughout the text by their Roman numerals:

- I Juuti, T.J., Karjalainen, L.P., & Heikkinen, E.-P., (2012) Precipitation of Si and its influence on mechanical properties of type 441 stainless steel, *Advanced Materials Research*, 409, 690-695.
- II Juuti, T., Karjalainen, P., Rovatti, L., Heikkinen, E.-P. & Pohjanne, P. (2011) Contribution of Mo and Si to laves-phase precipitation in type 444 steel and its effect on steel properties, In *Proceedings: 7th European Stainless Steel Conference – Science and Market, Como, Italy 21 – 23.9.2011* Associazione Italiana di Metallurgia AIM.
- III Juuti, T., Rovatti, L., Mäkelä, A., Karjalainen, L.P., & Porter D., (2014) Influence of long heat treatments on the laves phase nucleation in a type 444 ferritic stainless steel, *Journal of Alloys and Compounds*, 616, 250-256.
- IV Juuti, T., Rovatti, L., Porter, D., Angella, G., & Kömi, J., (2018) Factors controlling ambient and high temperature yield strength of ferritic stainless steel susceptible to intermetallic phase formation, *Materials Science and Engineering A*, 726, 45-55.
- V Juuti, T., Manninen, T., Uusikallio, S., Kömi, J., & Porter, D., (2019) New ferritic stainless steel for service temperatures up to 1050 °C utilizing intermetallic phase transformation, *Metals*, 9(6), 664.

The author of this work has been the main and corresponding author of all the publications. He has been responsible for the planning of the research and analytical work as well as executing the experiments, excluding Factsage-software calculations for Paper I and II, TEM examinations for Paper II, III and V, the electrochemical polarization measurements for Paper II, STEM examinations in Paper IV and Gleeble annealing for Paper V.

In Paper I, the precipitation of silicon in ferritic stainless steel EN1.4509 is investigated. Precipitation of silicon containing intermetallic Laves-phase (η) was promoted with heat treatments at temperatures between 450 and 800 °C and predictions for the precipitations calculated with Factsage-software using Scientific Group Thermochemical Europe database (SGTE). However, the SGTE database does not include Si as an element of the η -phase and only considered η -phase with the compositions of Fe_2Nb and Fe_2Mo in the calculations. The equilibrium diagrams are recalculated in chapter 4.1 using Thermo-Calc software with TCFE9 database for more comprehensive data on η -phase.

Paper II continues the research on η -phase precipitation on another ferritic stainless steel, type EN1.4521. The Mo alloying in the steel results in Mo bearing

η -phase during heat treatments above 650 °C. The Mo addition increased the volume fraction of the η -phase substantially.

In Paper III, the $(\text{FeCrSi})_2(\text{MoNb})$ type η -phase is analysed and characterized in detail. The crystal structure was determined as hexagonal and morphology characterized as either equiaxed or plate-like, depending on whether or not the particle had an orientation relationship with the matrix, i.e. whether the particle nucleated during the heat treatment or was already present in the as-received material.

Paper IV addresses the influence of the η - and σ -phases on the ambient and high temperature yield strength through a comprehensive breakdown of the mechanisms contributing to strengthening, i.e. grain boundary, dislocation, precipitation and solid solution strengthening. The nucleation and growth of the precipitation was also calculated using Thermo-Calc and TC-Prisma software. The calculated isopleth diagram showed overestimation of the range of carbon content in which Chi-phase precipitates. The issue was fixed in a later version of Thermo-Calc and is recalculated in chapter 4.1.

Paper V describes the process of designing a new heat resistant ferritic stainless steel utilizing the precipitation of η -phase. Previously gathered knowledge as well as both thermodynamic and Gleeble simulations, was used to select optimal alloying composition and annealing parameters to promote sufficient precipitation of η -phase on grain boundaries for enhanced creep resistance at very high temperatures up to 1050 °C.

Contents

Abstract

Tiivistelmä

Acknowledgements 9

Abbreviations and symbols 11

List of original publications 15

Contents 17

1 Introduction 19

1.1 Applications of ferritic stainless steels..... 19

1.2 Ferritic stainless steels used in high temperature applications..... 20

1.3 η -phase in high-Cr ferritic stainless steels 20

1.4 Objectives of the research 21

2 Theoretical framework 23

2.1 Ferritic stainless steels 23

2.1.1 Alloying of Ti and Nb in ferritic stainless steels 25

2.1.2 Alloying of Mo and Si in ferritic stainless steels..... 26

2.2 Precipitation in ferritic stainless steels 27

2.2.1 Nucleation, growth and dissolution 27

2.2.2 Niobium and titanium carbonitrides 34

2.2.3 η -phase and other intermetallic phases 35

2.3 Yield strength of ferritic stainless steels..... 36

2.3.1 Friction stress and Hall-Petch effect..... 37

2.3.2 Solid solution strengthening 37

2.3.3 Precipitation strengthening 38

2.3.4 Strengthening owing to dislocations..... 40

2.4 Creep resistance 41

3 Experimental procedures 45

3.1 Materials 45

3.1.1 Annealing simulations and hot rolling..... 46

3.1.2 Heat treatments 47

3.2 Thermodynamic modelling 47

3.2.1 Thermo-Calc..... 48

3.2.2 TC-Prisma 48

3.3 Microstructural analysis 49

3.3.1 Scanning and transmission electron microscopy 49

3.3.2 X-Ray diffraction..... 50

3.4	Mechanical testing	52
3.4.1	Macro and micro-hardness	52
3.4.2	Tensile tests	53
3.4.3	Sag tests	53
4	Results	57
4.1	Thermodynamic simulations	57
4.1.1	Phase equilibria	57
4.1.2	Kinetics and TTT curves for η -phase	59
4.2	Microstructure analysis	61
4.2.1	Effects of heat treatments	62
4.2.2	Characterization of η -phase	72
4.3	Mechanical testing	76
4.4	Sag tests.....	78
5	Discussion	81
5.1	Precipitation of Nb- and Ti-containing carbonitrides.....	81
5.2	Precipitation of η - and σ -phase	82
5.3	Characterization of η -phase.....	83
5.3.1	Composition of η -phase.....	83
5.3.2	Crystal structure and morphology of η -phase.....	84
5.4	Effect of η -phase on mechanical properties of the steel.....	85
5.4.1	Room temperature yield strength.....	87
5.4.2	High temperature yield strength	88
5.5	Utilizing η -phase to improve high-temperature creep resistance	90
5.5.1	Controlling the precipitation of η -phase	90
5.5.2	Improving creep resistance.....	93
6	Summary and conclusions	95
7	Novel features	99
	List of references	101
	Original publications	109

1 Introduction

1.1 Applications of ferritic stainless steels

High-Cr ferritic stainless steels containing over 18% chromium are designed to replace the more commonly used austenitic grades, especially in kitchen appliances. However, ferritic stainless steels are also used in building materials and many different automobile components. The use of stainless steels in automotive manufacture began with decorative trims but has since spread to more functional components due to the excellent corrosion and heat resistance, desirable appearance and mechanical properties of stainless steels. One of the most demanding components is the exhaust system, where good mechanical properties at a very high temperature, good stress-corrosion resistance as well as good formability are required. In exhaust systems, stainless steels and more recently high-Cr ferritic stainless steels have been replacing conventional cast iron as the most commonly used material, now accounting for more than half of all stainless steel used in automotive applications [1]–[4].

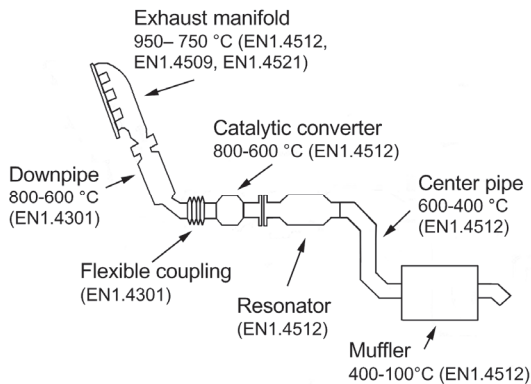


Fig. 1. Schematic illustration of various exhaust system parts and service temperatures (redrawn from [2], [5]).

Parts fabricated with ferritic stainless steels are lighter compared to cast iron and therefore lower the vehicle weight. However, ferritic stainless steel also matches better with the requirements of increasing service temperatures, which are the result of tightened exhaust gas regulations and producer warranties, but also allow automotive manufacturers to decrease fuel consumption. These requirements are

further emphasized in the parts of exhaust systems that are closest to the engine and therefore susceptible to the highest temperatures and most demanding conditions (Fig. 1). To continue the development of high demand applications, more knowledge on the microstructure changes taking place in ferritic stainless steels at high temperatures is required, and it is one of the key motivations of this research.

1.2 Ferritic stainless steels used in high temperature applications

The austenitic stainless steel EN1.4301 (ASTM type 304) has excellent high-temperature strength but weak cyclic oxidation resistance, while the ferritic stainless steel EN1.4512 (409) has inferior high-temperature strength. To replace these, EN1.4509 (S43940) and EN1.4521 (444) type high-Cr, Nb-Ti-stabilized ferritic stainless steels have been introduced and used because of their superior high temperature properties. EN1.4521 alloyed with Mo and Si is a candidate material for high temperature applications due to its low cost, good mechanical properties and high corrosion resistance. However, this steel lacks the properties needed in parts directly attached to the engine that can be susceptible to temperatures up to 1050 °C [1]–[4], [6]–[8].

In new high-Cr ferritic stainless steels, such as EN1.4509 and EN1.4521, the mechanical and corrosion properties are improved by alloying Ti, Nb and Mo to better address the requirements of high-temperature applications.

1.3 η -phase in high-Cr ferritic stainless steels

In addition to carbides and nitrides, the addition of alloying elements such as Nb, Si and Mo can lead to precipitation of intermetallic phases such as Laves (η), Chi (χ) and sigma (σ) phases, with very different precipitation kinetics compared to carbides and nitrides. The nucleation and coarsening of MX type carbonitrides has typically begun to saturate when the steel is in the as-delivered state. Intermetallic phases have much slower kinetics and may precipitate only after exposure to high temperatures for prolonged periods, such as those experienced in exhaust systems, making it more difficult to estimate the high-temperature mechanical properties of the steel.

The utilization of η -phase to improve high-temperature properties and creep resistance of martensitic pipeline steels has drawn interest in the past few decades. However, the use of it in ferritic stainless steels is less explored [9]–[12]. In addition, materials susceptible to the precipitation of η -phase are considered for solid oxide

fuel cell (SOFC) applications, which operate at temperatures above 600 °C. In SOFC applications, η -phase can be used to deplete the Si in the matrix, thereby preventing the formation of electrically resistive Si-rich oxide subscales [13]–[15].

1.4 Objectives of the research

The effect of intermetallic phases on strengthening at room temperatures, but especially in high temperatures, still requires clarification due to the many different variations of intermetallic phases and variables that affect yield strength in stainless steels. The challenge in understanding how intermetallic phase precipitation affects the yield strength of the steel at high temperature can be due to the precipitation of strong solid solution strengthening components like Si, and because the precipitation strengthening also depends on the shear modulus and Burgers vector, which are temperature dependent [16]–[19]. A further difficulty is due to the lack of studies on solid solution strengthening in α -Fe by Nb, which is needed to estimate the strength owing to Nb alloying and possibly its decrement as a result of the precipitation of intermetallic phases containing Nb, i.e. the η -phase [20], [21].

The key objective of this research is to fully understand the precipitation of η -phase in high-Cr ferritic stainless steels and its effect on the mechanical properties of the steel, and to use this knowledge to design a new ferritic stainless steel for high-temperature applications up to 1050 °C.

2 Theoretical framework

2.1 Ferritic stainless steels

Ferritic stainless steels typically contain 11 to 30 wt.% of chromium. The required Cr content is determined by the γ -loop, which in binary Fe-Cr system extends to 13 wt.% Cr (Fig. 2). Above 13 wt.% Cr, the structure is body centred cubic (b.c.c.) α -Fe from ambient to solvus temperature. Also, Cr content above 10.5% is required to form a sufficiently stable and self-healing oxide film on the surface, necessary for the corrosion resistance of stainless steels. The γ -loop can be suppressed by alloying ferrite stabilizing elements such as titanium, silicon and niobium. In contrast, the γ -loop will be extended by alloying interstitial atoms carbon and nitrogen, or other austenite stabilizing elements, such as nickel and manganese.

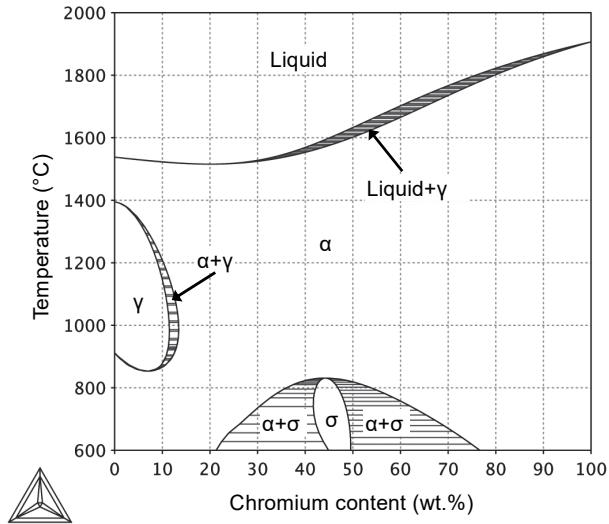


Fig. 2. The Fe-Cr equilibrium phase diagram calculated with Thermo-Calc.

The stabilizing effect of the alloying elements can be expressed in terms of a nickel equivalent if the element stabilizes austenite, or a chromium equivalent if it stabilizes ferrite:

$$\begin{cases} Ni_{eq} \text{ (wt. \%)} = Ni + Co + 30C + 25N + 0.5Mn + 0.3Cu \\ CrCr_{eq} \text{ (wt. \%)} = Cr + 2Si + 1.5Mo + 5V + 5.5Al + 1.75Nb + 1.5Ti + 0.75W \end{cases} \quad (1)$$

The equivalents are used, for example in the Schaeffler diagram that presents the microstructure achieved after rapid cooling typically from 1050 °C to room temperature (Fig. 3). The interstitial amount is typically kept as low as possible to avoid formation of carbides, nitrides and carbonitrides.

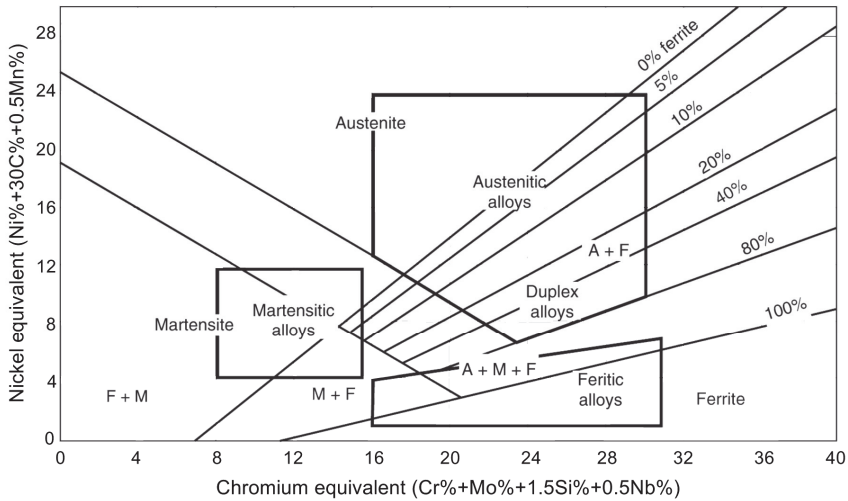


Fig. 3. Schaeffler diagram for stainless steels with typical composition ranges of austenitic, martensitic, ferritic and duplex alloys superimposed (redrawn from [22]).

The level of carbon and nitrogen is, however, usually determined by the melting technology used in the process, i.e. whether the decarburization is carried out using argon-oxygen decarburization (AOD) or vacuum-oxygen decarburization (VOD). The VOD process can reduce the carbon levels to below 0.02 wt.%. When the carbon level in 18 wt.% Cr steel is kept below 0.04 wt.%, the steel is fully ferritic in all temperatures. Higher carbon levels of 0.08 wt.% to 0.22 wt.% can lead to partial ($\alpha+\gamma$) structures.

The absence of phase transformations in stabilized ferritic stainless steels results in fewer options for grain refinement. As grain refinement is no longer possible to be achieved as a result of phase transformations during heat treatments, it can, in fact, cause rapid grain coarsening. These steels are susceptible to grain coarsening, for example, in welding. A large grain size is undesirable for several reasons, including the formability and high temperature strength of the steel, even

though it can have a beneficial effect on creep resistance. The grain size can be refined by finishing the hot rolling below the recrystallization temperature, or by cold rolling followed by recrystallization annealing. This will result in large rolling reductions, which is partly the reason why ferritic stainless steels are typically used as sheets rather than thicker plate. On the other hand, the lack of a phase transformation is also the reason why ferritic stainless steels are well suited for high temperature applications. In addition to rapid grain growth, ferritic stainless steels are also susceptible to “475 °C -embrittlement” [23], [24], which can have a negative effect on the formability of the steel and raise the ductile-to-brittle transition. When exposed to prolonged heat treatments in temperatures close to 475 °C, Cr-rich alpha prime (α') and Fe-rich α -phases precipitate due to the miscibility gap in the Fe-Cr equilibrium phase diagram (Fig. 2). The precipitation only occurs in compositions with over 12 wt.% of chromium, and the kinetics increase as the Cr content increases. The temperature window in which the phases precipitate is small, and the solvus temperature is around 550 °C, so the phenomena can be avoided or removed by heating the steel accordingly and then water quenching to room temperature.

2.1.1 Alloying of Ti and Nb in ferritic stainless steels

In addition to the ferrite stabilizing properties discussed in the previous chapter, Nb and Ti also provide other benefits when alloyed. As a highly reactive element, titanium is often alloyed in order to deplete the microstructure from interstitial atoms C and N by forming Ti-containing MX type nitrides and carbonitrides, such as the very stable TiN. The sufficient ratio of Nb and Ti to interstitial atoms C and N is ~ 3.7 [25]. The precipitation of C and N eliminates the formation of Cottrell atmospheres, i.e. the phenomenon where clusters of C and N react strongly with the strain fields around dislocations, as first shown by Cottrell and Bilby [26], [27]. The Cottrell atmosphere can be seen as a sharp transition between elastic and plastic deformation, called the upper yield point R_{cH} in the stress-strain curve, and can occur even in concentrations as low as 0.005 wt.%. The appearance of an upper yield point can be detrimental to formability and continuous yielding behaviour [26], [27]. Another reason to alloy Nb and Ti is to prevent the interstitials from precipitating as Cr-containing carbonitrides, resulting in Cr depleted zones and decreasing the corrosion resistance of the steel. In addition, the precipitation can also have a positive effect on the yield strength of the steel through dispersion strengthening if the particles remain small. Although at the same time, the

precipitation reduces the strengthening effect of Ti and Nb in solid solution [4], [28]. Ti is also alloyed in small concentrations for welding purposes to promote the formation of equiaxed grains without a loss of ductility [23], [28], [29]. The amount of Ti required to stabilize the steel is dependent on the C and N content and is typically calculated as $\text{Ti (wt.\%)} \geq 0.2 + 4(\text{C} + \text{N})$. However, the excess alloying of Ti can lead to surface defects, which require an additional process phase of surface grinding, increasing the total production costs [23], [30].

To overcome these issues and to improve the high temperature strength of high-Cr ferritic stainless steels, titanium is often coupled with niobium [30]. Nb behaves in same way as Ti by binding the free interstitials into carbides and carbonitrides, or, when in solution, by strengthening the steel via solid solution strengthening effect [31]. For Nb to contribute to the solid solution strengthening of the steel, the precipitation of Nb-containing carbides and carbonitrides and intermetallic phases, such as η -phase, needs to be controlled and understood, so that enough Nb is left for solution. However, controlled precipitation of η -phase can have other beneficial effects on high temperature properties. Nb can also suppress recovery and recrystallization, and it limits the grain growth. The increase of recrystallization temperature is due to the effect of Nb on grain boundary mobility. The temperature is increased probably due to the solute drag effect of Nb when in solution or when precipitated as carbides, nitrides or intermetallic phases due to the pinning effect of fine particles, especially if they are distributed on grain boundaries [32], [33].

Campbell et al. have shown that when alloying high amounts of Nb, the steel may become susceptible to grain boundary segregation, leading to hot cracking in the welds [24]. Optimum toughness and ductility of welds in ferritic stainless steels is achieved with 17 wt.% of chromium or more with a ratio of 1:2 between Ti and Nb. Optimal limits for Ti and Nb have been experimentally determined as follows:

$$\begin{cases} \text{Ti} + \text{Nb (wt. \%)} \geq 0.2 + (\text{C} + \text{N}) \\ \text{Ti} + \text{Nb} \leq 0.8 \end{cases} \quad (2)$$

The amounts of niobium and titanium in dual stabilized steels are a compromise between the increase of transition temperature via titanium stabilization and increase of impact toughness via niobium stabilization [30].

2.1.2 Alloying of Mo and Si in ferritic stainless steels

Another typical element used in alloying ferritic stainless steels is silicon. Silicon is used for its steelmaking properties as a deoxidizer and to improve the fluidity of

the melt. A typical amount of Si alloyed in ferritic steels is 0.3 wt.% to 0.6 wt.%. Silicon is also used to improve oxidation resistance in steels susceptible to high temperatures [31]. Si increases the activity of carbon and, in the presence of iron, Si does not form carbides [34]. In more recent studies on the role of Si, Hironaka et al. [35] suggested Si alloying to increase the formation of dislocation cells and thereby increasing work hardening rate and yield strength.

Especially in ferritic stainless steels used in high-temperature applications with corrosion resistance equivalent to that of austenitic stainless steels, molybdenum is alloyed. Molybdenum will enhance the passive layer and adjacent transition layer, notably improving the pitting and crevice corrosion resistance [36], [37]. Si and Mo both contribute to the solid solution strengthening of the steel, with Si having a more significant effect on the yield strength. Similarly to Nb and Ti, the alloying of Mo and Si also promotes the formation of intermetallic phases, especially σ - and η -phases.

2.2 Precipitation in ferritic stainless steels

Although the $\alpha \rightarrow \gamma$ transformation does not occur in stabilized ferritic stainless steels, there are other thermally activated phase transformations, namely precipitation reactions, that take place in ferrite due to the metastable supersaturated solid solution. In the next chapter, the principles of precipitation as well as the precipitation typical in ferritic stainless steel is described.

2.2.1 Nucleation, growth and dissolution

The precipitation reaction results in the formation of a phase with a different composition compared to that of the matrix and therefore it requires long-distance diffusion. For nucleation to happen, the atoms in the precipitating phase need to diffuse together and reorder into the crystal structure of the precipitate if needed. This leads to the formation of an interface between the matrix and the precipitate, which leads to a nucleation energy barrier. After the nucleation, the total free energy

change ΔG related to the nucleation barrier will decrease by the amount of nucleation barrier, i.e. maximum ΔG value (Fig. 4).

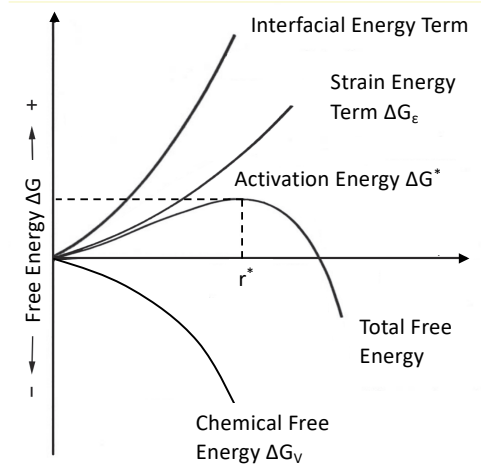


Fig. 4. Free Gibbs energy change related to the nucleation of precipitates (redrawn from [38]).

The change in free energy is calculated as a sum of chemical free energy change ΔG_V , surface free energy and misfit free energy as follows [38]:

$$\Delta G = \frac{4}{3}\pi r^3 \Delta G_V + 4r^2 \gamma + \frac{4}{3}\pi r^3 \Delta G_\epsilon, \quad (3)$$

where ΔG_V is the Gibbs chemical free energy change per unit volume ($\Delta G_V \leq 0$) of the new phase, γ is the energy per unit area of the interface between the two phases, ΔG_ϵ is the misfit strain energy per unit volume of precipitate and r is the radius of the embryo. r^* is the critical radius where the free energy change is at a maximum ΔG^* . The misfit energy ΔG_ϵ is caused by the coherency strains produced by the change of composition and crystal structure. The volume free energy change ΔG_V is given by:

$$\Delta G_V = \frac{\Delta G_m}{V_m}, \quad (4)$$

where V_m is the molar volume of precipitate β and ΔG_m the molar free energy change for the formation of the precipitates, which can be obtained via CALPHAD method [39], [40]. Differentiating Eq. 3 then gives the critical radius as:

$$r^* = \frac{2\gamma V_m}{\Delta G_m} \quad (5)$$

and

$$\Delta G^* = \frac{16\pi\gamma^3}{3(\Delta G_m)^2} . \quad (6)$$

Embryos smaller than r^* are unstable and can dissolve spontaneously. The time necessary to form an embryo larger than the critical radius, i.e. the supercritical radius, is typically described as the incubation time τ .

Eq. 3 considers the nucleation as homogeneous where the nucleation can occur anywhere in the matrix with equal probability. It is typical in steels that the nucleation is heterogeneous and will take place on non-equilibrium defects, such as grain boundaries, dislocations or stacking faults where the interfacial energy and, in case of dislocations, the misfit strain energy is lower, decreasing the nucleation barrier compared to that of a homogeneous nucleation site. The nucleation energy barrier and incubation time for nucleation will depend on the energy of the site in question, i.e. the incubation time will be shortest for grain corners, followed by grain edges then grain boundaries etc. [38].

Interfacial Energy

The interface between two solid phases with different crystal structures and/or compositions, i.e. the boundary between precipitate and the matrix, can be of three different types: i) coherent, ii) semi-coherent and iii) incoherent (Fig. 5). A coherent interface is where the crystal structure of the two phases match perfectly so that the lattice from one phase to another is continuous. A coherent interface can be formed only between phases with the same atomic configuration and specific orientation relationship. Therefore, the energy of a coherent interface is only the result of the wrong chemical bonding across the interface compared with the bulk. Consequently, coherent interfaces have relatively low energies, between 1 and 200 mJ/m². Small differences in the interatomic distances across the interface, i.e. misfit, can be accommodated by coherency strains in the precipitate and matrix. If the strain increases enough it will become energetically favourable to transform the coherent interface to a semi-coherent one, where the misfit strain is accommodated by misfit dislocations.

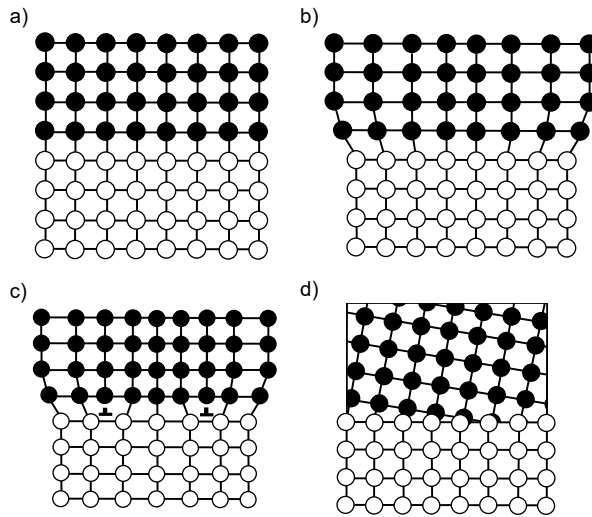


Fig. 5. schematic illustration of the different atomic configurations at a) perfectly coherent, b) coherent with coherency strain, c) semi-coherent, d) incoherent interfaces (redrawn from [38]).

The strain fields of the misfit dislocations are localised at the interface, giving semi-coherent interfaces an extra energy component in addition to the chemical contribution. This typically results in interfacial energies between 200 mJ/m^2 and 500 mJ/m^2 . The interface can also be incoherent, as happens in the case of very different atomic configurations between the two solid phases. When the interatomic distances are more than 25% different between the phases or the pattern of atoms is very different then the interface may be called incoherent. These interfaces generally have high interfacial energy above 500 mJ/m^2 . The interface between the two phases can change from coherent to semi-coherent during the precipitation as the precipitate grows. The interfacial energy has a significant contribution to the kinetics of the precipitation, i.e. the nucleation, growth and coarsening of the particles [38].

Precipitate nucleation rate

Classical nucleation theory (CNT) describes the time dependent nucleation rate defined as:

$$J(t) = J_s \exp\left(\frac{\tau}{t}\right), \quad (7)$$

where J_s is the steady state nucleation rate, t is the isothermal reaction time and τ is the incubation time for establishing steady state nucleation conditions. The steady state nucleation rate is described as:

$$J_s = Z\beta^* N_0 \exp\left(-\frac{\Delta G^*}{\kappa T}\right), \quad (8)$$

where Z is the Zeldovich factor which describes the probability with which an embryo with a radius slightly larger than the critical radius passes back across the free energy barrier, thereby dissolving in the matrix, ΔG^* is the Gibbs energy for the formation of a critical nucleus, N_0 is the number of nucleation sites per unit volume, κ is Boltzmann's constant, T is the absolute temperature and β^* is the rate of atoms attaching to the critical nucleus, given by [41]:

$$\beta^* = \frac{4\pi r^{*2}}{a^4} \left[\sum_{i=1}^k \frac{(X_i^{\beta/\alpha} - X_i^{\alpha/\beta})^2}{X_i^{\alpha/\beta} D_i} \right]^{-1}, \quad (9)$$

where a is the lattice parameter, $X_i^{\beta/\alpha}$ is the mole fractions of element i at the interface in the precipitate and $X_i^{\alpha/\beta}$ in the matrix, and D is the diffusion coefficient of the element i in the matrix. The number of nucleation sites depends on the shape and size of the grains. Assuming all grains are equal sized tetrakaidekahedrons, the area of grain boundary per unit volume is given by

$$\rho = \frac{6\sqrt{1+2A^2+1+2A}}{4A} D^{-1}, \quad (10)$$

where A is the aspect ratio, i.e. the length of the x - and y -axis divided by the length of the z -axis of the tetrakaidekahedron, and D is the distance between one pair of hexagonal faces. Assuming boundary thickness as one atomic layer, the number of nucleation sites is

$$N = \rho \left(\frac{N_A}{V_m^\alpha} \right)^{\frac{2}{3}}, \quad (11)$$

where V_m^α is the molar volume of the matrix phase and N_A is the Avogadro-number [41], [42].

Precipitate growth

When precipitate β has a different composition to that of the matrix α , growth of β in supersaturated α requires the long-range transport of solute elements and is

therefore, usually, diffusion controlled, as shown in the illustration in Fig. 6. A depleted area of solute element will appear around the growing precipitate because of the concentration of the solute in the precipitate C_β being higher than in the matrix C_α . If the interface is mobile, the composition in the matrix at interface C_e can be assumed to be that in local equilibrium with β . Growth of the precipitate requires the excess solute in the precipitate ($C_\beta - C_e$ and the interstitial diffusion coefficient D as following [38]) to be supplied by the flux of solute through the matrix towards the interface. Equating these two gives [38]:

$$v = \frac{dx}{dt} = \frac{D}{C_\beta - C_e} \times \frac{dc}{dx}, \quad (12)$$

where D is the diffusion coefficient and dC/dx the concentration gradient in the matrix at the interface. As the precipitate grows, the solute is depleted from the matrix, decreasing dC/dx with time. According to Zener's approach on precipitate growth, dC/dx is given by $(C_\alpha - C_e)/L$ where L is the width of the diffusion zone determined by two equal areas shown in Fig. 7 as $(C_\beta - C_\alpha)x = L(C_\alpha - C_e)/2$, where x is the slab thickness. The growth rate is thereby:

$$v = \frac{D(C_\alpha - C_e)^2}{2(C_\beta - C_e)(C_\beta - C_\alpha)x}. \quad (13)$$

When the diffusion zones (Fig. 7) overlap, the equation above will not apply, and the growth will decelerate until the composition everywhere in the matrix is equal to the composition at the interface. That is when the growth ceases. The precipitate growth rate is highly dependent on the temperature and supersaturation of the solid solution, as shown in Fig. 8. At temperatures slightly below solvus (T_e), the diffusion rate may be high, but the supersaturation is low, resulting in slow growth rate and vice versa. If the temperature is low then the supersaturation is high, but the diffusion rate is also low, leading again to a slow growth rate. The highest growth rate is achieved at some temperature between these two conditions.

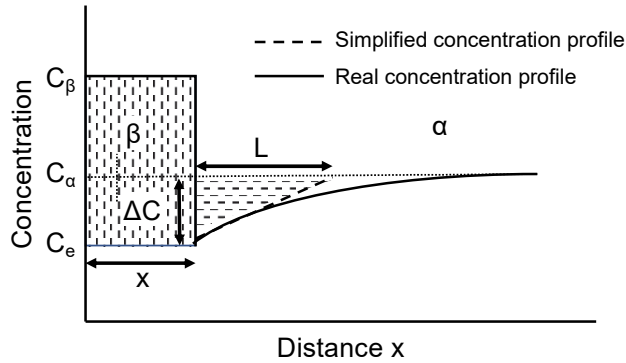


Fig. 6. Schematic illustration of diffusion controlled growth of precipitates (redrawn from [38]).

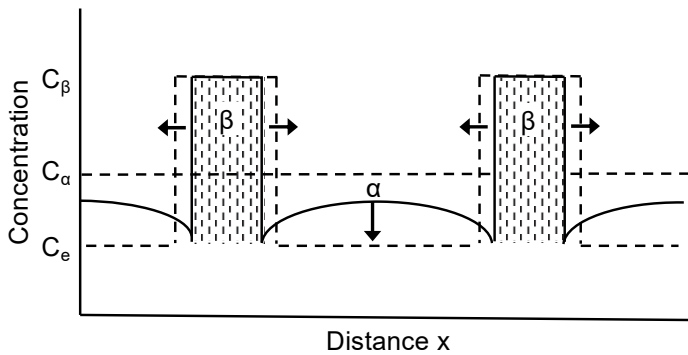


Fig. 7. Interference of growing precipitates due to overlapping diffusion fields (redrawn from [38]).

Coarsening of precipitates

The coarsening of precipitates is generally considered to be the final stage of precipitation in which the total volume fraction of the phase no longer increases over period of time, but the precipitate size continues to grow. The coarsening of the precipitates can be calculated using Ostwald ripening theory derived from the classical LSW coarsening and supersaturation theory by Lifshitz, Slyosov and Wagner, where smaller precipitates dissolve and larger ones coarsen. The LSW coarsening rate is given by:

$$r^n - r_0^n = \frac{8\gamma V_m^\beta D C_\alpha}{9RT} t, \quad (14)$$

where r_0 is the initial precipitate radius, r is the average precipitate radius, V_m^β is the molar volume of phase β , C_α is the equilibrium solute composition of the matrix, R is the gas constant, T is the temperature in Kelvin and t is the holding time at T . For intragranular precipitates, the coarsening is controlled by bulk diffusion and the factor n is 3. The above equation is only valid for coarsening taking place in the matrix. The precipitates in grain boundaries can also coarsen through two-dimensional diffusion of solute atoms along the grain boundary, in which case the equation would require modifications.

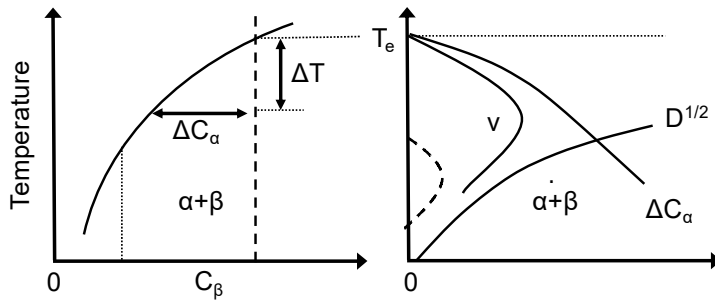


Fig. 8. Effect of temperature and supersaturation on the growth rate and coarsening of particles (redrawn from [38]).

2.2.2 Niobium and titanium carbonitrides

In Nb and Ti dual stabilized ferritic stainless steels, the Nb and Ti can form MX type carbides, nitrides and carbonitrides, where M represents the metallic atoms, e.g. Nb and Ti, and X the interstitials C and N. The following stoichiometric ratios apply in the case of pure Ti or Nb carbides:

$$\begin{cases} \text{Ti} : 12\text{C (at. \%)} \text{ or } 4\text{Ti} : 1\text{C (wt. \%)} \\ \text{Nb} : 12\text{C (at. \%)} \text{ or } 8\text{Nb} : 1\text{C (wt. \%)} \end{cases} \quad (15)$$

However, C can be partly or fully replaced by N, and Nb and Ti are mutually soluble, forming the carbonitrides $(\text{Ti}_a\text{Nb}_b)(\text{C}_c\text{N}_d)$. In such a case, the relative amounts of the elements depend on the concentrations represented by a, b, c and d. $(\text{TiNb})(\text{CN})$ precipitates are rather stable, forming at relatively high temperatures. Any excess alloying of Nb or Ti relative to that required to form $(\text{TiNb})(\text{CN})$ is initially left in

solution and is available to form other precipitates at lower temperatures, e.g. the intermetallic η -phase. The lattice structure of MX type precipitates is face centred cubic (f.c.c.). Typical MX type precipitates in high-Cr ferritic stainless steels are angular Ti-containing carbonitrides and NbTi -carbides [8], [43]–[45].

2.2.3 η -phase and other intermetallic phases

According to the Fe-Cr equilibrium phase diagram shown in Fig. 2, σ -phase can be present in the equilibrium microstructure at temperatures below 830 °C in steels with a Cr content above 20 wt.%. However, the critical Cr level is decreased when other substitutional elements such as Mo, Ni and Si are alloyed. The composition of σ -phase is typically FeCrSi, but Mo can replace Si as is the case in EN1.4521 type ferritic stainless steel with 18 wt.% of Cr and 2 wt.% of Mo. In EN1.4521 the Cr window has decreased enough for σ -phase to precipitate in temperatures below 620 °C, as seen in Fig. 19. When alloying elements other than Cr are present, intermetallic phases such as η - and χ -phase can form. The exact steel composition affects the temperature window and solvus temperatures of the intermetallic phases, as shown by Murata et al. in the case of η -phase [46]. The formation of Cr and Mo rich χ - and σ -phases can decrease the corrosion resistance of the steel by depleting Cr and Mo from the matrix adjacent to precipitates. Some studies suggest that during a prolonged ageing χ -phase can transform into σ -phase [47]–[50].

η -phases are intermetallic phases with AB_2 lattice structure, where the atomic radius of element A is bigger than the atomic radius of element B, such as Mg_2Zn or Fe_2Nb . However, η -phase may include other alloying elements such as Cr, Si and Mo as well. The η -phase is stabilized by the size factor for atomic size ratios $r_a : r_b$ in the range of 1.05 to 1.68 [51], [52]. η -phases in ferritic steels are typically hexagonal close packed structures (type C14) with unit cells in the range of $a = 0.473$ – 0.495 nm and $c = 0.770$ – 0.815 nm with $c : a$ ratio close to 1.633 [53], [54].

The effect of η -phase precipitation on the properties of ferritic stainless steels have been reported but are slightly controversial. It has been reported that the precipitation of Fe_2Nb -type η -phase can reduce of the toughness of the steel, especially at room temperature [8], [55], [56]. In further research, Fujita et al. [4] observed an increase in the high-temperature yield strength after precipitation of the same phase, whereas Morris et al. [57] observed a decrease in the high-temperature yield strength, which was, however, mainly due to the coarsening of the η -phase. Sim et al. [56] made a similar observation as Morris et al. and suggested that Fe_2Nb coarsens faster than NbC because of a coherency difference.

It should be noted that Si and Mo are potent solid solution strengtheners (in addition to Nb) and therefore the precipitation of these alloys, especially as coarse particles where dispersion strengthening does not apply, could lead to decreased strength. Experimental data regarding these effects is, however, lacking as the compositions of the η -phase and the matrix and the magnitudes of other strengthening factors vary [8], [56], [58].

The order in which the secondary phases occupy the nucleation sites can influence the evolution of the mechanical properties of the steel and thereby limit the service temperature. The η -phase has been observed to nucleate first on grain boundaries, presumably first on grain corners, grain edges and finally grain boundaries, then on dislocations and finally in the matrix [59]. For nucleation to take place on dislocations, at least one interface plane should have rather good matching between the precipitate and the matrix, i.e. creating a coherent or semi-coherent interface so that the interfacial energy is low enough for nucleation [38]. The coherence of η -phase and α -Fe has been studied, but the results are contradictory. Cocks et al. observed plate-like Fe_2Nb particles with a unique orientation relationship between Fe_2Nb and the ferritic matrix [60]. Cottrell and Turnbull suggested that the η -phase nucleates on the tension side of the dislocations where elements with atomic size larger than iron, such as Nb and Mo, would segregate. Sim et al., however, showed the presence of an incoherent interface between Fe_2Nb with HR-TEM observations [56], [61], [62].

2.3 Yield strength of ferritic stainless steels

The yield strength is typically taken as the offset yield stress $R_{p0.2}$ at 0.2% plastic strain in stress-strain curve obtained as a result of experimental methods such as the tensile test. The yield strength (σ_y) of a steel can also be estimated by calculating the various strengthening components as follows:

$$\sigma_y = \sigma_i + k_y d^{-1/2} + \sigma_{ss} + \sigma_{ppt} + \sigma_d, \quad (16)$$

where σ_i is the friction stress, $k_y d^{-1/2}$ is the Hall-Petch relationship, σ_{ss} is the solid solution strengthening, σ_{ppt} is the precipitation strengthening and σ_d is the dislocation strengthening.

2.3.1 Friction stress and Hall-Petch effect

Friction stress, σ_i is the lattice resistance of a pure metal, i.e. the stress required to move a dislocation along slip planes, and can therefore be considered as the yield strength of a pure single crystal ($d^{-1/2}=0$). Hirth and Lothe [63] have given the expression for friction stress as:

$$\sigma_i = \frac{1}{b^2} \left[\frac{\partial \omega(\alpha)}{\partial \alpha} \right]_{max} = \frac{2\pi\omega_p}{b^2} = \frac{2\mu}{(1-\nu)} \exp\left(\frac{-4\pi\zeta}{b}\right), \quad (17)$$

where ω_p is the friction energy, b is the Burgers vector, ζ is the half-width of the dislocation described as:

$$\zeta = \frac{\lambda}{2(1-\nu)} \quad (18)$$

and λ is the interplanar spacing:

$$\lambda = \frac{a}{\sqrt{h^2+k^2+l^2}}, \quad (19)$$

ν is Poisson's ratio, and μ is the shear modulus. Friction stress is particularly sensitive to temperature, especially in b.c.c. structures, since friction stress depends on the short-range stress field of the dislocation core. In crystal structures with wide dislocations, i.e. f.c.c. structures, friction stress is negligible, whereas in b.c.c. structures with narrow dislocations, friction stress may also be insignificant at high temperatures, but increases rapidly with decreasing temperature, representing a large component of the yield strength at low temperatures [64].

One of the reasons the grain size in ferritic stainless steel is kept reasonably small is to achieve higher yield strength. The first scientific analysis on the relation between grain size and strength was carried out by Hall and Petch on ARMCO iron which led to the Hall-Petch equation, describing the strengthening arising from grain boundaries, $k_y d^{-1/2}$, where d is the grain size and the Hall-Petch coefficient is k_y [65], [66].

2.3.2 Solid solution strengthening

The formation of intermetallic phases can decrease the solid solution strengthening σ_{ss} effect by depleting matrix from alloying elements, but it also contributes to precipitation strengthening σ_{ppt} . Solid solution strengthening is due to the interaction between dislocations and solutes in solid solution. The size of the strengthening effect depends on the size misfit of solute atoms in the matrix

according to the Hume-Rothery size effect, but also on elastic behaviour between the solute and the matrix, as shown by Fleischer [18], [67], [68]. Solid solution strengthening can be one of the reasons for alloying, especially in industrial steels where it may make a significant contribution to overall yield strength. For multicomponent alloys, the change in strength owing to σ_{ss} can be calculated using the following formula by Suzuki and Mott, which has been shown to correlate well with experimental results for b.c.c. metals [18]:

$$\sigma_{ss} = \varphi \sum_i K_i C_i, \quad (20)$$

where φ is a scaling factor dependent on temperature, K_i is the strengthening coefficient in MPa / at.% for alloying element i and C_i is the atomic per cent of the alloying element i in solution.

2.3.3 Precipitation strengthening

Typically, precipitation may occur in all steels during some process stage, as described in chapter 2.2. The matrix already strengthened by the grain size and solid solution additions can be significantly further strengthened by precipitation. Strengthening owing to precipitates, also known as dispersion strengthening, often arises from looping of the dislocations around the precipitates, as described by Orowan [28].

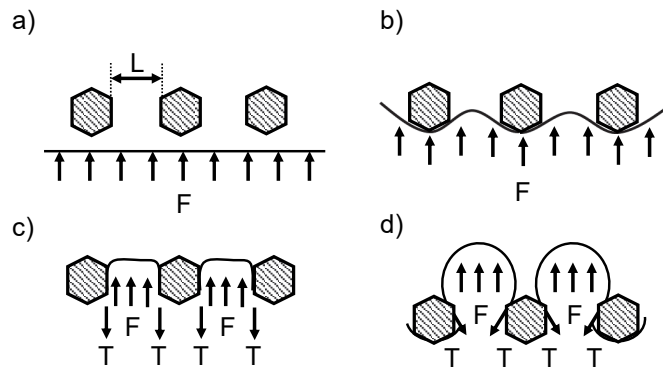


Fig. 9. Dislocation looping around precipitates in a) approach situation, b) sub-critical situation, c) critical situation and e) escape situation (redrawn from [28]).

Other interactions between the dislocations and precipitates are also possible, i.e. dislocations cutting through the second phase particle. However, it has been found that the bowing mechanism is usually able to explain precipitation strengthening in microalloyed b.c.c. steels [28]. According to the basic model of dislocation looping by Orowan (Fig. 9), the line tension of the dislocation is $T_d \approx \mu b^2/2$. If the dislocation movement stops due to precipitated particles it will begin to bow under the bowing force B given by:

$$B = \Delta\tau bL, \quad (21)$$

where L is the spacing between the particles and $\Delta\tau$ is the shear stress difference between the applied shear stress and the stress required to move the dislocation in the absence of particles. This force is balanced by the force exerted by the particles, i.e. $F = 2T_d \sin \theta$. Equating these two gives the Orowan equation:

$$\Delta\tau_y = \frac{\mu b}{L}. \quad (22)$$

Substituting the Orowan equation with volume fraction and converting it to yield strength using the Taylor factor gives:

$$\sigma_{ppt} = \frac{6\mu b \left(\frac{3f}{2\pi}\right)^{1/2}}{X}, \quad (23)$$

where $X = (3/2)^{1/2}x$, the three dimensional, i.e. true particle diameter of the particles, is converted from the diameter x of particles on the plane of intersection. However, this presents an overestimation of the stress required to bypass the particles. The particle spacing is calculated by assuming the dislocation is parallel with one edge of the assumed square array of particles in the slip plane. The effective spacing would, in fact, be increased by a factor of $2^{1/2}$ if the dislocation was parallel with the diagonal of the square. Furthermore, when the particles are in random array, some of the larger spacing offers no resistance to the passage of the dislocations when the stress has reached a level where it would allow bypassing of dislocations on a regular array. Kocks, Foreman and Makin used a computer-based simulation to determine an effective obstacle spacing as circle which can be placed at opposite ends of the diameter without occluding other particles [69], [70]. Ashby considered this effect with the use of interparticle distance instead of centre to centre spacing in Ashby-Orowan equation given as:

$$\sigma_{ppt} = \frac{0.538\mu b\sqrt{f}}{X} \ln \frac{X}{2b} \quad (24)$$

According to Gladman [28], the Ashby-Orowan equation is best suited for microalloyed steels where the precipitate size is negligible compared to the precipitate spacing due to the low volume fractions of precipitates [17]. A comparison of the strengthening contribution from particles between Orowan and Ashby-Orowan is shown in Fig. 10. The Orowan equation indicates a significantly larger increase in yield strength and as described is an overestimation due to the minimum spacing.

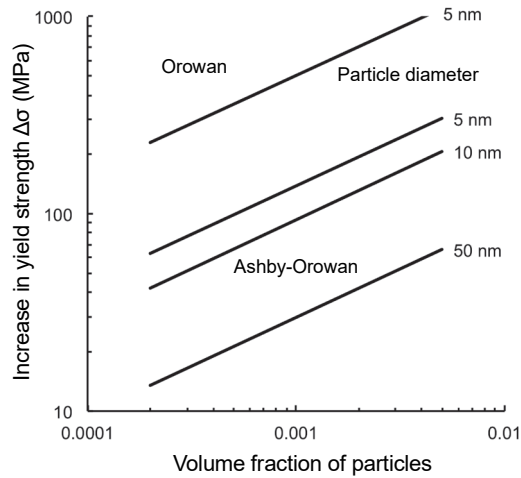


Fig. 10. Increase in yield strength according to Orowan and Ashby-Orowan equations (redrawn from [28]).

2.3.4 Strengthening owing to dislocations

One of the first ones to relate the dislocation density of a material to the flow stress was G.I. Taylor (1934), who developed an equation to describe work hardening. The equation assumes flow stress as external stress required to move two dislocations on parallel slip planes past each other. The maximum shear stress associated with a dislocation is of $\mu b/r$, where r is the distance to the dislocation, and the average spacing between the dislocations is $1/\sqrt{\rho}$ where ρ is the dislocation density. The contribution from dislocation density to the strength σ_d can be described as:

$$\sigma_d = \alpha M \mu b \sqrt{\rho}, \quad (25)$$

where M is the Taylor factor used to convert shear stress to an equivalent uniaxial yield stress, and α is the material constant depending on crystal structure. In literature the equation also exists without the addition of the Taylor factor in which case it is possibly considered in the material constant [71], [72]. The Taylor factor, or the material constant, can also change if the material has a texture or deformation, however only very slightly [73]. Other work hardening models attribute a similar linear relation between flow stress and dislocation density, but with different constants. The Taylor equation has been shown to hold true for f.c.c., b.c.c. and h.c.p. (hexagonal close-packed) metals [74].

2.4 Creep resistance

Creep concerns the time-dependent change in strain under a constant applied load at temperatures above approximately $0.4T_m$, where T_m is the melting point in Kelvins. For many materials, the variation of creep strain with time can be divided into three stages based on creep rate behaviour (Fig. 11). The different creep stages are due to changing interactions between hardening (e.g. the generation of new dislocations) and recovery (e.g. the annihilation of dislocation) [64], [75].

After the initial elastic strain ε^o caused by the application of the load, comes the first so-called transient response stage, where strain rate $d\varepsilon/dt$ decreases with time. The decrease is related to work hardening, i.e. by subgrain formation caused through the rearrangement of dislocations. When the strain has reached ε^l , the creep rate reaches a minimum value and the steady-state creep stage begins. Here, the hardening and recovery processes are almost in balance. Increasing the applied stress or temperature will shorten and ultimately remove the steady-state creep stage. The final stage where the creep rate increases rapidly is the third stage, followed by the failure in rupture life t_R . In this stage the high stress / temperature levels cause the balance to be lost and softening processes and formation of cavities becomes dominant [64], [75], [76].

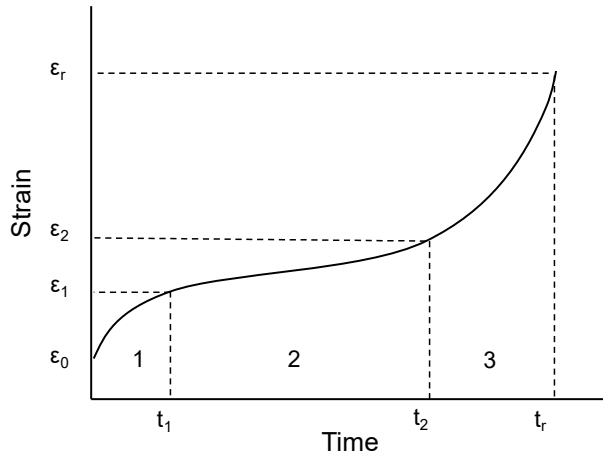


Fig. 11. Three stages of the creep deformation curve (redrawn from [64]).

The dominant creep mechanism during steady-state creep can be estimated using the deformation mechanism map in which the different creep mechanisms are located in normalized stress–temperature space. The creep rate $\dot{\epsilon}$ in the deformation map is shown as a function of homologous temperature T/T_m and shear stress is normalized in respect to the shear modulus. A deformation map for a ferritic steel calculated by Zinkle and Lucas is shown in Fig. 12 [77]. The creep mechanisms considered, from low to high temperature, are plasticity, i.e. dislocation glide, power-law or dislocation creep, and the diffusional creep mechanisms known as Coble creep and Nabarro-Herring creep [78], [79].

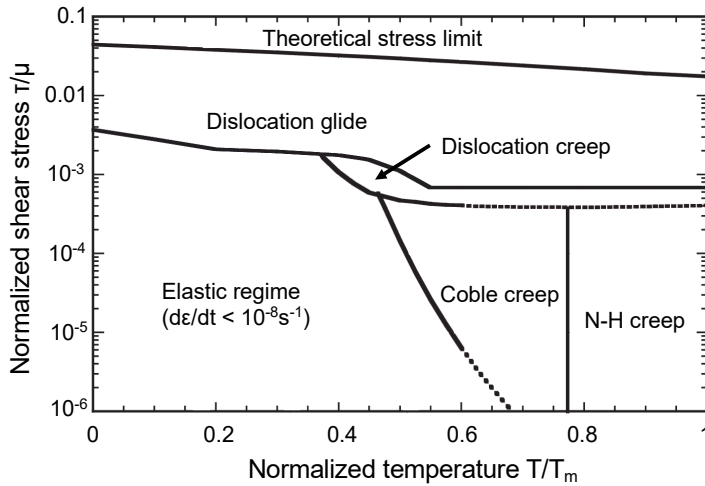


Fig. 12. Calculated deformation map for ferritic-martensitic steel (redrawn from [77]).

When the temperature is above $0.4T_m$ and the stress is sufficiently high, the dislocation glide is assisted by the climbing of the dislocations, i.e. climb-controlled creep or power-law creep begins. The dislocation creep mechanism is based on the diffusion of vacancies to the dislocations, allowing the dislocation to climb over obstacles on the slip plane. Depending on the temperature, the mechanism of creep at lower applied stress and higher temperature involves diffusion-controlled migration of vacancies. At temperatures above $0.5T_m$, the creep is controlled by grain boundary diffusion; this mechanism is called Coble creep. At temperatures above 0.7 (Fig. 12), the creep is controlled by lattice diffusion, and the mechanism is called Nabarro-Herring creep. The creep rate depends on the grain size in such a way that a smaller grain size increases the creep rate. The creep rate in Coble creep is inversely proportional to the cube of the grain size and thereby even more sensitive to the grain size than in Nabarro-Herring creep, where the creep rate is inversely proportional to the square of the grain size [64], [78].

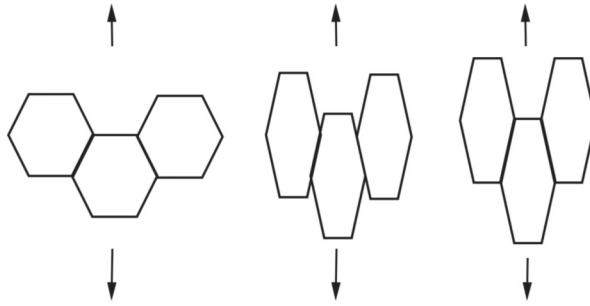


Fig. 13. Elongation and grain separation caused by stress induced diffusional flow accommodated by grain boundary sliding (redrawn from [64]).

Another creep mechanism present in high-temperatures where fine grain size has a negative effect is grain boundary sliding (Fig. 13). However, grain boundary sliding is not an independent mechanism but accommodated by other creep modes, and its effect can be mitigated if the grain boundaries are covered with precipitates [64], [76]. Hertzberg et al. (1989) have studied the overlapping of the mechanisms and suggest that Coble creep is dependent on grain boundary sliding [64].

3 Experimental procedures

This chapter covers the composition and heat treatment parameters of the materials used in this study together with a description of the research equipment and methods used to evaluate the microstructures and mechanical properties of the materials.

3.1 Materials

In all of the papers, Ti and Nb dual-stabilized ferritic stainless steels were studied with a Cr content of 18 and 21 wt.%. The materials were provided as 2 mm thick sheets. The chemical compositions of the materials are presented in Table 1.

Table 1. Chemical composition (wt.%), grain size (ASTM) and η -phase solvus temperature ($^{\circ}\text{C}$) of the investigated steels [Paper I, II, V].

Steel	C	N	Cr	Nb	Ti	Si	Mn	Mo	Cu	Ni	Grain size	η -phase solvus T
EN1.4509	0.018	0.018	17.90	0.38	0.11	0.45	0.50	0.02	0.13	0.37	6.0	820
EN1.4521	0.022	0.023	17.61	0.38	0.12	0.50	0.52	2.02	0.19	0.19	7.8	900
EN1.4622	0.010	0.020	20.80	0.36	0.17	0.48	0.40	0.03	0.36	0.18	8.8	839
High-NbMo-SS	0.020	0.020	21.00	0.80	0.20	0.60	0.30	2.00	0.40	0.20	5.0	1009
Mid-Nb-SS	0.020	0.020	21.00	0.40	0.10	0.43	0.33	0.12	0.40	0.19	6.1	819
High-Nb-SS	0.020	0.020	21.00	0.80	0.20	0.80	0.32	0.02	0.40	0.20	5.0	1009

Type EN1.4509 and EN1.4521 steels were from a conventional production process of ferritic steels, in which the steel was hot rolled to a strip with 4.5 mm thickness at 1050 $^{\circ}\text{C}$ followed by continuous annealing. A first annealing was carried out at ~ 1000 $^{\circ}\text{C}$ followed by water quenching and cold rolling to a 55% reduction. A second annealing was done at ~ 1020 $^{\circ}\text{C}$ followed by temper rolling with a rolling reduction of 0.5% to the final thickness of 2 mm. In Paper V, a new high-Cr ferritic stainless steel was designed, based on three different trial steels (the last three rows in Table 1). The chemical compositions, grain size according to ASTM E 112 standard [80] and the solvus temperatures of η -phase are shown in Table 2.

3.1.1 Annealing simulations and hot rolling

The experimental materials, i.e. the last three in Table 1, were prepared from 65 kg laboratory cast ingots. The cast ingot was reheated to 1100 °C and held for 75 minutes, which is a typical procedure for ferritic stainless steels. After reheating the ingot was hot rolled in 7 passes with a starting temperature of 1160 °C to an end thickness of 6 mm. Hot rolling was followed by cold rolling with a 30% reduction to an end thickness of 4.2 mm. The cold-rolled strips were then pre-annealed and finally cold rolled with a 48% reduction to a final thickness of 2 mm. This was followed by a final annealing to optimize the microstructure of the finished product. A Gleeble 3800 thermomechanical simulator was used to simulate the pre- and final annealing, using different peak temperatures with the aim of optimizing the final microstructure. The heating rate and cooling rate in the Gleeble simulations was matched with an actual industry scale annealing process. The heating curves are shown in Fig. 14.

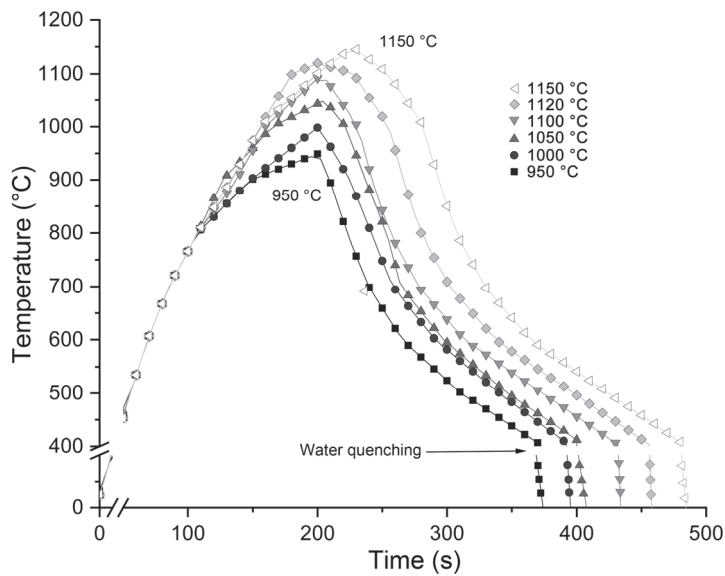


Fig. 14. Heating curves for Gleeble annealing simulations of trial steels (Under CC BY Paper V © 2019 Authors).

3.1.2 Heat treatments

To simulate the high-temperature service, the commercial steels EN1.4509 and EN1.4521 were heat treated at temperatures of 450, 600, 650 and 800 °C for various durations of time up to 120 hours in a convection furnace followed by water quenching. The heat treatments were followed by water quenching to avoid prolonged exposure to the “475 °C -embrittlement” temperature. Another set of EN1.4521 steels were first heat treated at 1050 °C for 24 hours to dissolve all the intermetallic phase particles formed during the earlier processing to obtain a better understanding of the effect of the processing on the nucleation and morphology of precipitation, such as the formation of η -phase during the heat treatments. The heat treatments are summarized in Fig. 15.

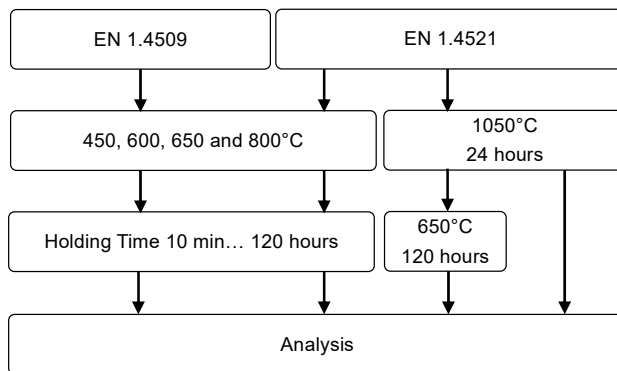


Fig. 15. Heat treatments of the commercial steels EN1.4509 and EN1.4521.

3.2 Thermodynamic modelling

Thermodynamic and phase equilibrium calculations for multicomponent and multiphase systems was carried out using the Thermo-Calc software package based on the CALPHAD method in conjunction with suitable thermodynamic databases. Phase equilibrium calculations were performed to gain better knowledge of the precipitation behaviour in the studied steels, but also in Paper V as part of the alloy design to reduce the time and costs significantly compared to a conventional trial-and-error approach [81], [82]. Two different thermodynamic databases for Fe-based alloys were used: TCFE7 in Papers I to III and TCFE9 in Papers IV and V.

3.2.1 Thermo-Calc

The CALPHAD method applied in Thermo-Calc software is based on calculating the Gibbs energy of a phase as a function of the phase composition as well as temperature and pressure in the system. The CALPHAD method works in conjunction with various databases and interfaces, where all the information regarding the Gibbs energy is stored. A mathematical model containing adjustable parameters is then applied and the parameters evaluated so that the fit of the model is optimized to all the assessed information involving coexisting phases. This allows recalculation of the phase diagram as well as the thermodynamic properties of the system. Therefore, the CALPHAD method obtains consistent information of the phase diagram and the thermodynamic properties to predict the stable phases and thermodynamic properties without any experimental information, in a mathematical way. However, the method is far from simple due to the large number of variables involved in the calculations [42].

3.2.2 TC-Prisma

For calculating nucleation, growth and dissolution of phases, TC-Prisma was used together with kinetic database MOBFE2, which contains mobility data for Fe-based alloys. TC-Prisma simulates diffusion-controlled nucleation, growth and dissolution of precipitates using the Langer-Schwartz theory and the Kampmann-Wagner numerical approach in conjunction with Thermo-Calc and its diffusion-controlled phase transformation module (DICTRA). The classic nucleation theory has been extended in TC-Prisma to model nucleation in multicomponent alloy systems [42]. The maximum driving force and the critical composition are calculated in Thermo-Calc with the aid of a Newton-Raphson method [83].

In Paper IV, the interfacial energy γ is added manually with values taken from the literature: $\gamma^\sigma = 0.35 \text{ J/m}^2$ for σ -phase, $\gamma_\eta = 0.311 \text{ J/m}^2$ for η -phase and $\gamma^{MX} = 0.15 \text{ J/m}^2$ for MX type precipitation [42], [48], [58], [84]. In Paper V, the interfacial energy was calculated with an extended Becker's model using thermodynamic data from the existing CALPHAD thermodynamic database. In this method the interfacial energy is given by

$$\gamma = \frac{n_s z_s}{n_A z_l} \Delta E_s, \quad (26)$$

where n_s is the number of atoms per unit area at the interface, z_l is the coordination number of an atom within the bulk crystal lattice, z_s is the number of bonds per

atom crossing the interface and ΔE_s is the energy of solution in a multicomponent system with the two phases considered.

For the density of nucleation sites in TC-Prisma, grain boundary nucleation was calculated using the measured mean linear intercept grain diameter [42].

3.3 Microstructural analysis

3.3.1 Scanning and transmission electron microscopy

The microstructures of all samples were examined using backscatter and secondary electron imaging with a field emission scanning electron microscope (FESEM) Zeiss Ultra Plus and Zeiss Sigma. Precipitation analysis including volume fraction, equivalent circle diameter, structure and chemical composition were analysed from as-received and heat treated samples by using energy dispersive spectrometers Oxford INCA X-act and EDAX Apollo-X together with INCA and EDAX microanalysis software. Final preparation of all samples for FESEM analysis was performed by oxide polishing using a colloidal silica suspension. The smallest spot size used in EDS measurements was $\sim 2 \mu\text{m}$. The detection limit for the EDS analysis is about 1000 ppm at its lowest [85]. In Paper III, FESEM was also utilized to study the morphology of particles extracted from the steel matrix. Electrolytic extraction of the precipitates was carried out in accordance with the ASTM E963 standard procedure [86]. The sample surfaces were ground with a diamond grinding disc and cleaned ultrasonically in acetone to remove adhering particles before the electrolytic extraction. The extraction was carried out using anodic dissolution in a platinum cathode electrolysis cell with a solution of 10% hydrochloric acid and 1% tartaric acid in methanol as an electrolyte. The samples were electrolyzed at a current density of $\sim 0.05 \text{ A/cm}^2$ until a weight loss of ~ 3.0 grams was achieved. The electrochemically extracted particles were collected by using vacuum filtration with a polycarbonate membrane filter (pore size of $0.05 \mu\text{m}$). The precipitates were then removed from the filter by ultrasonic agitation in 20 ml methanol and dried on a hot plate.

In Paper IV, a scanning transmission electron microscopy (STEM) detector on a high-resolution FE-SEM Hitachi SU70 with a TFEG source was used to analyse η - and σ -phase precipitates with a diameter of less than or equal to 50 nm, including the size distribution and volume fraction in the as-received samples and after heat treatment at 600 °C for 120 hours. Thin foils for STEM examination were prepared

by first mechanically grinding the samples down to a thickness of 70 μm , and then using a twin-jet electropolisher at a voltage of 32 V in an electrolyte containing 59 vol.% butanol, 35 vol.% methanol and 6 vol.% of perchloric acid at a temperature of -20 $^{\circ}\text{C}$. Particles with a diameter above 50 nm were analysed with FESEM. The true precipitate diameter X required to estimate the effect of precipitates on strengthening is measured when particles are analysed using thin foil samples. However, when the particles are analysed from bulk samples, i.e. with FESEM, the true precipitate diameter was converted from the average diameter x of the precipitates seen on the 2D section, as described in chapter 2.3.3.

To confirm the EDS results and to determine the crystallography of the η -phase, transmission electron microscopy examinations were performed in Papers II, III and V. The TEM used in Papers II and III was a LEO 912 Omega at 120 kV and, in Paper V, a JEOL JEM-2200FS at 200 kV. The samples for TEM were mechanically polished to a thickness of 70 μm . The thin foils were prepared with a twin-jet electropolisher (Tenu-Pol 5, Struers). In Paper II, the thin foils were prepared using voltage of 40 V and a current in the range of 100-120 mA in the electrolyte containing 10 vol.% of perchloric acid and 90 vol.% of acetic acid at room temperature. In Papers III and V, thin foils were prepared with a voltage of 32 V in an electrolyte containing 59 vol.% butanol, 35 vol.% methanol and 6 vol.% of perchloric acid at a temperature of -10 $^{\circ}\text{C}$.

3.3.2 X-Ray diffraction

An X-ray diffractometer was used to analyse the intermetallic precipitates and to calculate the dislocation density before and after heat treatments. In Paper III, the extracted precipitates were qualitatively analysed using a Siemens D5000 with Cu K_{α} radiation and a Bruker D8 Discover with a Göbel-mirror, Cu K_{α} radiation, and a LynxEye detector. In Paper IV, XRD measurements were made on Rigaku Smartlab using Co K_{α} radiation of 1.79 \AA wavelength. XRD line broadening analysis was carried out to determine dislocation densities in EN1.4521 before and after heat treatment at 600 $^{\circ}\text{C}$ for 120 hours. To avoid any changes in microstructure caused by the sample preparation, sample surfaces were lightly etched with colloidal silica.

The measured XRD patterns are shown in Fig. 16. The pattern is characterized by peaks, the width, height and the position of which can be used to determine crystallite size, lattice parameter and microstrain [87]. The fitting was carried out using a fundamental parameter (FP) method, which includes the instrument

function into the line broadening, and with the Rietveld refinement method, which uses a least squares approach to refine a theoretical profile until it matches with the measured profile [88].

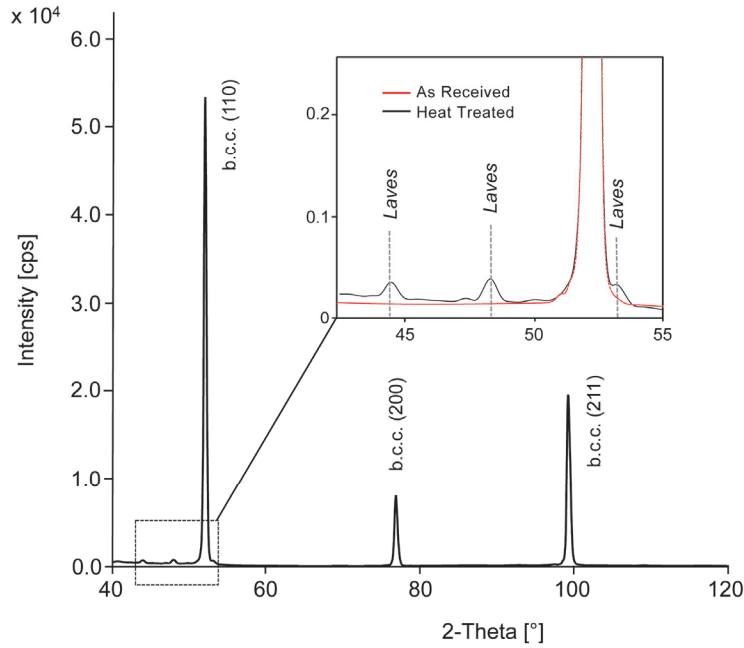


Fig. 16. XRD patterns of as-received and heat treated samples showing peaks for b.c.c. Fe. η -phase appears after heat treatment, as shown in the inset. MX type carbides and σ -phase are not seen in the patterns due to their low volume fractions (reprinted by permission from Paper III © 2014 Elsevier B.V.).

The dislocation density is calculated with crystallite size and microstrain using the Williamson and Smallman equation [87] given by:

$$\rho = \sqrt{(\rho_d \rho_s)} \quad (27)$$

and

$$\rho_s = \frac{k \varepsilon^2}{f b^2} \quad (28)$$

$$\rho_d = \frac{3n}{L_c^2}, \quad (29)$$

where ρ_d and ρ_s are the dislocation densities calculated from crystallite size L_c and from the microstrain ϵ respectively, k is a geometrical constant approximated as 14.4 for b.c.c. and n is a material dependent factor taken as 1 according to Williamson and Hall [87]. Table 2 shows the calculated dislocation densities for the as-received and heat treated samples (5.48×10^{13} and $7.11 \times 10^{13} \text{ m}^{-2}$ respectively) along with the lattice parameters.

Table 2. Lattice parameters and dislocation densities with standard deviations (obtained from XRD measurements) (reprinted by permission from Paper IV © 2018 Elsevier B.V.).

Specimen	Lattice parameter (Å) ($\pm 7 \times 10^{-6}$ to 1×10^{-5})	Microstrain $\times 10^6$ (± 6)	Crystallite size (Å) (± 7 to 9)	Dislocation density $\times 10^{-13}$ (m^{-2}) (± 0.015 to 0.027)
As-received	2.877	466	561	5.48
Heat treated	2.875	556	516	7.11

The smaller lattice parameter and higher microstrain in the heat treated sample is explained by the precipitation of η -phase [89]. The dislocation densities are consistent with those found in the literature [90]–[94], ranging from $1 \times 10^{13} \text{ m}^{-2}$ to $4 \times 10^{14} \text{ m}^{-2}$ for other ferritic steels. The amount of MX precipitates, η - and σ -phase in the as-received sample is too small for quantitative XRD analysis, but the amount of η -phase in the heat treated sample was high enough to be analysed. The analysis was done using the Rietveld WPPF and the Pseudo-Voigt method, which gave the amount of η -phase as 4.2 wt.%, which is close to both the measured and calculated values presented earlier.

3.4 Mechanical testing

3.4.1 Macro and micro-hardness

In Paper I, an instrumented micro-hardness tester by CSM Instruments was used to measure the micro-hardness with a load of 1 N at the centre of grains to avoid all precipitates. Micro-hardness was determined as an average value of ten indentations. The standard deviation in micro-hardness measurements was $\pm 3\%$. In Paper II, macro-hardness measurements were carried out using Struers Duramin A-300 hardness tester with a 98 N load. The standard deviation for macro-hardness tests was less than $\pm 3\%$.

3.4.2 Tensile tests

Engineering stress-engineering strain curves were measured according to the standard EN 10 002-1 using a computer-controlled Zwick Z250/SW5A tensile testing machine [95]. In Paper I, three tensile test samples were cut transverse to the rolling direction to determine the yield strength σ_y .

3.4.3 Sag tests

In Paper V, a sag test was carried out to evaluate the high-temperature creep resistance of the experimental and commercially available steels. Bars with dimensions of 150x15x2 mm³ were cut and placed into a furnace horizontally with both ends supported 20 mm above the bottom of the furnace, as shown in Fig. 17 and Fig. 18. The distance L, between the supports was 140 mm.



Fig. 17. Sag test environment and sample positioning.

The sample is kept in the furnace at temperatures in the range of 800 to 1050 °C. The deflection of the bar is measured after 20 and 100 hours. The creep deformation is caused solely by the sample's own weight and therefore depends on the bar dimensions. Hence, it is crucial that the dimensions, furnace and all other conditions are constant throughout the sag test for all samples. The active creep mechanism in the sag test can be estimated using the deformation map in which the different creep mechanisms are located in normalized stress–temperature space.

The creep mechanisms considered are power-law or dislocation creep, and the diffusional creep mechanisms, Coble creep and Nabarro-Herring creep [78], [79].

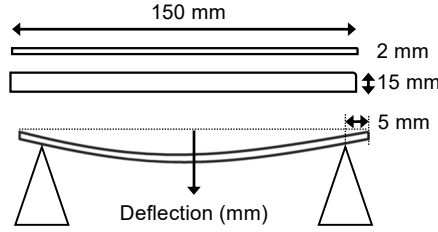


Fig. 18. Sag test sample dimensions (Under CC BY Paper V © 2019 Authors).

The stress state in the sag test is estimated with classical beam theory, where the sample is modelled as a simply supported beam. The problem is statically determinate and the distribution of the bending moment can be determined based on the equilibrium equations. In the beginning of the sag test, the cumulated inelastic strain is negligible and the distribution of axial normal stress is assumed linear over the thickness of the sample. The maximum shear stress is at the centre point between the supports, on the upper and lower surfaces, and is given by

$$\tau_{\max} = \left(\frac{3}{8}\right) \frac{dgL^2}{t}, \quad (30)$$

where d is the density of the material, g acceleration of gravity, L the distance between the supporting points and t is the thickness of the sample. The origin of the coordinate system is positioned in the middle plane of the sample on the leftmost supporting point. In the present geometry, the maximum shear stress has the value of $\tau_{\max} = 0.28$ MPa. The shear modulus has a dependency on temperature which can be considered linear according to Schneibel et al. [16] and Puchi-Cabrera et al. [17], and is described by:

$$\mu(T) = \mu_o - \frac{d\mu}{dT} \Delta T, \quad (31)$$

where $d\mu/dT$ is -37.3 (MPa/K) and the shear modulus at 300 K (μ_o) is 78 GPa [16], [17]. Therefore, the shear stress normalized with respect to the shear modulus is 7.0×10^{-6} at 1050 °C, and the homologous temperature, T/T_m , where T_m is the absolute melting temperature, is 0.7. Plotting these values to the deformation map for ferritic steel by Ashby [79], Zinkle and Lucas [77] imply that the dominant creep mechanism during the sag test is Coble Creep, typically occurring at low stresses and high temperatures. The creep rate in Coble creep is proportional to the

stress. Therefore, the linear distribution of axial normal stress prevails, provided that the curvature of the sample remains moderate. The maximum shear stress will be at near constant level and Coble creep will remain as the active deformation mechanism throughout the test in this case.

4 Results

4.1 Thermodynamic simulations

Thermodynamic and kinetic simulations with the Thermo-Calc software package including TC-Prisma were performed for two main reasons. The first was to provide comprehensive details of the microstructure including the following data regarding the phases: volume fractions, compositions, solvus temperatures and nucleation kinetics. This information was used to predict the results of various heat treatments and to validate microstructure analyses performed with FESEM, TEM and EDS. The second reason for thermodynamic and kinetic simulations was to decrease the time and resources required to design a new material, as was the case in Paper V.

4.1.1 Phase equilibria

Fig. 19 shows the equilibrium phase diagrams of EN1.4509 and EN1.4521 determined using the Thermo-Calc software with the database TCFE9. The simulation results show the precipitation of the η -phase and Ti- and Nb-containing MX type carbonitrides, where $M = Nb + Ti$ and $X = C + N$. According to the results, highly stable titanium carbonitrides and niobium carbides with traces of titanium can be present in the temperature regime from room temperature up to 1100 °C, while η -phase has a solvus temperature at 822 °C in EN1.4509 and 900 °C in EN1.4521. According to the phase equilibrium calculations, the composition of the η -phase at 650 °C in EN1.4509 is 51Fe-10Cr-6Si-33Nb and in EN1.4521 it is 58Fe-2Cr-6Si-26Nb-8Mo (at.%) which correspond to $(FeCrSi)_2(Nb)$ and $(FeCrSi)_2(MoNb)$ respectively. In Paper IV, the thermodynamic simulations for EN1.4521 were continued by calculating the isopleth equilibrium phase diagram as a function of carbon content shown in Fig. 20. The phase diagram shows that the phases present in the solid material at equilibrium above 600 °C are η -, χ - and σ -phase. In addition to the intermetallic phases, the microstructure is predicted to contain MX type precipitates, as shown in previous phase diagrams, at all calculated carbon levels from 0 to 0.1 wt.%.

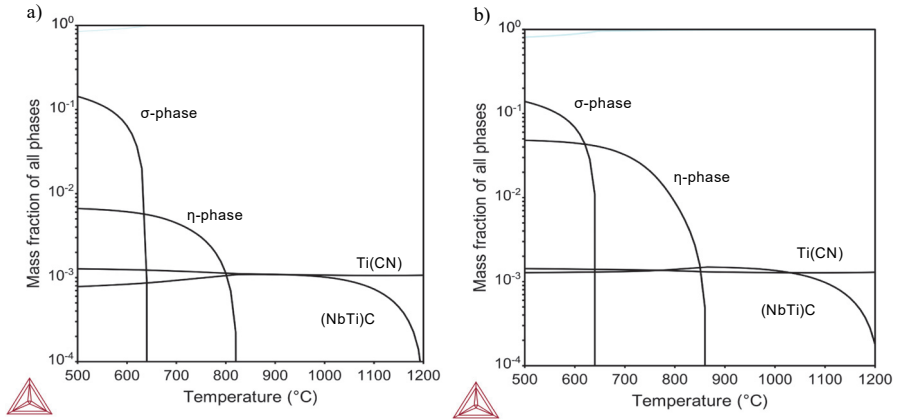


Fig. 19. Calculated equilibrium weight fractions of σ - and η -phase and Nb- and Ti-containing carbonitrides in a) EN1.4509 and b) EN1.4521 steels [Paper II].

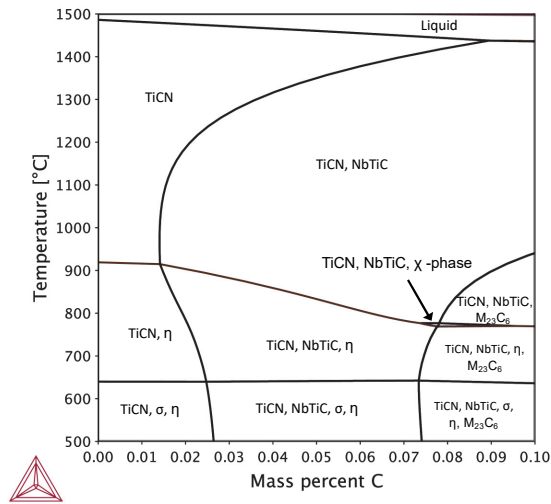


Fig. 20. Isopleth equilibrium phase diagram for EN1.4521 (reprinted by permission from Paper IV © 2018 Elsevier B.V.).

For clarity, the α -Fe have been omitted from the phase diagram. Each of the intermetallic phases have their own temperature range in which they precipitate. The η -phase has the largest temperature window and can precipitate below 920 °C, χ -phase in the range between 770 and 780 °C and σ -phase below 640 °C.

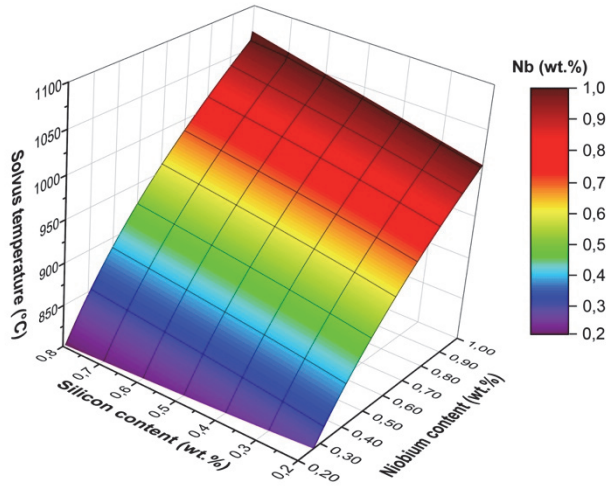


Fig. 21. Simulated solvus temperature of η -phase as a function of Si and Nb contents (wt.%) in 0.02C-0.02N-21Cr-0.32Mn base composition (Under CC BY Paper V © 2019 Authors).

In Paper V, Thermo-Calc was used to simulate the solvus temperature of η -phase as a function of Nb and Si contents for the base composition 0.02C-0.02N-21Cr-0.32Mn. The simulation results in Fig. 21 show that alloying with Nb raises the η -phase solvus temperature. A similar effect is achieved by alloying with Si, however to a smaller degree.

4.1.2 Kinetics and TTT curves for η -phase

To better understand the precipitation sequence of the equilibrium phases in EN1.4521, isothermal curves and time-to-precipitate diagrams were calculated using TC-Prisma. All calculations were performed based on the assumption that the alloy is single-phase α -Fe at time equal to zero and that nucleation occurs on the grain boundaries.

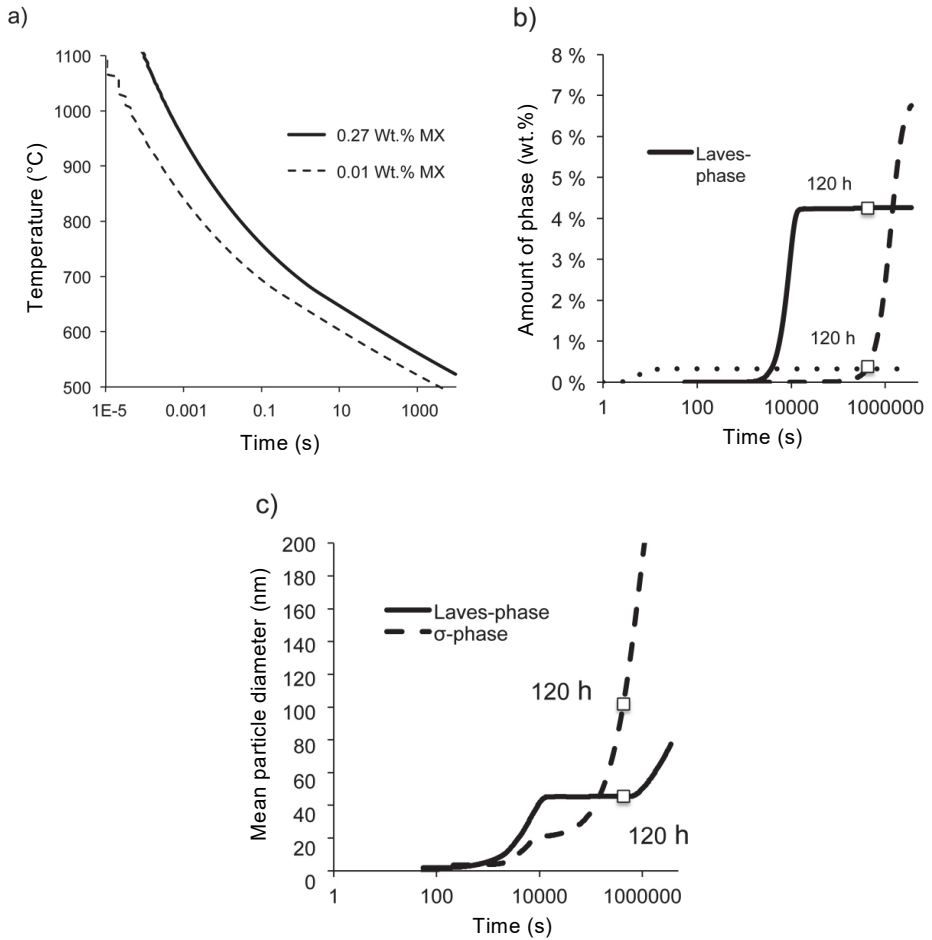


Fig. 22. Isothermal precipitation curves showing a) time to 0.01 wt.% and 0.27 wt.% precipitation of MX precipitates as a function of temperature, b) the amount of MX precipitates, η - and σ -phase in wt.% and c) the average diameter of η - and σ -phase particles for EN1.4521 after heat treatment at 600 °C (reprinted by permission from Paper IV © 2018 Elsevier B.V.).

The isothermal precipitation curves presented in Fig. 22 for EN1.4521, show that the MX type precipitates (NbTi)C and Ti(CN) should nucleate in a few seconds at the temperatures used in the present heat treatments and in a fraction of a second if the temperatures is above 1000 °C. The precipitation of MX type precipitates saturates after reaching a total of 0.27 wt.% (Fig. 22a). The intermetallic η -phase

has significantly slower kinetics, reaching a total of 4.3 wt.% after 4 hours at a temperature of 600 °C. However, η -phase precipitation is still predicted to be almost one hundred times faster than that of the σ -phase (Fig. 22b). σ -phase precipitation is predicted to saturate after reaching a total of 0.4 wt.%.

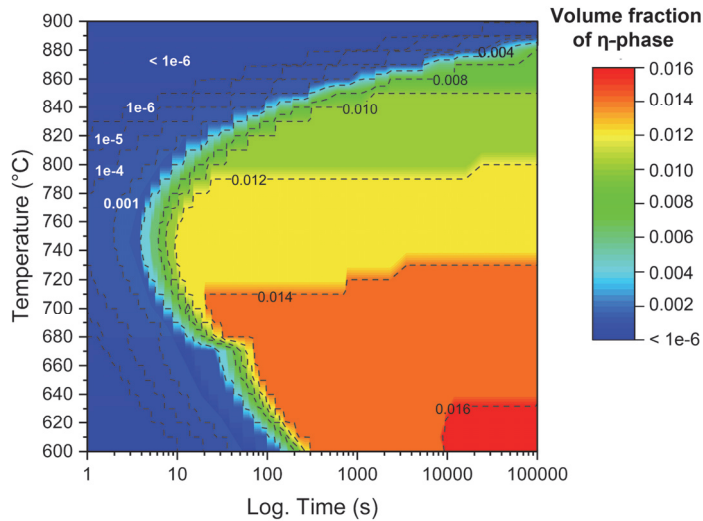


Fig. 23. Isothermal precipitation diagram of η -phase in High-Nb-SS (Under CC BY Paper V © 2019 Authors).

Another isothermal precipitation diagram (Fig. 23) was calculated for the High-Nb-SS steel designed, as described in Paper V. According to the diagram, 1% volume fraction of η -phase can precipitate in ~ 10 seconds in the temperature range of 700 to 800 °C. At higher or lower temperatures, the precipitation slows down significantly due to the reduction of the driving force (ΔG). The isothermal diagram can be used to estimate how much η -phase can precipitate in the microstructure during annealing, heat treatments or even cooling.

4.2 Microstructure analysis

In addition to the thermodynamic simulations presented in the previous chapter, an actual microstructure analysis of all of the samples was performed with various methods to validate the simulation results and to gain further knowledge on the

microstructure evolution of the samples at high temperature. The analysis results are summarized in Table 3.

Table 3. Precipitates present in the microstructures of EN1.4509 and EN1.4521 after heat treatments at various temperatures and heating times [Paper I, II, III].

Steel	Heating temperature	Time	Precipitates present	η -phase morphology
EN1.4509	450 °C	≤ 120 h	Ti(CN), (NbTi)C	n/a
EN1.4509	650 °C	≤ 120 h	Ti(CN), (NbTi)C, η -phase	plate-like
EN1.4509	800 °C	≤120 h	Ti(CN), (NbTi)C, η -phase	plate-like
EN1.4521	450 °C	≤120 h	Ti(CN), (NbTi)C, η -phase	plate-like & equiaxed
EN1.4521	600 °C	≤120 h	Ti(CN), (NbTi)C, σ - & η -phase	plate-like & equiaxed
EN1.4521	650 °C	≤120 h	Ti(CN), (NbTi)C, η -phase	plate-like
EN1.4521	800 °C	≤120 h	Ti(CN), (NbTi)C, η -phase	plate-like
EN1.4521	1050 °C	24 h	Ti(CN), (NbTi)C	n/a
EN1.4521	1050 °C + 650°C	24 h + 120 h	Ti(CN), (NbTi)C, η -phase	plate-like

4.2.1 Effects of heat treatments

In Paper I, the microstructure of EN1.4509 type stainless steel after heat treatments at various temperatures was analysed using FESEM EDS, as shown in Fig. 24. The analysis shows the presence of Nb- and Ti-containing carbonitrides as well as Si and Nb-containing η -phase, in line with the Thermo-Calc predictions given above. The η -phase has clearly precipitated mostly on the grain boundaries. The evolution of the precipitation during heat treatments at 450, 650 and 800 °C can be seen in Fig. 25. At the lowest temperature, no precipitation of η -phase occurs, which also correlates with the Thermo-Calc results. After some hours at 650 °C or 10 minutes at 800 °C, a significant amount of η -phase has precipitated. The average diameter and the Nb-content of precipitates formed at 650 °C are shown in Fig. 26 as a function of the duration of ageing. The size of the carbonitrides was measured with INCA image analysis. The size is based on the contrast difference between the particle and the surrounding matrix. The average diameter of (NbTi)C and Ti(CN) particles are ~0.6 to 0.8 μm and 1 μm respectively. It is apparent that neither the composition nor the size of these particles change during the heat treatments, even at the highest ageing temperature for up to 120 hours. It is suggested that the

coarsening of the carbonitrides is almost saturated in the course of the production process of the steels.

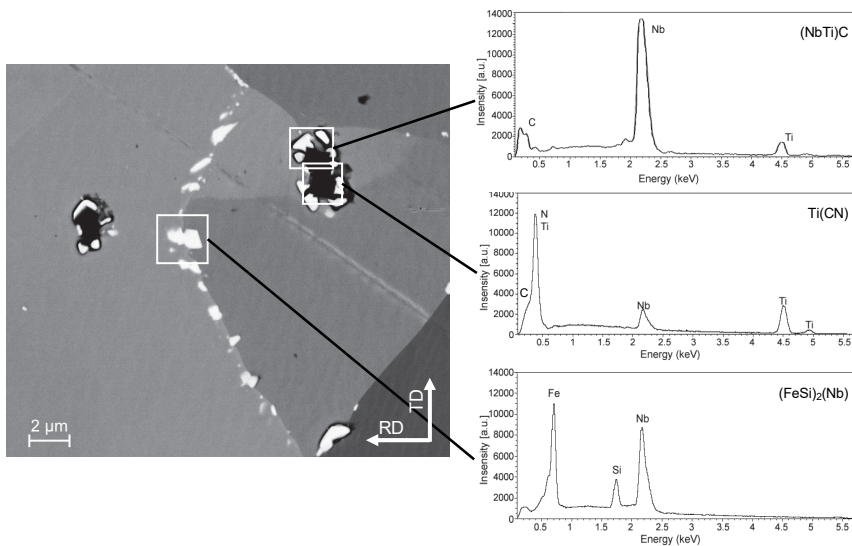


Fig. 24. FESEM backscatter image and EDS spectra of (NbTi)C, Ti(CN) and η -phase particles in EN1.4509 sample heat treated at 800 °C for 120 hours (reprinted by permission from Paper I © 2012 Trans Tech Publications Ltd.).

In Papers II and IV, precipitation in EN1.4521 steel was studied after heat treatments at 650 °C and higher. EN1.4521 has essentially the same composition as the previously examined EN1.4509, but with 2 wt.% Mo alloying. According to Thermo-Calc calculations and microstructure analysis for EN1.4509, a significant amount of η -phase and MX type carbonitrides can be expected to be seen after heat treatments at temperatures above 650 °C with reasonable heating times. FESEM micrographs before and after heat treatments at various temperatures and with various holding times are shown in Fig. 27. Unlike in EN1.4509, some amount of η -phase was present in the samples before the heat treatments.

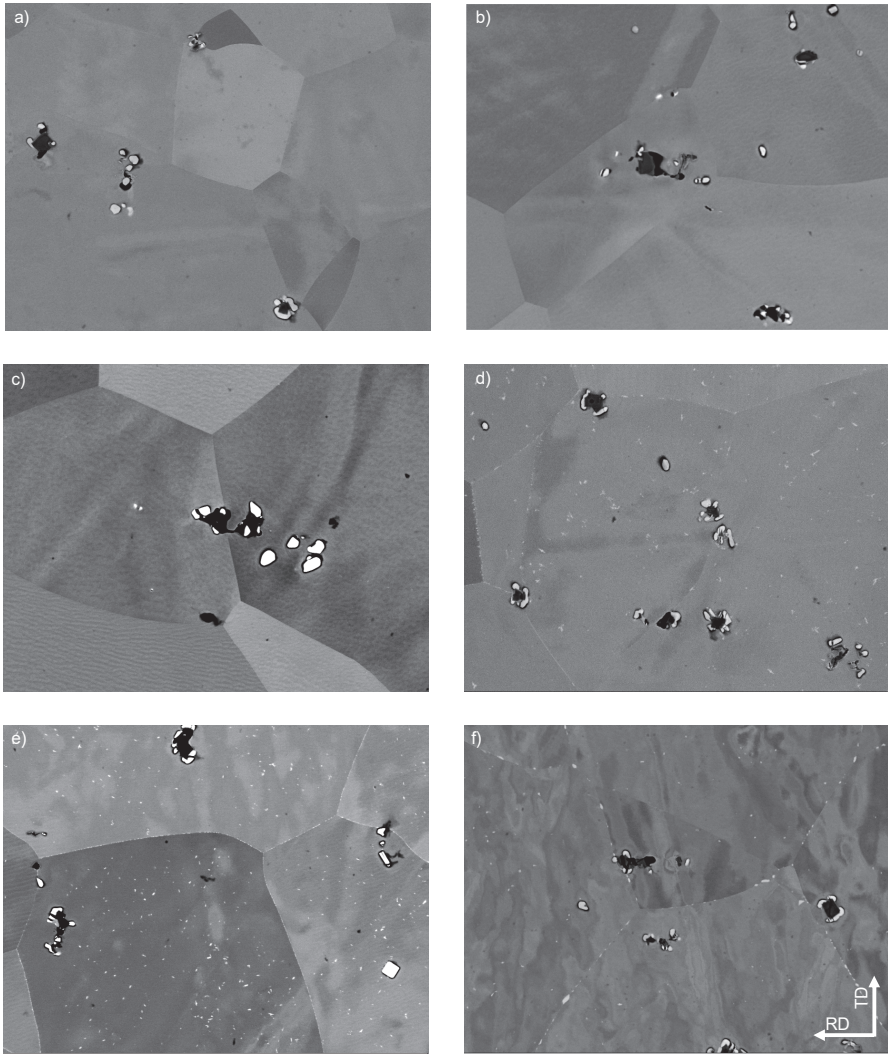


Fig. 25. FESEM backscatter images of EN1.4509 samples after different heat treatments with (NbTi)C and η -phase particles shown as light contrast and Ti(CN) as dark contrast: a) as received, b) 450 °C for 120 h, c) 650 °C for 2 h, d) 650 °C for 120 h, e) 800 °C for 30 min and f) 800 °C for 120 h (reprinted by permission from Paper I © 2012 Trans Tech Publications Ltd.).

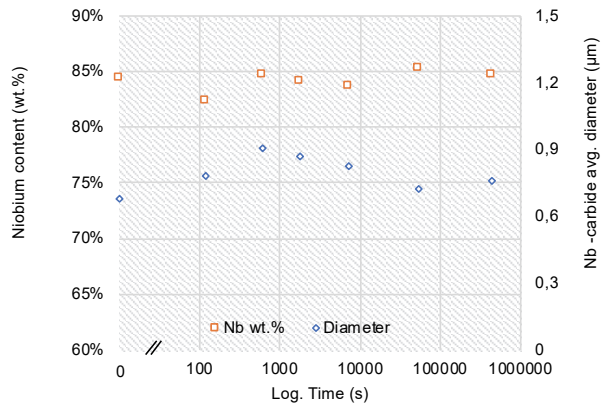


Fig. 26. EDS and INCA microanalysis results on the average diameter and Nb content of niobium carbides in the EN1.4509 steel samples aged at 450 °C until 120 h [Paper I].

In both steels, the Nb- and Ti-containing carbides are present in the as-received condition and the less common Ti(CN) is often surrounded by (NbTi)C, as shown in Fig. 24 and Fig. 25. As previously shown in the case of EN1.4509 steel, the influence of the heat treatments on microstructure evolution was also analysed.

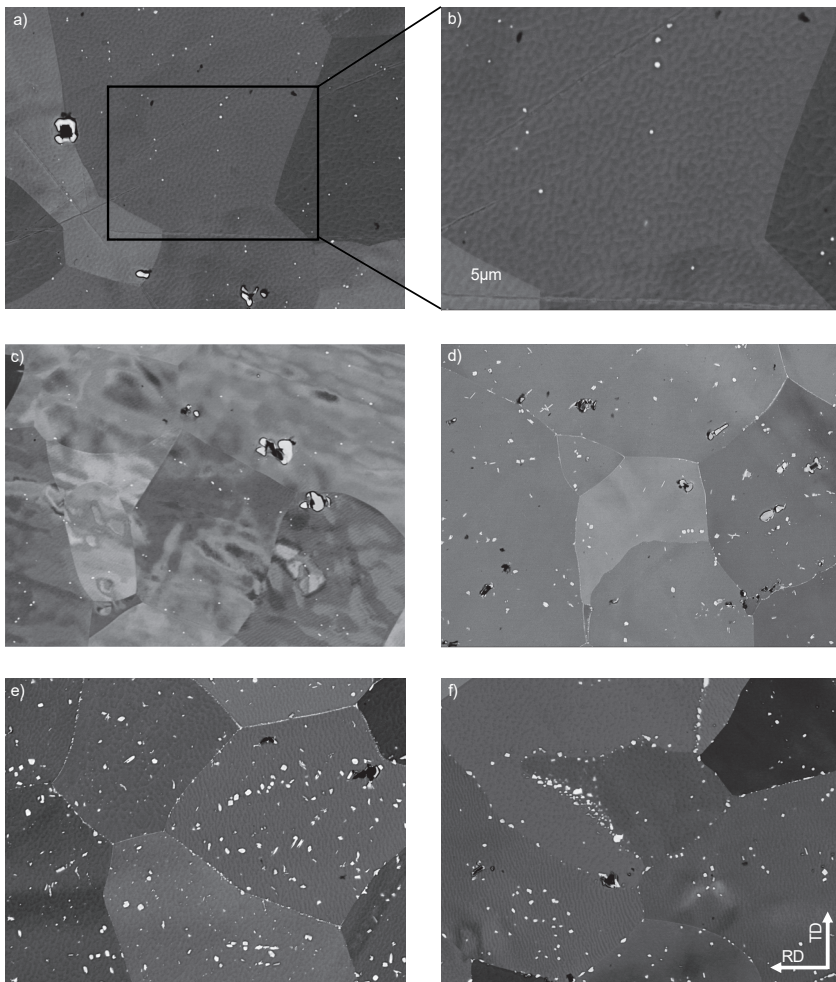


Fig. 27. FESEM micrographs of EN1.4521 with (NbTi)C and η -phase particles shown as light contrast and Ti(C,N) as dark contrast in a) and b) as received samples, and samples heat treated at c) 450 °C for 2 h, d) 650 °C for 15 h, e) 650 °C for 120 h and f) 800 °C for 120 h (reprinted by permission from Paper II © 2011 AIM and Paper III © 2014 Elsevier B.V.).

FESEM micrographs of heat treated samples are shown in Fig. 27. The volume fraction of η -phase increased after heat treatments at 650 °C with holding times

longer than 2 hours. The particles formed on both grain boundaries and grain interiors. However, when comparing the microstructure of samples aged at 650 °C and 800 °C for 120 hours (Fig. 27e and f), it can be seen that in the sample aged at 650 °C more precipitates are located within the grains.

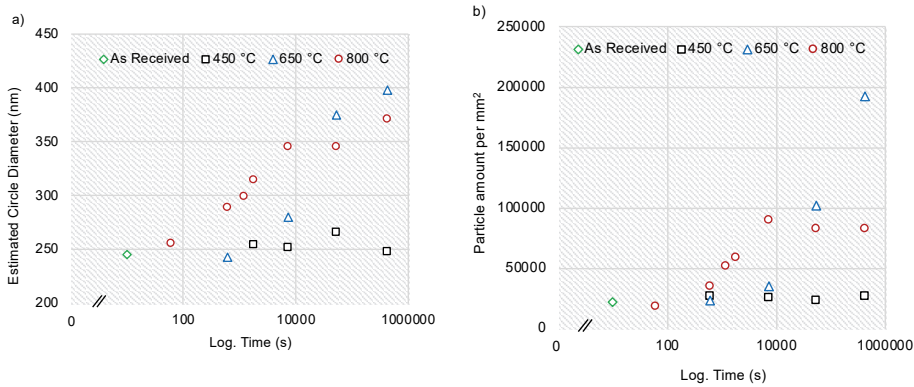


Fig. 28. INCA microanalysis results on a) the avg. ECD and b) number of η -phase particles per mm² in samples aged at 450 °C, 650 °C and 800 °C until 120 h [Paper II].

The size and number of η -phase particles was analysed using FESEM images from an area of $\sim 6000 \mu\text{m}^2$ in EN1.4521 samples heat treated at 650 °C and 800 °C for different periods of time. The average equivalent circle diameter (ECD) of the η -phase particles present before heat treatments was $0.25 \mu\text{m}$ with a particle number density of $0.02 \text{ } 1/\mu\text{m}^2$, as shown in Fig. 28. In samples aged for a minimum of 2 hours at 650 °C, the η -phase particle number density and size increased. After 120 hours the average ECD was $0.4 \mu\text{m}$ and the number density $0.18 \text{ } 1/\mu\text{m}^2$. In samples heat treated at 800 °C, fewer η -phase particles precipitated than in samples heat treated at 650 °C ($0.09 \text{ } 1/\mu\text{m}^2$) while the average ECD seemed to saturate at an almost equal diameter of $0.35\text{-}0.4 \mu\text{m}$. As mentioned earlier, in EN1.4521 some η -phase was present in the as-received condition. To understand and remove the effect of the previously nucleated η -phase, another preceding heat treatment at 1050 °C for 24 hours was performed to dissolve all η -phase. The difference in microstructure between the as-received condition and the sample heat treated at 1050 °C is shown in Fig. 29.

Again, the light particles are Nb- and Ti-containing carbides (NbTi)C, and the dark particles are Ti-containing carbonitrides Ti(CN). The smaller light particles

are η -phase. After the heat treatment at 1050 °C, all η -phase has dissolved, as seen in Fig. 29, with only carbonitrides and carbides present. Moreover, the grain size coarsened from an average grain diameter of 20 μm to 100 μm . The ECD of (NbTi)C also increased from 0.8 μm to 1.4 μm after the dissolution of η -phase. The average ECD of the (NbTi)C in non-annealed condition is the same as in EN1.4509 steel.

Fig. 29 shows the FESEM micrographs of a sample annealed at 1050 °C and subsequently at 650 °C for 120 hours. It can be seen that η -phase forms on the grain boundaries and grain interiors. During the heat treatment at 650 °C, the η -phase has nucleated and precipitated more homogeneously and densely within grains and on grain boundaries compared to the sample without a preceding heat treatment (Fig. 29). The different distributions of η -phase particles in the sample heat treated at 1050 °C and 650 °C compared to the sample only heat treated at 650 °C is presumably a result of the different microstructures prior to the heat treatment at 650 °C.

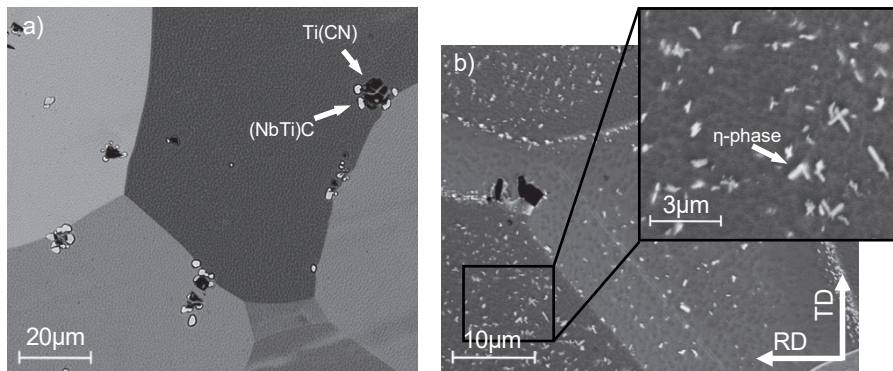


Fig. 29. FESEM micrograph of EN1.4521 samples heat treated at a) 1050 °C for 24 h and b) 1050 °C for 24 h and 650 °C for 120 h (reprinted by permission from Paper III © 2014 Elsevier B.V.).

A small number of η -phase particles are present in samples without preceding heat treatment and the particles further coarsen during the heat treatment at 650 °C, whereas in the heat treatment at 1050 °C η -phase dissolves. Sample without preceding heat treatment at 1050 °C would appear to include bigger η -phase particles and have less homogenous size distribution of η -phase particles compared to sample with preceding heat treatment. One logical explanation for this is that the

bigger particles have nucleated earlier in the process, and only some new particles nucleate during the heat treatment.

According to the Thermo-Calc results (Fig. 20) another intermetallic phase, i.e. σ -phase, can precipitate at temperatures below 644 °C in EN1.4521 steels. In Paper IV, the samples were heat treated at 600 °C where the material should be susceptible to the precipitation of σ -phase. The FESEM and STEM micrographs of the steel in the as-received condition and after heat treatment at 600 °C (such as the ones shown in Fig. 30) were used to estimate the diameter and amount of η - and σ -phase. The wt.% of small particles with a diameter less than 50 nm was measured on STEM images and the wt.% of larger particles on FESEM BSE images. The average diameter of the small precipitates in the as-received sample was estimated to be 17 nm and 29 nm in the heat treated sample. The total average diameters of all precipitates measured in the as-received and heat treated samples are 20 nm and 62 nm respectively.

Table 4. Diameters of η - and σ -phase precipitates and their weight fractions obtained from thin foil measurements and predicted using TC-Prisma (reprinted by permission from Paper IV © 2018 Elsevier B.V.).

Analysis	Classification	As-received	Heat treated (650 °C 120 hours)
Measured avg. diameter	(<50 nm)	17	29
	(>50 nm)	212	456
	(all)	20	62
Measured wt. %	(<50 nm)	0.44	1.45
	(>50 nm)	0.16	3.28
	(all)	0.60	4.73
Predicted wt. %	η -phase		4.3
	σ -phase		0.4

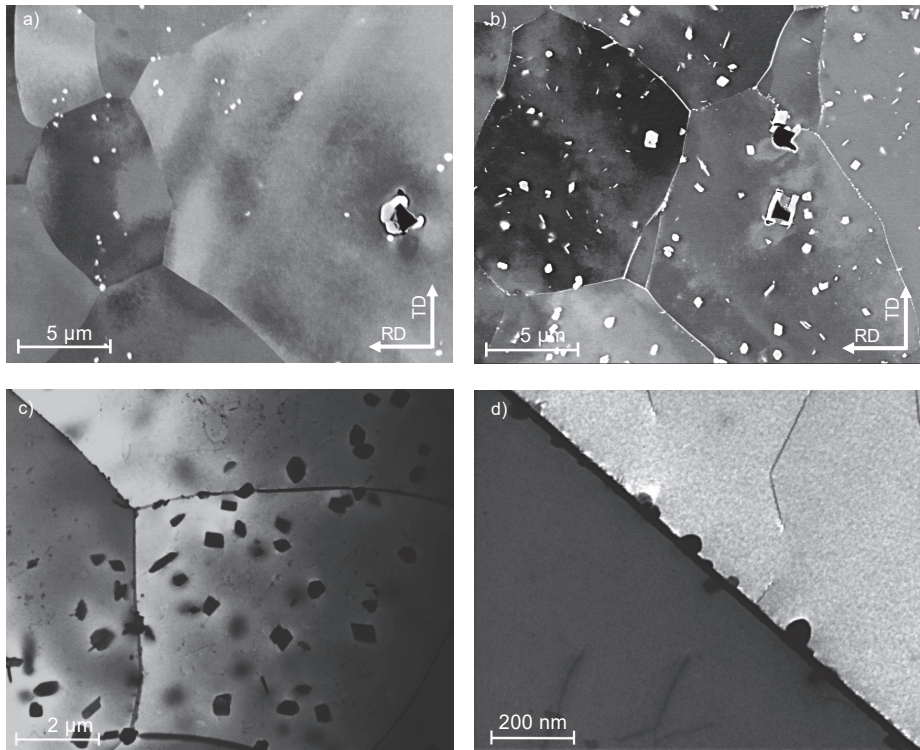


Fig. 30. FESEM backscatter images of EN1.4521 samples in a) as-received condition and b) heat treated at 600 °C for 120 h. c) and d) STEM micrographs of heat treated condition revealing a bimodal distribution of the η - and σ -phase precipitates homogeneously in the α -Fe matrix and at the grain boundary (reprinted by permission from Paper III © 2014 Elsevier B.V.).

The amount of the small η - and σ -phase particles in the as-received and heat treated samples was 0.44 wt.% and 1.45 wt.%, respectively. The total amount of all precipitates in the heat treated sample was 4.73 wt.%. This is in very good agreement to the amount of η - and σ -phase (4.3 and 0.4 wt.%) predicted with TC-Prisma shown in Fig. 22b. The measured particle diameters, volume fractions and the predicted mole fraction of intermetallic phases are shown in Table 4.

In Paper V, the knowledge regarding η -phase precipitation is used to design a new ferritic stainless steel for high temperature applications. The pre-annealing and final annealing of the trial steels were done using various annealing peak temperatures. The microstructures of the trial steels after annealing with different peak temperatures are shown in Fig. 31.

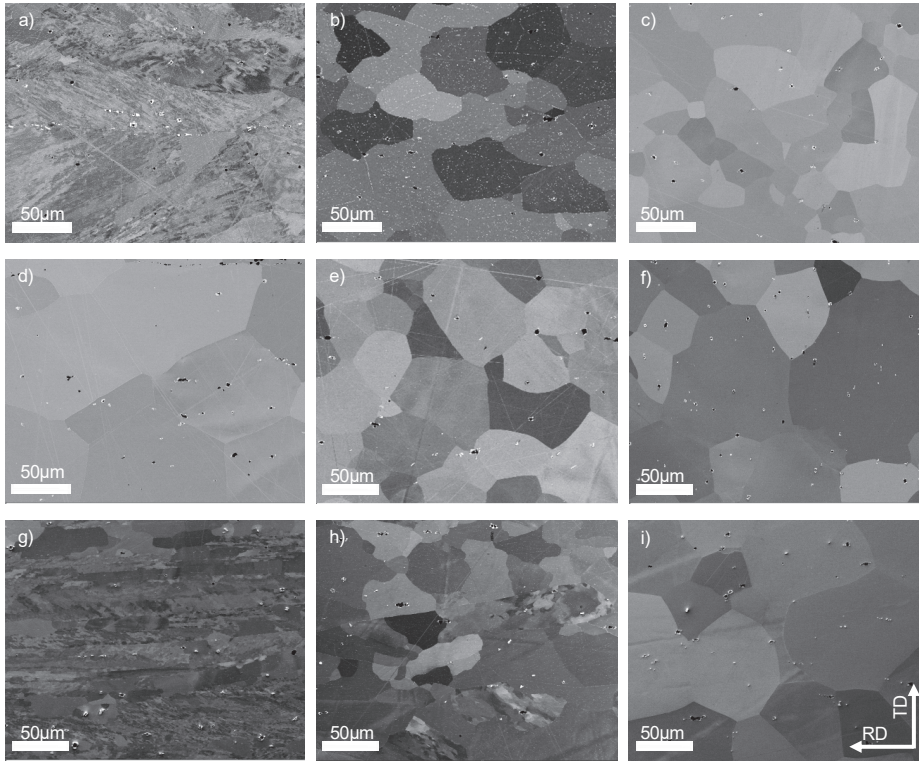


Fig. 31. FESEM backscatter images with (NbTi)C and η -phase particles shown as light contrast and Ti(CN) as dark contrast a) High-NbMo-SS annealed at 1000 °C, b) 1100 °C and c) 1120 °C, d) Mid-Nb-SS annealed at 950 °C, e) 1000 °C and f) 1120 °C, and g) High-Nb-SS annealed at 950 °C, h) 1050 °C and i) 1120 °C (Under CC BY Paper V © 2019 Authors).

The steel High-Nb-SS performed well in sag tests and therefore its microstructure was further studied after testing at 950 °C for 100 hours (see Fig. 32 for an example). The FESEM backscatter image clearly shows how most of the η -phase particles have nucleated on grain boundaries. A simple image analysis was carried out for the sample using ImageJ software, covering a total surface area of 1.64 mm² and including hundreds of particles. A volume fraction of 1.124% for all particles

visible in the backscattered electron images was measured, i.e. η -phase and NbC excluding TiN. The FESEM image shown in Fig. 32 is part of the analysed area.

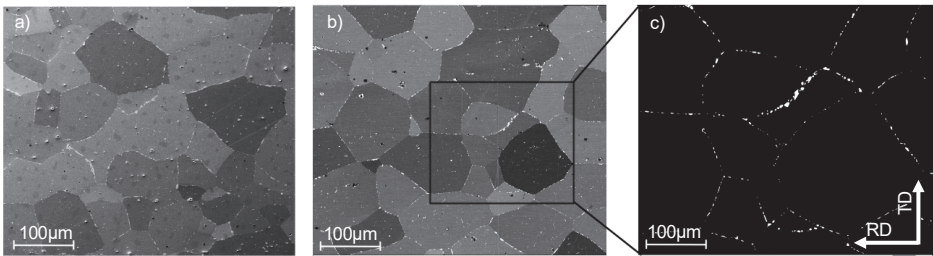


Fig. 32. FESEM micrographs of a) Mid-Nb-SS and b) High-Nb-SS after sag test with only particles on grain boundaries included in the on-set (Under CC BY Paper V © 2019 Authors).

4.2.2 Characterization of η -phase

Fig. 33 shows the chemical composition map created with EDS from a sample of EN1.4521 annealed at 1050 °C and subsequently at 650 °C for 120 hours with η -phase and Ti nitride particles. η -phase precipitates in both EN1.4509 (Fig. 24) and EN1.4521 steels. In the case of EN1.4521, Mo was found to precipitate as a component of η -phase in addition to Nb and Si, as seen in the EDS map.

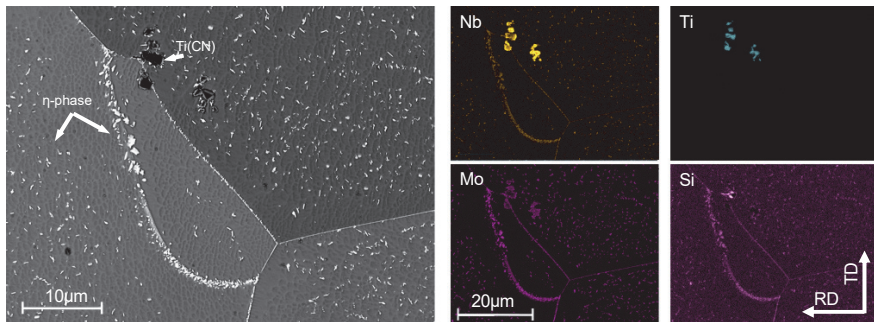


Fig. 33. EDS map of sample heat treated at 1050 °C and 650 °C showing Nb, Ti, Mo and Si in different colours (reprinted by permission from Paper II © 2011 AIM).

Extracted η -phase particles from samples with and without preceding heat treatments were further analysed using EDS and INCA analysis software to

eliminate the effect of the α -Fe matrix. The normalized results are summarized in the ternary diagram in Fig. 34 along with the equilibrium composition calculated using Thermo-Calc. The ternary diagram is plotted to show the contents of Fe on one axis, Mo and Nb on the second axis and Si on the third axis. The lattice structure of the η -phase is described as AB_2 where component A can be Fe, but also Cr, as shown by Kato et al. [96]. However, Cr was excluded from the results because of EDS analysis peaks from oxygen, deriving from the film used in sample preparation overlapping with those of Cr.

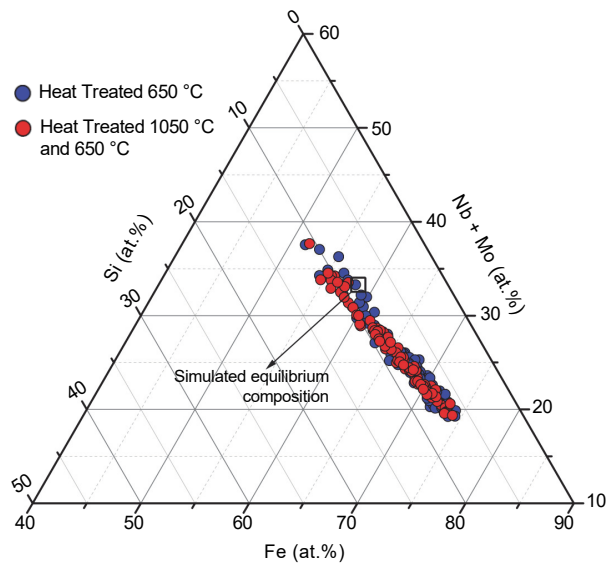


Fig. 34. The normalized η -phase composition in the particles extracted from samples with heat treatment at 650 °C (blue points) and 1050 °C & 650 °C (red points) plotted in a ternary diagram in which Nb and Mo are considered as one component (reprinted by permission from Paper III © 2014 Elsevier B.V.).

The amount of Si in the analysed η -phase particles in both samples is between 6 to 10 at.%. However, the amount of Fe and Nb+Mo changes significantly and varies between 55 and 75 at.% for Fe and 20 and 40% for Nb+Mo. It is possible that tiny flakes of the ferrite matrix are included in the extracted samples, which would artificially increase the apparent Fe content. Another possible explanation for the variation is morphology differences between the particles, i.e. the particle may face the EDS beam at a different angle. The equilibrium composition calculated with Thermo-Calc has 6 at.% Si. This is in good agreement with the EDS analysis,

although it is unlikely that the equilibrium state has been reached during the heat treatments. The dissolution heat treatment did not have any effect on the chemical composition of the phase.

In addition to differences in the spatial distribution of the η -phase, the shape of particles also seems different in samples with a preceding heat treatment, as seen in Fig. 29. Fig. 35 presents some higher resolution images of η -phase particles that were extracted from samples with and without a preceding heat treatment. The images reveal a clear difference in the morphologies of the η -phase particles after the different heat treatments. In a sample without preceding heat treatment, equiaxed particles and particles that have grown in two directions to form a plate-shaped particle are shown. Furthermore, the equiaxed type of particles, only seen in samples without preceding heat treatment, are bigger than the plate-like particles, shown in both sample conditions.

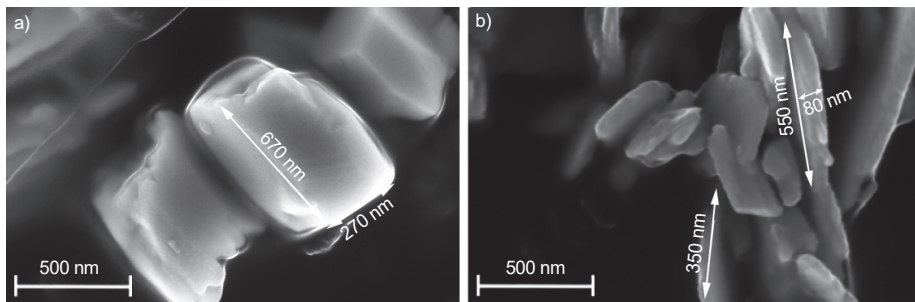


Fig. 35. FESEM secondary electron image of η -phase particles extracted from samples heat treated at a) 650 °C, b) 1050 °C and 650 °C (reprinted by permission from Paper III © 2014 Elsevier B.V.).

The extracted particles were further analysed using X-ray diffraction (see Fig. 36). Comparing the XRD peaks positions to the JCPDS database, the η -phase peaks corresponded to the phases Fe_2Mo (06-0622) and Fe_2Nb (17-0908).

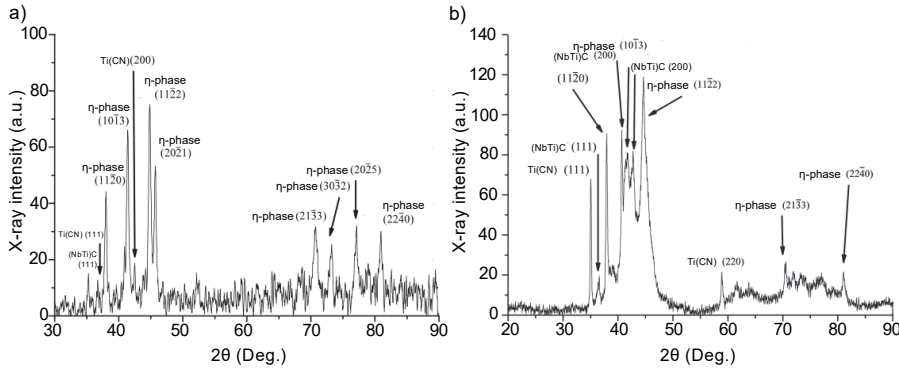


Fig. 36. XRD diffraction pattern of samples heat treated at a) 650 °C, b) 1050 °C and 650 °C (reprinted by permission from Paper III © 2014 Elsevier B.V.).

XRD was also used to measure the lattice parameters of particles in samples without preceding heat treatment. The a and c lattice parameters were 0.474 nm and 0.774 nm respectively, which are nearly identical to the lattice parameters of Fe_2Mo ($a = 0.473$ nm and $c = 0.774$ nm) [53]. The values were calculated considering the $hk0$ and $00l$ reflections of the hexagonal intermetallic phase [97], [98].

TEM was used to analyse the morphology and orientation relationship between the η -phase and α -Fe matrix. The TEM results confirmed that the η -phase in EN1.4521 has a hexagonal C14 crystal structure (Fig. 37). Furthermore, as explained previously, η -phase particles in EN1.4521 were seen to have two different, easily distinguishable morphologies. To find out whether this could be a result of the plate-like particle having a distinct orientation relationship with the α -Fe matrix, the orientation relationship was determined from the diffraction patterns presented in Fig. 37d as following $(\bar{1}101)_\eta // (21\bar{1})_\alpha$ and $[1\bar{1}02]_\eta // [011]_\alpha$.

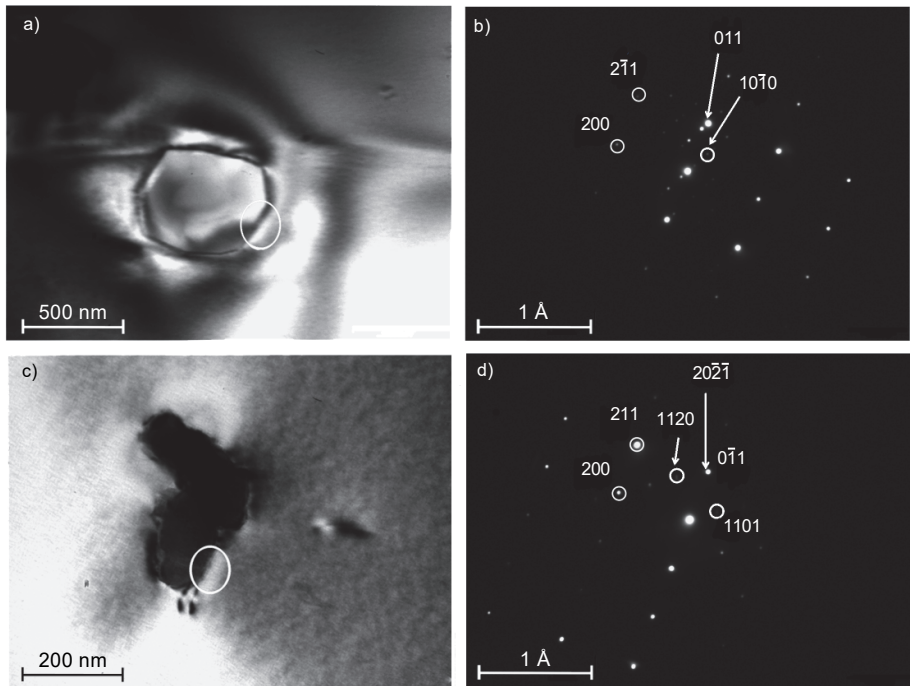


Fig. 37. η -phase particles of (a and b) equiaxed type with zone axis $[0001]_{\eta}$ and (c and d) plate-shaped type in the crystallographic orientation with α -Fe matrix ($[1\bar{1}02]_{\eta} // [011]_{\alpha}$) (reprinted by permission from Paper III © 2014 Elsevier B.V.).

4.3 Mechanical testing

In Paper I, tensile tests as well as macro- and micro-hardness tests were performed on EN1.4509 steel heat treated at 450, 650 and 800 °C up to 120 hours. Fig. 38 shows the room temperature yield stress σ_y of the steel after heat treatment at 800 °C for up to 16 hours. After heat treatment for 2 minutes, σ_y decreased significantly before reaching a constant level after heat treatments of 30 min or longer. The reduction of σ_y compared to the as-received sample is 90 MPa. The ultimate tensile stress and ultimate elongation was not affected by the heat treatments.

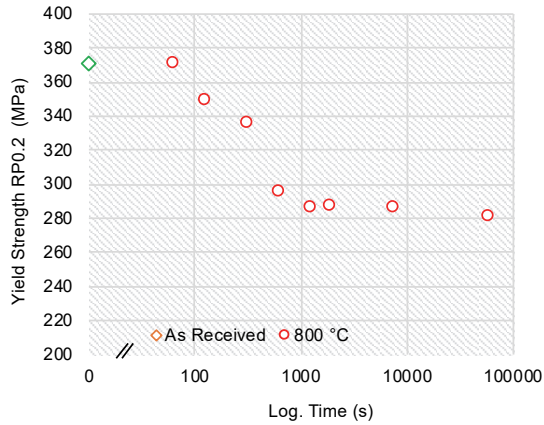


Fig. 38. Yield strength σ_y at room temperature after ageing at 800 °C for various times up to 16 h [Paper I].

Fig. 39 shows measured macro- and micro-hardness values at the centres of grains in samples heat treated at temperatures of 450 °C, 650 °C and 800 °C. The results are consistent with the previously presented tensile test results. Both macro- and micro-hardness values are highest for the as-received sample and decrease rapidly after a certain heat treatment time. In samples heat treated at 650 °C and 800 °C, the decrease in hardness appears in heat treatments of 10 minutes and longer. In samples heat treated at 450 °C, the decrease is smaller and seems to saturate in heat treatments of 2 hours and longer. Heat treatments at 450 °C did not seem to have any effect on the measured macro-hardness values (Fig. 39a).

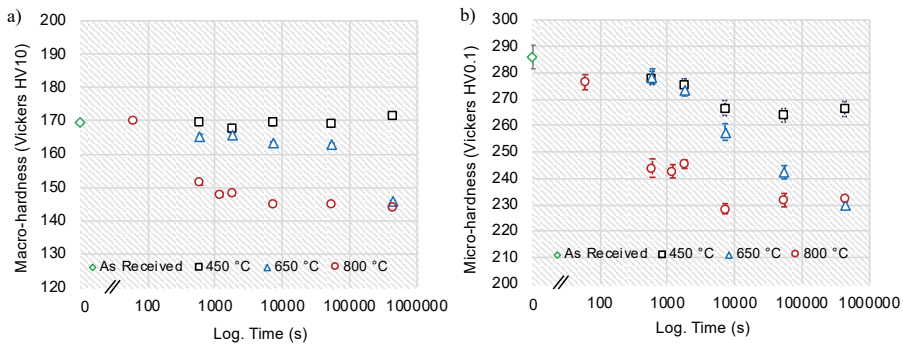


Fig. 39. a) Macro- and b) micro-hardness values for the EN1.4509 samples heat treated at 450 °C, 650 °C and 800 °C for various times up to 120 h [Paper I].

Heat treatments at temperatures above 450 °C result in similar drops in micro- and macro-hardness values. However, macro-hardness decreases less than micro-hardness.

In Paper II, macro-hardness measurements for EN1.4521 steel after heat treatments at 450, 650 and 800 °C were performed, and the results are shown in Fig. 40.

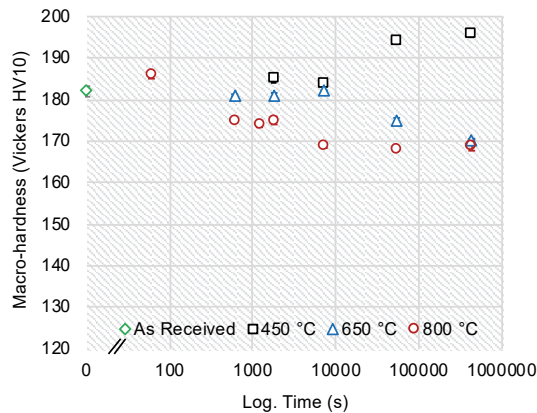


Fig. 40. Vickers HV10 hardness values for EN1.4521 samples heat treated at 450 °C, 650 °C and 800 °C for various times up to 120 h [Paper II].

The results show a decrease in hardness in samples heat treated at 650 °C for 2 hours or longer and in samples heat treated at 800 °C for 10 minutes or more. The results are consistent with the results for EN1.4509 steel in Fig. 39, however in EN1.4509 the hardness dropped ~15% while in EN1.4521, the hardness dropped ~8%. In samples heat treated at 450 °C for 2 hours or longer, the hardness seems to have increased (by 7% max.). The standard deviation in hardness results was less than 3%.

4.4 Sag tests

In Paper V, sag tests were carried out to evaluate the high-temperature creep resistance of the experimental and commercially available steels typically used in high temperature applications.

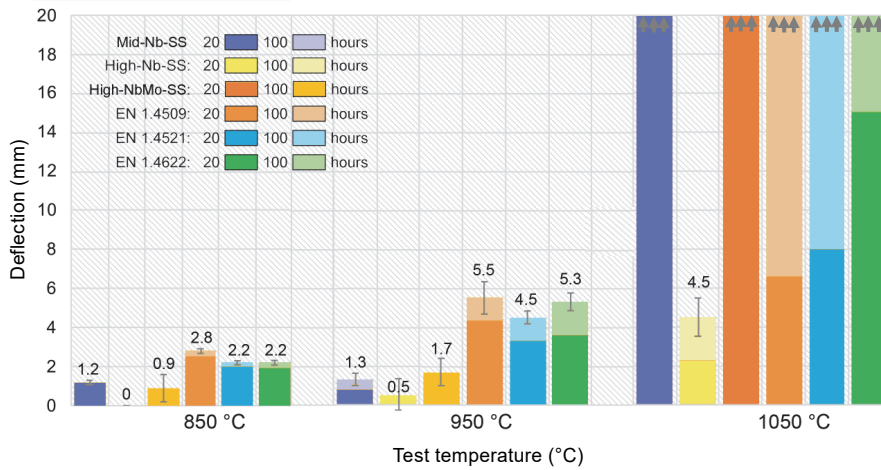


Fig. 41. Deflection measured after sag test at 850 °C, 950 °C and 1050 °C for the experimental and conventional ferritic stainless steels typically used in high-temperature applications (Under CC BY Paper V © 2019 Authors).

The results of the sag tests in Fig. 41 show that the deflection in the case of the experimental steel High-Nb-SS was significantly smaller than that in the commercial high-temperature ferritic stainless steels. This means that the High-Nb-SS steel possessed a clearly higher creep resistance under the stresses produced by the weight of the steel. At 850 °C there was no measurable deflection (i.e. <0.1 mm) for the High-Nb-SS steel during the 100 hour test and only 0.5 mm deflection was measured after testing at 950 °C. When tested at 1050 °C, the High-Nb-SS exhibited a deflection similar to that shown by the other steels at the lower temperatures of 850 °C and 950 °C.

5 Discussion

5.1 Precipitation of Nb- and Ti-containing carbonitrides

Typically, ferritic stainless MX type precipitates consist of Nb and/or Ti as the metal component M, and carbon and/or nitrogen as the component X. As shown by the thermodynamic simulations and microstructure analysis in chapter 4, these carbides, nitrides and carbonitrides are present in the microstructure of the studied steels in a temperature regime from room temperature to 1100 °C.

The microstructure analyses of all steel samples in this study showed the presence of MX precipitates in as-received microstructure as well as in microstructures after heat treatment. The MX precipitates were analysed to be Nb- and Ti-containing carbides (NbTi)C and titanium carbonitrides Ti(CN). The equivalent circle diameter (ECD) of the less common Ti(CN) was measured as 1000 nm while the (NbTi)C typically surrounding the Ti(CN) had an ECD of 800 nm. The ECD of (NbTi)C increased after heat treatments at 1050 °C, i.e. above the η -phase solvus temperature, to 1400 nm; however, the volume fraction of precipitates after heat treatments did not increase even after the longest holding time of 120 hours. The ECD of MX type precipitates was same in all the ferritic stainless steels studied in this work.

Further precipitation of MX precipitates beyond that found in the as-delivered condition was not observed as a result of any of the heat treatments. This is presumably due to the very fast kinetics of MX precipitation. According to the TC-Prisma calculations shown in Fig. 22, up to 0.27 wt.% of MX precipitates, including both (NbTi)C and Ti(CN), can nucleate and grow from a single-phase α -Fe in just few seconds at temperatures between 600 and 800 °C and in a fraction of a second at temperatures above 1000 °C. The equilibrium amounts of (NbTi)C and Ti(CN) calculated with Thermo-calc in EN1.4521 are 0.12 wt.% to 0.15 wt.% (Fig. 19) respectively, totalling to 0.27 wt.%. This implies that all MX carbonitrides will have been able to precipitate easily during prior steel processing, i.e. hot rolling, cold rolling, annealing and cooling, and are already present before the prolonged heat treatments of this study.

According to the microstructure analyses, MX precipitates are located within the grains. Typically, the nucleation first occurs on grain boundaries as suggested in the literature [49], [50], [59]. However, in this case the MX precipitation has already taken place during previous process stages, after which the microstructure

has recrystallized, resulting in a more homogenous distribution of the MX precipitates located within the new grains.

5.2 Precipitation of η - and σ -phase

In EN1.4509 type ferritic stainless steel, according to the thermodynamic calculations, η -phase will precipitate at temperatures from room temperature up to 800 °C. However, it was observed that at temperatures below 600 °C, heat treatment times required for precipitation of the η -phase could be extremely long, longer than the longest heating time of 120 hours used in this work. In Mo alloyed type EN1.4521 steel, the microstructure contained similar carbides and carbonitrides to EN1.4509, but unlike in EN1.4509, some η -phase was already present in the as-received material. The Mo addition in EN1.4521 seems to increase the precipitation rate and amount of η -phase compared to that of the η -phase in EN1.4509. The isopleth equilibrium phase diagram for EN1.4521 (Fig. 20) shows that η -phase, χ -phase and σ -phase can precipitate at temperatures above 600 °C. The η -phase is present in temperatures below 900 °C and the σ -phase below 640 °C. The precipitation of χ -phase would require higher carbon content than in any of the studied steels according to the calculated equilibrium diagram shown in Fig. 20, and therefore χ -phase does not precipitate in the studied steels. During the heat treatments at 600 °C, the steel is susceptible to the precipitation of η - and σ -phases.

According to the TC-Prisma calculations, η -phase is predicted to reach a total of 4.3 wt.% after 4 hours at 600 °C while only 0.4 wt.% of σ -phase is predicted to precipitate during the heat treatment. The TC-Prisma calculations suggest that the rate of precipitation decreases through the series $\text{MX} \rightarrow \eta\text{-phase} \rightarrow \sigma\text{-phase}$, which is in agreement with the experimental observations found in the literature [43], [49], [56], [58]. Typically, any nucleation of precipitates occurs first on the most preferable site, i.e. the grain boundaries. After grain boundaries the nucleation will continue on dislocations and finally homogeneously in the α -Fe matrix [43], [99]. According to the TC-Prisma calculations, the η -phase precipitation takes place only on grain boundaries during the heat treatment. However, as evidenced by the FESEM images, intermetallic precipitates were also found homogeneously through the grains, possibly after nucleating on dislocations, and likely in that order [49], [50], [59]. There are three possible reasons why η -phase did not precipitate only on grain boundaries as TC-Prisma results suggested: i) η - and σ -phase particles within grains might have nucleated during previous process stages before recrystallization, which is the case with MX precipitates, ii) the number of nucleation sites on grain

boundaries is overestimated in TC-Prisma calculations, or iii) the homogeneous nucleation barrier within the grains is overestimated in TC-Prisma, thereby excluding homogeneous nucleation from occurring. The reason can also be a combination of the above. However, the inaccuracy in TC-Prisma calculations regarding nucleation sites does not have significant relevancy to the results of this study, as the total amount of all η - and σ -phase precipitates in the heat treated sample, measured to be 4.73 wt.%, is in very good agreement to the amount predicted with TC-Prisma (4.3 wt.% η -phase + 0.4 wt.% σ -phase). The equilibrium volume fraction of η -phase decreases towards the solvus temperature (as seen in Fig. 19), which is suggested to be the reason for the lower saturation level in the case of samples aged at 800 °C compared to samples aged at 650 °C. To dissolve all η -phase, samples were heat treated at 1050 °C before the following heat treatment at 650 °C. In this case, the nucleation and precipitation occurred more homogeneously and densely both on grain boundaries and within the grains, but not entirely, as the TC-Prisma calculations suggested, on grain boundaries. Therefore, as previously suggested, it seems that the simulations overestimate either the density of nucleation sites on grain boundaries or the nucleation barrier for homogeneous nucleation. However, even with infinite number of nucleation sites, the diffusion from the centre of the grain would be very slow, therefore making the latter option more likely.

5.3 Characterization of η -phase

5.3.1 Composition of η -phase

According to the Thermo-Calc simulations and EDS analyses, η -phase in EN1.4509 type steel consists of Fe, Cr, Nb and Si. It has been shown that Si does not form carbides in the presence of Fe and is therefore susceptible to η -phase precipitation [34]. In EN1.4521, which has a similar composition as EN1.4509 but with an addition of molybdenum, the η -phase composition also included Mo. According to the Thermo-Calc results, the equilibrium composition of the η -phase at 650 °C in EN1.4509 is 51Fe-10Cr-6Si-33Nb and in EN1.4521 58Fe-2Cr-6Si-26Nb-8Mo (at.%). These correspond to the formulae $(\text{FeCrSi})_2(\text{Nb})$ and $(\text{FeCrSi})_2(\text{MoNb})$ respectively. The EDS analyses done on extracted particles of EN1.4521 showed that the amount of Si in the η -phase is fairly constant at 6–10 at.%. The compositions calculated with Thermo-Calc are consistent with the

measured ones, although the microstructure is unlikely to have reached the equilibrium state during the heat treatments. These results are also in agreement with the results of Kato et al. [96], who measured the amount of Si to be 9.2 at.% in $(\text{FeCrSi})_2\text{Nb}$ phase. The reason for Si stabilization in the η -phase has been suggested to be due to the effective electron concentration [100]. Furthermore, Iseda et al. [101] reported that Si substitutes for Fe in the $(\text{FeCrSi})_2(\text{Mo})$ η -phase, and Kato et al. [96] reported similar results for the $(\text{FeCrSi})_2\text{Nb}$ η -phase. However, in the study by Padilha et al. for austenitic stainless steels, Si was considered as an A component in the AB_2 η -phase, so that the chemical formula should be written $(\text{FeCrNi})_2(\text{NbSi})$ [102]. Considering the existing research by previously mentioned authors, the Thermo-Calc simulations and EDS analysis, it is suggested that in the case of η -phase with Mo and Nb, the Si acts as part of the B component and corresponds to $(\text{FeCrSi})_2(\text{MoNb})$. In the EDS analyses, the Cr peaks overlap with oxygen deriving from the film on which the particles were placed, and therefore Cr was ignored in the analysis. Boutarek et al. [103] showed that large amounts of Cr can dissolve in the Fe_2Nb η -phase in the Fe–Cr–Nb system. However, in ferritic stainless steels the amount of Cr in η -phase varies between 2 and 10 at.% according to Thermo-Calc calculations, while Kato et al. [96] experimentally found the content to be between 0 and 3 at.%. The amount of Cr in η -phase can be considered small and, therefore, the lack of experimental data on the amount of Cr is ignored when analysing the composition of η -phase. The dissolution heat treatment did not seem to have a significant effect on the chemical composition of the η -phase.

The X-ray diffraction pattern of extracted residues was compared to the JCPDS database and the η -phase peaks were found to relate to the reflections of the phases Fe_2Mo (06-0622) and Fe_2Nb (17-0908) [104]. The XRD results are consistent with Thermo-Calc calculations and EDS analyses, and similar peaks were also found by Tavares et al. [105]. Therefore, $(\text{FeCrSi})_2(\text{MoNb})$ as the major η -phase can be confirmed even though the JCPDS database did not include η -phase with Si.

5.3.2 Crystal structure and morphology of η -phase

The crystal structure of the η -phase was verified with TEM and XRD as being hexagonal, in agreement with similar observations in the literature [53], [54]. The lattice parameters of η -phase ($a = 0.474$ nm and $c = 0.774$ nm) are in agreement with those reported in literature for Fe_2Mo ($a = 0.473$ nm and $c = 0.774$ nm) [53]. Therefore, the Nb and Si addition can be seen to have almost no effect on the lattice

parameters. This can explain why the XRD peaks of the η -phase correlated with the ones in the JCPDS database for η -phase without Si.

The size difference observed earlier between the η -phase particles in samples with and without preceding dissolution heat treatment at 1050 °C could be explained by the fact that the bigger particles have nucleated earlier in the process. The process stage in which the nucleation occurs can result in different coherence of the interface between the particle and α -Fe, as stated in the literature [11]. The different coherence can result in differences in the morphology once the particle grows, i.e. the morphology of the η -phase particles in the samples with preceding dissolution heat treatment (plate-like) has a distinct orientation relationship with the α -Fe matrix, whereas the particles which presumably formed earlier in the process (equiaxed) have no orientation relationship. Recrystallization and grain growth will have left the equiaxed particles within the α -Fe grains in which they lack an orientation relationship. The orientation relationship between the plate-like η -phase particles and the α -Fe was determined as $(\bar{1}101)_{\eta} // (21\bar{1})_{\alpha}$ and $[1\bar{1}02]_{\eta} // [011]_{\alpha}$. The same orientation relationship was observed by Cocks et al. for η -phase in the Fe–Nb system. Cocks determined the habit plane of the plate-like precipitates to be $\{111\}_{\alpha}$ [60].

5.4 Effect of η -phase on mechanical properties of the steel

The following chapter addresses the effect of η -phase precipitation on the hardness and yield strength of EN1.4509 and EN1.4521 type ferritic stainless steels at ambient and high temperature.

Micro- and macro hardness

In EN1.4509 steel, micro-hardness decreased significantly within the same ageing times and temperatures where the precipitation of η -phase becomes evident. Using lower heat treatment temperature of 450 °C where the η -phase does not precipitate, the decrease was smaller and ceased after 2 hours of ageing. Macro-hardness did not change at all in heat treatments at 450 °C, which implies that the change in micro-hardness at low temperatures was not due to the η -phase but a result of some internal stresses relieving in the structure. After heat treatment at higher temperatures, the decrease in micro- and macro-hardness was more significant. Micro-hardness was found to decrease more than macro-hardness, which may be caused by the loss of solid solution strengthening elements such as Nb and Si to η -

phase. Furthermore, the growth of η -phase particles could decrease the effect of precipitation strengthening. Some contribution to the difference between the two hardness values may also derive from factors such as grain boundaries, which should be considered when comparing the micro- and macro-hardness measurements.

In a similar way to EN1.4509, the hardness data for EN1.4521 is also consistent with the precipitation of η -phase. The hardness decreased in samples after heat treatments in 650 °C suggesting that the nucleation and coarsening of the η -phase contributes to the drop in hardness. However, in EN1.4509 the precipitation reduced the hardness more significantly (~15%) than in EN1.4521 (~8%). The smaller decrement in strength must be due to the differences in η -phase composition, i.e. Mo, and its effect on solid solution strengthening. Another difference between the two steels was that in EN1.4521 heat treatment at 450 °C for 2 hours increased the hardness slightly. This could be caused by tiny particles, and Ashby-Orowan type dispersion strengthening, that, however, were not made visible with the techniques used in Paper II [28].

In Paper IV, the effect of η -phase precipitation on ambient or high-temperature strength was studied by carrying out a complete breakdown of strengthening mechanisms with each mechanism considered individually. The tensile test results for EN1.4521 at both ambient temperature and 600 °C were reported by Östman et al. [106], reproduced in Table 5.

Table 5. Yield strength of EN1.4521 measured by Östman et al. at ambient temperature and 600 °C in the as-received and heat treated conditions (reprinted by permission from Paper IV © 2018 Elsevier B.V.).

Testing temperature	Sample condition	
	As-received	Heat treated at 600 °C for 120 hours
Ambient	406 MPa	425 MPa
600 °C	198 MPa	183 MPa

The samples were held for 30 minutes at the target tensile test temperature of 600 °C before testing. The holding time or the test itself had no effect on the precipitate microstructure, i.e. no further coarsening or nucleation of precipitates in addition to what had occurred during the production of the material or the preceding high-temperature heat treatment. A more detailed analysis is presented in Paper IV. The possibility of dynamic strain ageing (DSA) was also examined by Östman et

al., but the tensile test results showed no significant serrated, unstable behaviour usually related to DSA [107].

5.4.1 Room temperature yield strength

In Paper IV, the yield strength of the steel is considered as a sum of each contributing strengthening mechanism. To understand the effect of the precipitation on the yield strength, each mechanism is considered individually. The strengthening mechanisms are friction stress, Hall-Petch, strengthening due to dislocations, precipitation strengthening and solid solution strengthening. The room temperature yield strength is calculated for EN1.4521 and compared to the results shown in Table 5 for as-received samples and samples heat treated at 600 °C.

The friction stress of 111 MPa for α -Fe in room temperature was calculated using shear modulus (78 GPa), Poisson's ratio (0.33) and Burgers vector ($\frac{a}{2}\sqrt{3} = 0.249$ nm), where the lattice parameters $a = 0.288$ nm was measured with XRD. Friction stress is typically approximated as 100 MPa for pure α -Fe in the literature [108]–[110]. Friction stress and grain boundary strengthening are unaffected by the heat treatments. Strength owing to the Hall-Petch term was calculated using a grain size of 23 μ m, measured using the mean linear intercept method. The grain size was the same in all samples and was not affected by the heat treatments.

According to the Thermo-Calc equilibrium calculations, room temperature and heat treatments with all N will have precipitated in MX type carbonitrides in both the as-received and heat treated material while 0.05 ppm of C remains in solution in b.c.c. phase.

The Hall-Petch strengthening contribution is 31 MPa at room temperature. The strengthening due to dislocations was calculated using the Taylor equation with a Taylor factor of 2.9 and $\alpha = 0.5$, which are typically used for ferritic stainless steels [74], [92], [111], [112]. The calculated strengthening contributions by dislocations were 72 MPa and 82 MPa for the as-received and heat treated samples respectively.

Precipitation strengthening caused by η - and σ -phases was calculated using the Ashby-Orowan equation. With the amount and size of the particles considered, the yield strength owing to precipitation is 150 MPa for the as-received condition and 196 MPa for the heat treated (at 600 °C for 120 hours) condition. Therefore, the increase of room temperature yield strength due to the precipitation during heat treatment is 46 MPa. The experimentally measured yield strength was 19 MPa higher after heat treatment, which is 27 MPa less than the estimated increase. This

is explained by the loss of solid solution strengthening as a result of the precipitation of η - and σ -phases. The decrease can be estimated by calculating the effect of solid solution by the alloys precipitating. However, the only solid solution strengthening coefficient in the literature for Nb in α -Fe is 4230 MPa/wt.% [20], which is likely to be a gross overestimation, as noted by Kostyrychev et al. [21]. To overcome this shortcoming, a regression analysis was made to formulate an equation for solid solution strengthening in α -Fe based on two key parameters known to influence the strengthening coefficient of an alloying element, i.e. the shear modulus and the atomic radius [18], [28], [67], [68], [113]. The analysis gave Nb a strengthening coefficient of 16 MPa/at.%. A more detailed description of how the coefficient was determined is shown in Paper IV. Most of the Nb has, however, precipitated, and, as expected, the effect of Nb in solution is very small. Considering all alloying elements, the solid solution strengthening effect decreases by 20 MPa as a result of the heat treatment and precipitation. This explains the 19 MPa difference mentioned above. The loss of solid solution strengthening arising from the heat treatment is due to the precipitation of Mo, Nb and Si in η -phase and is in good agreement with the results regarding the combined effect of precipitation and solid solution strengthening.

In Paper I, the yield strength was measured after heat treatments of EN1.4509 samples at 800 °C for various holding times. In this case, the yield strength seemed to drop after the precipitation of η -phase. The η -phase particles were present mostly on grain boundaries (Fig. 27), and have had more time to coarsen, which will mitigate the contribution to yield strength from the dispersion strengthening effect. In this case, the precipitation of η -phase would have a negative effect on the yield strength of the steel.

5.4.2 High temperature yield strength

Yield strength measured at 600 °C was over 200 MPa lower than at room temperature [106]. Furthermore, contrary to room temperature behaviour, the yield strength was higher in the as-received material than in the heat treated sample. The drop in yield strength is explained by the different behaviour of the various strengthening mechanisms at higher temperature, e.g. as a result of the decrease of shear modulus as a function of temperature, which affects the magnitude of many of the strengthening mechanisms.

The effect of friction stress is related to the short-range stress field of the dislocation core, which makes the friction stress sensitive to temperature because

of the effect of temperature on the thermal energy of the atoms. This results in relatively large friction stress at low temperatures. However, especially in b.c.c. lattices with narrow dislocation widths, the stress decreases rapidly as the temperature increases. Friction stress is considered to reach zero well below 600 °C as experimentally observed by Schneibel et al. [64], [110], [114]–[116].

Strengthening owing to grain boundaries, precipitation and dislocations is susceptible to the temperature dependency of Burgers vector and the shear modulus as mentioned earlier. The change in Burgers vector as a function of temperature has been determined by Van Bohemen et al. [19], who studied the thermal expansion in b.c.c. iron and steels. According to these studies, the lattice parameters change by less than 1% between ambient temperature and 600 °C. Therefore, the change in Burgers vector during high temperature tensile tests is ignored. XRD results in Table 2 showed that the heat treatment changed the lattice parameters only by 0.1% so Burgers vector is also considered unchanged as a result of heat treatment. Ignoring the change in Burgers vector means that the significant drop in yield strength at higher temperatures is due to the decreased shear modulus. The temperature dependency of shear modulus was described in Eq. 31 in chapter 3.4.3. According to the relation, the shear modulus at 600 °C is reduced to 56 GPa. The temperature is expected to have a minor effect on Hall-Petch strengthening due to very low interstitial amount, and therefore no significant grain boundary segregation of carbon or nitrogen occurs [109]. However, the Hall-Petch coefficient k' is dependent on the shear elastic modulus related to μ/μ_0 , which results in a decrease of 9 MPa, from 31 to 22 MPa [65], [66]. The decrease of shear modulus also contributes to the yield strength contribution of dislocations.

As previously explained, the tensile test itself caused no coarsening or precipitation of the intermetallic phases, and, therefore, the same precipitation parameters apply when calculating the strengthening due to precipitates at 600 °C as for the room temperature, apart from the lower shear modulus. The decreased shear modulus results in 41 and 54 MPa lower contributions to yield strength in as-received and heat treated samples respectively.

The only strengthening mechanism with decreased contribution to yield strength as a result of the heat treatments and precipitation is the solid solution strengthening. Therefore, it is suggested to be the cause of why the yield strength in the as-received sample is higher compared to heat treated sample in the high-temperature tests. There is a significantly higher concentration of elements in solid solution strengthening the material in the as-received sample; however, the magnitude of solid solution strengthening also decreases as the temperature

increases. On the basis of the relation determined by Lu et al. [18], solid solution strengthening is reduced by a factor of 0.203 at 600 °C compared to room temperature.

Table 6. Comparison of calculated and measured yield strengths (reprinted by permission from Paper IV © 2018 Elsevier B.V.).

Specimen condition	Testing T (°C)	σ_i (MPa)	$\frac{K_y}{\sqrt{d}}$ (MPa)	σ_{ss} (MPa)	σ_{ppt} (MPa)	σ_d (MPa)	Calculated σ_y (MPa)	Measure	Ratio calc./meas.
								d (MPa)	
As-received	Ambient	111	31	61	150	72	425	406	1.05
Heat treated	Ambient	111	31	41	196	82	461	425	1.08
As-received	600 °C	0	22	12	109	52	195	198	0.99
Heat treated	600 °C	0	22	9	142	59	232	183	1.27

The contribution of the different strengthening mechanisms to the yield strength for as-received and heat treated samples tested at room temperature and at 600 °C are summarized in Table 6. The calculated values are very close to measured values for as-received samples, but the difference is greater especially for the heat treated material at high temperature.

The calculated values indicate that the yield strength for the as-received materials should be lower than that of the heat treated material at both room temperature and 600 °C, whereas the measured values show that the opposite is true at 600 °C. This difference can be the result of an underestimated temperature sensitivity of some of the strengthening mechanisms or overlapping of the different components. Also, the equations used to calculate precipitation and solid solution strengthening disregard dislocation density and the amount of dislocation-obstacle interaction sites which might affect the strengthening effect and cause further inaccuracy [21].

The ratio of yield strengths at high temperature and room temperature is in good agreement with the results of Schneibel et al. for different ferritic alloys [110].

5.5 Utilizing η -phase to improve high-temperature creep resistance

5.5.1 Controlling the precipitation of η -phase

With the results and knowledge obtained via the previously described experiments and calculations, a new type of ferritic stainless steel was designed for use at very

high temperatures with good creep resistance based on η -phase precipitation. For an optimal microstructure, the amount and distribution of η -phase particles must be controlled and the nucleation of interfering Nb-containing carbonitrides considered. To do so, the alloying of elements present in η -phase, i.e. Nb, Si, Mo together with Ti, must be carefully balanced together with the annealing parameters, such as the maximum temperature and holding time. Furthermore, to achieve higher service temperatures, the solvus temperature of η -phase needs to increase. Thermo-Calc simulations showed that the solvus temperature of the η -phase can be increased in the range of 100 to 150 °C, by increasing the Nb content by 0.4 wt.% in the range of 0.35 to 1.0 wt.%. Also, increasing Si from 0.4 to 0.8 wt.% would increase the solvus temperature by another ~30 °C. When optimizing the amount of Ti in the steel, the precipitation of Ti-containing carbonitrides during casting should also be considered. The optimal amount of Ti is high enough to deplete the microstructure of free interstitials C and N to prevent Nb-containing carbonitrides from precipitating, thereby leaving Nb for precipitation of η -phase. To reduce the total amount of Ti needed, the interstitial C and N levels should be kept as low as possible. Ideally, enough Ti is alloyed when traces of Ti also precipitate in the η -phase, indicating that the amount of Ti-containing carbonitrides is high enough to largely deplete free C and N from the matrix. The equilibrium composition of the η -phase in the trial steel with 0.02C-0.02N-0.8Nb-0.8Si and 0.2 wt.% Ti is 46Nb-39Fe-11Cr-3Si-0.4Ti (wt.%) at temperatures above 850 °C. This can be considered close enough to the optimal in the current case.

After calculating the optimal alloy composition, experimental material was melted and cast. After hot rolling the material, as described in chapter 3.1, the annealing parameters were simulated and selected to achieve the target microstructure. Based on the TC-Prisma simulations and Gleeble heating curves, a significant amount of η -phase can be expected to precipitate during pre-annealing and in some amount during the cooling phase as well. Therefore, there are two things to consider when selecting the maximum pre-annealing temperature: i) the microstructure should be fully recrystallized and ii) previously precipitated η -phase should have dissolved to enable new precipitation on grain boundaries after recrystallization for enhanced creep resistance. The recrystallization temperature is also likely to be dependent on the dissolution temperature of η -phase due to the pinning effect of the particles distributed on grain boundaries, as described in chapter 2.1.1 [32], [33]. However, the temperature should be kept low enough to avoid extensive grain growth. The grain size should be small, around ASTM 6, to achieve good formability during manufacturing and high temperature strength,

although, ideally, the creep resistance could be increased with a larger grain size. In the pre-annealing stage, the grain size is not important since the material will be later cold rolled and finally annealed. After simulating the pre-annealing with peak temperatures between 950 and 1200 °C (Fig. 14), temperature of 1150 °C was selected so that all η -phase would dissolve, i.e. peak temperature would be safely above the η -phase solvus temperature (Fig. 42).

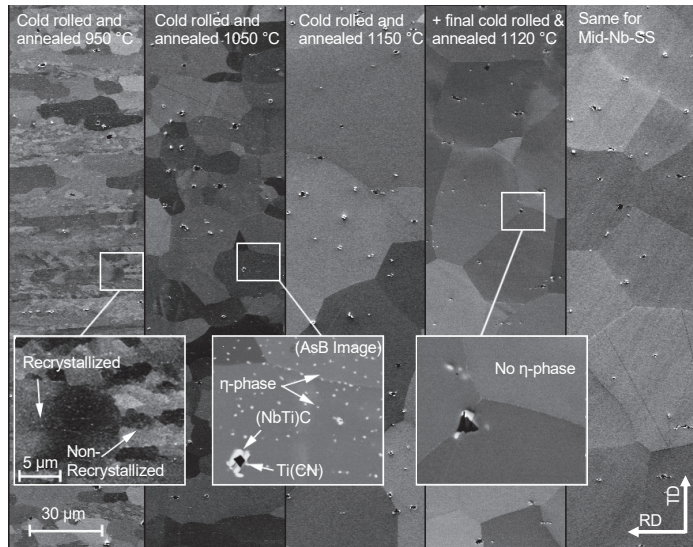


Fig. 42. FESEM secondary electron and backscatter images of samples after cold rolling and annealing at 950 °C, 1050 °C and 1150 °C, after final cold rolling and annealing at 1120 °C of High-Nb-SS and Mid-Nb-SS (Under CC BY Paper V © 2019 Authors).

The pre-annealing and cold rolling were followed by final annealing with parameters determined using a similar approach to when selecting pre-annealing parameters. However, for final annealing the grain size needs to be considered. In order to obtain a smaller grain size, a smaller temperature window is required for the maximum annealing temperature. The lowest temperature that resulted in a fully recrystallized microstructure was 1120 °C (Fig. 42). Some η -phase was still present in the microstructure after annealing at that temperature, and some grain growth was observed, but only a little. The grain size was 5.0 ASTM, which is slightly larger than the target of 6 ASTM. With more simulations using smaller temperature intervals, a better peak temperature could have been determined.

5.5.2 Improving creep resistance

Creep resistance is often decreased as the grain size decreases; however, in the present case, reasonably small grain size is important for other properties of the steel. Therefore, ways to reduce the active creep mechanisms, namely Coble creep and grain sliding, should be considered when aiming to increase creep resistance. The negative effect of fine grain size and grain boundary sliding is reduced when the grains are sufficiently covered by η -phase, which act as pinning points, resisting the grain boundary sliding, and perhaps as blocks to diffusional fluxes along the grain boundaries [9], [117].

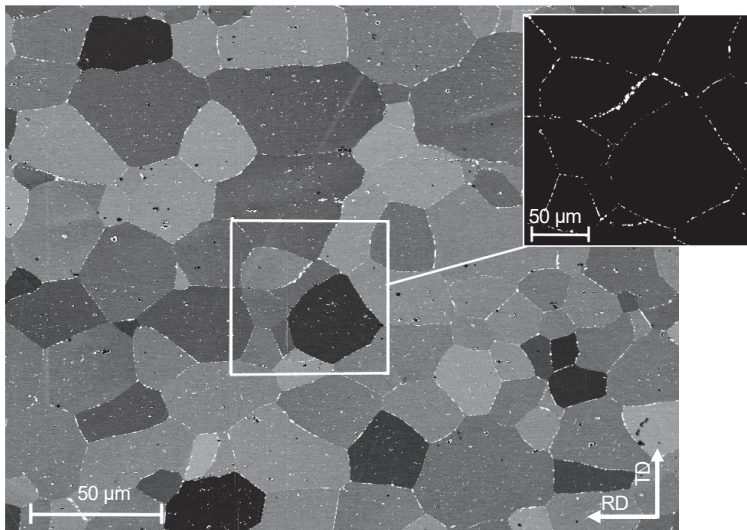


Fig. 43. FESEM backscatter image of High-Nb-SS sag test sample after 100 hours at 950 °C. Insets show grain boundary η -phase (0.77 wt.%) (Under CC BY Paper V © 2019 Authors).

Fig. 43 shows the microstructure of the High-Nb-SS sag test sample after 100 hours at 950 °C. It exhibited very good creep resistance under the prevailing low stress–high temperature conditions. The η -phase can be seen precipitated along the grain boundaries and within the grain as planned. The grain size of the High-Nb-SS at room temperature is slightly higher than in typical ferritic stainless steels (Table 1); however, at the test temperatures, grain growth occurs in most steels resulting in larger grain sizes than those that originally exist in the as-delivered material. The

grain size after the sag test at 950 °C was measured as 4-5 ASTM for High-Nb-SS, Mid-Nb-SS and EN 1.4622, and as 2 ASTM for EN 1.4509, while it was too large to be measured for EN 1.4521 and High-NbMo-SS (i.e. <0 ASTM). In High-Nb-SS, the negative effect of its fine grain size on creep resistance is mitigated by the precipitation of η -phase on grain boundaries, as previously explained.

The amount of η -phase might be high enough for the High-Nb-SS to retain good creep resistance even if the grain size was kept closer to the target size of ASTM 6 by annealing with a lower maximum temperature than used here. However, this would require more comprehensive simulations and tests with a smaller temperature interval between the tests than was used in this work. During the sag test, the dominant creep mechanism involves diffusion along grain boundaries presumably hindered by grain boundary η -phase; however, η -phase also precipitated within the grains, implying that good creep resistance might also be expected for higher stresses where other creep mechanisms are dominant. This should be examined with a creep test other than the sag test.

6 Summary and conclusions

The aim of this work was to understand the microstructural evolution in High-Cr, Nb and Ti dual stabilized ferritic stainless steels such as EN1.4509 and EN1.4521, during prolonged exposure at high temperatures. A comprehensive set of heat treatments at temperatures between 450 and 1050 °C were carried out using a Gleeble thermomechanical simulator as well as a conventional air furnace with heat treatment periods ranging from minutes up to 120 hours. The microstructure was then analysed using various techniques and methods, including FESEM, EDS, TEM and XRD. The microstructure evolution was also predicted with the aid of thermodynamic and kinetic simulations using Thermo-Calc and TC-Prisma software. It was observed that the MX type carbides and carbonitrides, (NbTi)C and Ti(CN), typically found in ferritic stainless steels, were already present in the as-received microstructure. Further heat treatments did not have any effect on the distribution, size or volume of these carbonitrides and carbides. However, heat treatments promoted the precipitation of η - and σ -phases. The composition, morphology and nucleation of η -phase precipitating was analysed.

To understand the effect of the microstructural changes occurring at high service temperatures (i.e. precipitation of intermetallic phases) on the yield strength of the steel, a complete breakdown of the various strengthening components was carried out. The strengthening mechanisms include friction stress, Hall-Petch grain boundary strengthening, Ashby-Orowan precipitation strengthening, solid solution strengthening and dislocation strengthening according to the Taylor equation.

Finally, the gathered data and knowledge on the precipitation of intermetallic phases in Ti and Nb dual stabilized ferritic stainless steels and its effect on steel properties was used to design a new ferritic stainless steel, based on the precipitation of the intermetallic η -phase, for use at very high temperatures. The volume fraction, distribution and composition of the η -phase and the grain size were optimized for good creep resistance and high temperature properties. The alloying elements Nb, Si and Ti were balanced with the aid of thermodynamic simulations to achieve a sufficient volume fraction and high enough solvus temperature of the η -phase. Further Gleeble thermomechanical simulations were carried out to determine the annealing parameters, i.e. peak temperature and holding time required to obtain both a fine grain size for good formability and the preferred grain boundary nucleation of the η -phase for enhanced creep resistance. The creep resistance of the new steel was compared to other commercial high-

temperature steels with a simple sag test performed at high temperatures. The following conclusions were made:

- The crystal structure of the η -phase was found to be hexagonal with calculated lattice parameters of $a = 0.474$ nm and $c = 0.774$ nm, which are very close to those reported in literature for Fe_2Mo -type η -phase.
- Based on comparison between the calculated and reported lattice parameters, it would appear that the presence of the substitutional elements Si and Nb do not have a significant effect on the lattice parameters. The chemical formula of the η -phase was identified as $(\text{FeCrSi})_2(\text{MoNb})$.
- The η -phase appeared in the microstructure of heat treated samples in two distinguishable morphologies: i) as equiaxed and typically larger particles and ii) as smaller plate-like particles. In addition, the plate-like η -phase particle had a distinct orientation relationship $[1\bar{1}02]_{\eta} // [011]_{\alpha}$ with the α -Fe matrix while the equiaxed particle had no orientation relationship with the matrix. The equiaxed particles are suggested to have nucleated and grown prior to reaching the as-delivered condition during the earlier processing of the steel in which recrystallization and grain growth left them located within grains with which they had no orientation relationship. The time of nucleation and the presence or absence of an orientation relationship with the matrix account for the different morphologies of the particles.
- To calculate the effect of η - and σ -phase precipitation on solid solution strengthening, the strengthening coefficient of Nb in α -Fe was required. As no proper value was to be found in the literature, the coefficient had to be first estimated. For this a regression analysis of known solid solution strengthening coefficients for various alloying elements in α -Fe was carried out on the basis of radius and modulus misfit. The resultant equation was used to estimate the solid solution strengthening coefficient of Nb as 16 MPa/at.% with a mean absolute deviation of 1.1 MPa/at.%. The results were coherent with the known coefficient for Nb in austenite (26 MPa/at.%).
- The contribution of Nb, Mo and Si to solid solution strengthening was calculated as 61 MPa in as-received and 41 MPa in heat treated samples, resulting in a 20 MPa decrease after heat treatment caused by the precipitation. This implies that the effect of precipitation strengthening exceeds the loss of solid solution strengthening during heat treatments carried out in this work. However, with prolonged heat treatments, precipitates will coarsen, resulting in a different relation between the mechanisms. The precipitation strengthening

- caused by the 0.60 wt.% η - and σ -phase in the as-received material was calculated as 150 MPa and, in the heat treated material, as 196 MPa with 4.73 wt.% of precipitated particles. Despite the significantly larger amount of particles in the heat treated sample, the strengthening due to precipitation increased only by 46 MPa due to the coarsening of the particles, therefore contributing less to the strengthening.
- The calculated total yield strength of the as-received and heat treated samples at room temperature were 425 and 461 MPa, respectively, which correlates well with the measured yield strengths of 406 and 425 MPa. This suggests that the magnitude of the Nb solid solution strengthening coefficient should be correct and can be considered as a good approximation considering the amount of Nb in solid is low. A number of approximations were made when combining all the strengthening components.
 - The yield strength before and after heat treatments was also measured at 600 °C. The calculated and experimentally measured values for as-received samples were very close, 195 MPa and 198 MPa respectively, but for the heat treated samples the calculations were less accurate, resulting in 232 MPa while the measured value was 183 MPa. This suggests that some of the assumptions made when calculating yield strength at high temperature are invalid, such as the scaling factors for solid solution strengthening coefficient and the rapid decrease of the friction stress. Finally, it should also be considered that the yield strength may not be a linear sum of strengthening mechanisms, and some mechanisms may overlap, which would explain why the calculated yield strength was higher than measured in most cases.
 - A trial High-Nb-SS steel with the composition 0.02C-0.02N-0.8Nb-0.8Si-0.2Ti (wt.%) was cast and manufactured. By alloying 0.8 wt.% Nb and Si, the equilibrium solvus temperature for η -phase is ~ 1050 °C, meaning that a higher temperature than that must be applied to dissolve all η -phase and for the rapid grain growth to begin increasing the possible service temperature of the steel. By alloying Ti, any interstitial C and N atoms precipitate as MX type Ti(CN) carbonitrides, leaving all of the Nb to freely precipitate as η -phase. Any additional free C and N will be precipitated with Nb as (NbTi)C. The amount of Ti that can be added in practice is limited by the need to avoid surface defects on the sheet as explained in chapter 2.1.1. However, it was shown that with the present C and N levels, by alloying 0.2 wt.% Ti (NbTi)C, precipitation was kept to a very low volume fraction.

- Annealing peak temperatures of 1120 and 1150 °C were selected with heating curves similar to plant-scale annealing processes. After annealing the microstructure was fully recrystallized with a low volume fraction of the η -phase on grain boundaries as preferred. The annealing temperature for a fully recrystallized microstructure is increased by the high content of Nb.
- The sag test results showed that the High-Nb-SS composition gave significantly higher creep resistance compared to the other steels. The measured deflection after testing at 950 °C was 0.5 mm, whereas the deflection was tenfold in the typical ferritic stainless steels used in high temperature applications
- Microstructure analysis after the sag test showed η -phase on grain boundaries. The creep mechanism active during the test was determined to be Coble creep, according to the deformation maps and considering calculated shear stress and homologous temperature. In Coble creep, the creep takes place via grain boundary diffusion and is inversely dependent on the grain size. Despite its finer grain size at the sag test temperatures, the deflections measured for High-Nb-SS were lower compared to other test materials, suggesting that the negative effect of its small grain size was mitigated, and creep resistance enhanced, by the η -phase on grain boundaries.

As recommendations for future work, the creep resistance in different test conditions, e.g. in a high stress condition, should be evaluated with comprehensive creep tests. Furthermore, long-term heat treatments and simulations should be carried out to understand whether the further coarsening of η -phase affects the creep resistance through the increased spacing between particles. Finally, it is suggested that the effect of η -phase on the impact toughness of the steels should be studied. The continuous network of precipitates on grain boundaries may present an easy path for fractures, and therefore the η -phase may decrease impact toughness, as reported in the literature (chapter 2.2.3). However, the materials in this thesis were only 2 mm thick and, according to the standard EN ISO 148-1:2016, below testable minimum thickness, which may result in inaccurate results due to out-of-plane bending of the sample during impact testing [118].

7 Novel features

The following observations are new to this thesis:

- Precipitation of atypical η -phase that includes molybdenum and silicon was observed. The phase was characterized as hexagonal C14 structured $(\text{FeCrSi})_2(\text{MoNb})$, with lattice parameters very close to those reported in the literature for Fe_2Mo -type η -phase. Therefore, the substitutional elements Si and Nb do not affect the lattice parameters significantly. Two types of morphology in η -phase particles were distinguished, which are due to differences in the orientation relationship between the particles and the matrix. It is suggested that this difference in coherence is a result of nucleation occurring during different stages of the steel processing. To our knowledge, the type of η -phase presented in the study is not well known, and its characterization is important for utilizing the phase to improve high-temperature strength and creep resistance.
- To estimate the effect of intermetallic phases on solid solution strengthening, a strengthening coefficient of Nb in α -Fe was determined from a regression analysis of the atomic size and modulus misfits of elements with known strengthening effects on the solid solution strengthening of b.c.c. iron. A value of 16 MPa/at.% with a mean absolute deviation of 1.1 MPa/at.% was obtained. To our knowledge, no reasonable estimation of the solid solution strengthening coefficient of Nb in α -Fe has been done, while it is important knowledge for controlling ambient and high temperature strength of Nb-alloyed ferritic steels.
- A new ferritic stainless steel was designed for very high temperatures with good creep resistance by utilizing the precipitation of η -phase. Instead of using a conventional trial and error approach, a comprehensive set of thermodynamic simulations were used to optimize the contents of alloying elements. The precipitation of η -phase on grain boundaries resulted in significantly better results in a simple sag creep test compared to commercially available steels used at high temperatures. Further tests regarding new ferritic stainless steels for very high temperatures are already in progress.

List of references

- [1] M. Hua, C. I. Garcia, A. J. DeArdo, and G. Tither, "Dual-stabilized ferritic stainless steels for demanding applications such as automotive exhaust systems," *Iron and Steelmaker (I and SM)*, vol. 24, no. 4. pp. 41–44, 1997.
- [2] Y. Inoue and M. Kikuchi, "Present and future trends of stainless steel for automotive exhaust system," *Nippon Steel Technical Report*, no. 88. pp. 62–69, 2003.
- [3] H. Ali-Löytty, P. Jussila, T. Juuti, L. P. Karjalainen, A. A. Zakharov, and M. Valden, "Influence of precipitation on initial high-temperature oxidation of Ti-Nb stabilized ferritic stainless steel SOFC interconnect alloy," *Int. J. Hydrogen Energy*, vol. 37, no. 19, pp. 14528–14535, 2012.
- [4] N. Fujita, K. Ohmura, M. Kikuchi, T. Suzuki, S. Funaki, and I. Hiroshige, "Effect of Nb on high-temperature properties for ferritic stainless steel," *Scr. Mater.*, vol. 35, no. 6, pp. 705–710, Sep. 1996.
- [5] J. Douthett, "Automotive exhaust system corrosion," in *Corrosion: environments and industries*, S. D. Cramer and B. S. J. Covino, Eds. ASM International, 2006, pp. 519–530.
- [6] K. Ishii, A. Miyazaki, and S. Satoh, "Stainless steels for automotive exhaust systems," *Kawasaki Steel Tech. Rep.*, pp. 39–41, 1999.
- [7] N. Fujita, "New ferritic stainless steels in automotive exhaust system," *Nippon Steel Technical Report*, pp. 29–33, 2000.
- [8] H. Yan, H. Bi, X. Li, and Z. Xu, "Precipitation and mechanical properties of Nb-modified ferritic stainless steel during isothermal aging," *Mater. Charact.*, vol. 60, no. 3, pp. 204–209, 2009.
- [9] F. Abe, "Effect of fine precipitation and subsequent coarsening of Fe₂W laves phase on the creep deformation behavior of tempered martensitic 9Cr-W steels," *Metall. Mater. Trans. A*, vol. 36, no. 2, pp. 321–332, Feb. 2005.
- [10] W. Wang, B. Liu, and V. Kodur, "Effect of temperature on strength and elastic modulus of high-strength steel," *J. Mater. Civ. Eng.*, vol. 25, no. 2, pp. 174–182, Feb. 2013.
- [11] F. Liu, M. Rashidi, L. Johansson, J. Hald, and H.-O. Andrén, "A new 12% chromium steel strengthened by Z-phase precipitates," *Scr. Mater.*, vol. 113, pp. 93–96, Mar. 2016.
- [12] M. I. Isik, A. Kostka, V. A. Yardley, K. G. Pradeep, M. J. Duarte, P. P. Choi, D. Raabe, and G. Eggeler, "The nucleation of Mo-rich Laves phase particles adjacent to M 23 C 6 micrograin boundary carbides in 12% Cr tempered martensite ferritic steels," *Acta Mater.*, vol. 90, pp. 94–104, May 2015.
- [13] H. Cui, F. Sun, K. Chen, L. Zhang, R. Wan, A. Shan, and J. Wu, "Precipitation behavior of Laves phase in 10%Cr steel X12CrMoWVNbN10-1-1 during short-term creep exposure," *Mater. Sci. Eng. A*, vol. 527, no. 29–30, pp. 7505–7509, Nov. 2010.
- [14] H. Ali-Löytty, M. Hannula, T. Juuti, Y. Niu, A. A. Zakharov, and M. Valden, "The role of (FeCrSi)₂(MoNb)-type Laves phase on the formation of Mn-rich protective

- oxide scale on ferritic stainless steel,” *Corros. Sci.*, vol. 132, pp. 214–222, 2018.
- [15] J. Froitzheim, G. H. Meier, L. Niewolak, P. J. Ennis, H. Hattendorf, L. Singheiser, and W. J. Quadakkers, “Development of high strength ferritic steel for interconnect application in SOFCs,” *J. Power Sources*, vol. 178, no. 1, pp. 163–173, 2008.
- [16] J. H. Schneibel and M. Heilmaier, “Hall & Petch breakdown at elevated temperatures,” *Mater. Trans.*, vol. 55, no. 1, pp. 44–51, 2014.
- [17] E. S. Puchi-Cabrera, J. D. Guérin, D. Barbier, M. Dubar, and J. Lesage, “Plastic deformation of structural steels under hot-working conditions,” *Mater. Sci. Eng. A*, vol. 559, pp. 268–275, Jan. 2013.
- [18] Q. Lu, W. Xu, and S. Van Der Zwaag, “Designing new corrosion resistant ferritic heat resistant steel based on optimal solid solution strengthening and minimisation of undesirable microstructural components,” *Comput. Mater. Sci.*, vol. 84, pp. 198–205, 2014.
- [19] S. M. C. Van Bohemen, “The nonlinear lattice expansion of iron alloys in the range 100–1600 K,” *Scr. Mater.*, vol. 69, no. 4, pp. 315–318, 2013.
- [20] Q. Yu, Z. Wang, X. Liu, and G. Wang, “Effect of microcontent Nb in solution on the strength of low carbon steels,” *Mater. Sci. Eng. A*, vol. 379, no. 1–2, pp. 384–390, 2004.
- [21] A. G. Kostryzhev, O. O. Marenych, C. R. Killmore, and E. V. Pereloma, “Strengthening mechanisms in thermomechanically processed NbTi-microalloyed steel,” *Metall. Mater. Trans. A Phys. Metall. Mater. Sci.*, vol. 46, no. 8, pp. 3470–3480, 2015.
- [22] A. F. Padilha, R. Lesley, and P. R. Rios, “Stainless steels heat treatment,” in *Steel Heat Treatment Handbook*, Second Edi., G. E. Totten, Ed. CRC Press, 2006, p. 1576.
- [23] J. Grubb, R. Wrigth, J. Farrar, P, and R. Wright, “Toughness of ferritic stainless steels,” in *Toughness of Ferritic Stainless Steels*, R. Lula, Ed. West Conshohocken: ASTM International, 1980, pp. 2–32.
- [24] R. D. Campbell, “Ferritic stainless steel welding metallurgy,” *Key Eng. Mater.*, vol. 69–70, pp. 167–216, Jan. 1992.
- [25] J. F. Almagro, X. Llovet, M. Auxiliadora Heredia, C. Luna, and R. Sánchez, “Soluble fraction of stabilising elements in ferritic stainless steel,” *Microchim. Acta*, vol. 161, no. 3–4, pp. 323–327, Jun. 2008.
- [26] A. H. Cottrell and B. A. Bilby, “Dislocation theory of yielding and strain ageing of iron,” *Proc. Phys. Soc. Sect. A*, vol. 62, no. 1, pp. 49–62, Jan. 1949.
- [27] R. E. Hook and J. A. Elias, “The effects of composition and annealing conditions on the stability of columbium (niobium)-treated low-carbon steels,” *Metall. Trans.*, vol. 3, no. 8, pp. 2171–2181, Aug. 1972.
- [28] T. Gladman, *The Physical Metallurgy of Microalloyed Steels*, 1st ed. London: Ashgate Publishing, 1997.
- [29] K. F. Krysiak, J. Grubb, B. Pollard, and R. D. Campbell, “Selection of wrought ferritic stainless steels,” in *ASM Handbook, volume 6: Welding, brazing, and soldering*, 10th ed., D. L. Olson, T. A. Siewert, S. Liu, and G. R. Edwards, Eds. ASM International, 1993, pp. 441–455.

- [30] J. Redmond, "Toughness of 18Cr-2Mo stainless steel," in *Toughness of ferritic stainless steels*, 1st ed., R. . Lula, Ed. West Conshohocken: ASTM International, 1980, pp. 123–144.
- [31] K. Hio, M. Tsutsui, and Y. Hosoi, "Electrochemical characteristics of chromium-saving ferritic stainless steel," *Corrosion*, vol. 55, no. 9, pp. 822–824, Sep. 1999.
- [32] M. Suehiro, Z.-K. Liu, and J. Ågren, "Effect of niobium on massive transformation in ultra low carbon steels: a solute drag treatment," *Acta Mater.*, vol. 44, no. 10, pp. 4241–4251, Oct. 1996.
- [33] M. Suehiro, "Recrystallization and related phenomena. An analysis of the solute drag effect of Nb on recrystallization of ultra low carbon steel.," *ISIJ Int.*, vol. 38, no. 6, pp. 547–552, 1998.
- [34] P. L. Gruzin, "Certain laws of diffusion and distribution of elements in alloys," *Met. Sci. Heat Treat. Met.*, vol. 2, no. 10, pp. 525–532, 1960.
- [35] S. Hironaka, T. Hiroshi, and M. Takashi, "Effect of Si on mechanical property of galvanized dual phase steel," *Mater. Sci. Forum*, vol. 638, pp. 3260–3265, 2010.
- [36] C.-O. A. Olsson and D. Landolt, "Passive films on stainless steels-chemistry, structure and growth," *Electrochim. Acta*, vol. 48, no. 9, pp. 1093–1104, Apr. 2003.
- [37] T. Hanawa, S. Hiromoto, A. Yamamoto, D. Kuroda, and K. Asami, "XPS characterization of the surface oxide film of 316L stainless steel samples that were located in quasi-biological environments," *Mater. Trans.*, vol. 43, no. 12, pp. 3088–3092, 2002.
- [38] D. A. Porter and K. E. Easterling, *Phase transformations in metals and alloys*, 3rd ed. London: CRC Press, 2009.
- [39] N. Fujita, M. Kikuchi, and H. K. D. H. Bhadeshia, "Modeling M6C precipitation in niobium-alloyed ferritic stainless steel," *Metall. Mater. Trans. A*, vol. 33, no. 11, pp. 3339–3347, Nov. 2002.
- [40] H. K. D. H. Bhadeshia, "Advances in the kinetic theory of carbide precipitation," *Mater. Sci. Forum*, vol. 426–432, pp. 35–42, Aug. 2003.
- [41] J. Svoboda, F. D. Fischer, P. Fratzl, and E. Kozeschnik, "Modelling of kinetics in multi-component multi-phase systems with spherical precipitates," *Mater. Sci. Eng. A*, vol. 385, no. 1–2, pp. 166–174, Nov. 2004.
- [42] Q. Chen, H. J. Jou, and G. Sterner, "TC-PRISMA user's guide." Thermo-Calc Software AB, Stockholm, p. 29, 2015.
- [43] C. C. Silva, J. P. Farias, H. C. Miranda, R. F. Guimarães, J. W. A. Menezes, and M. A. M. Neto, "Microstructural characterization of the HAZ in AISI 444 ferritic stainless steel welds," *Mater. Charact.*, vol. 59, no. 5, pp. 528–533, 2008.
- [44] W. Gordon and A. Van Bennekom, "Review of stabilisation of ferritic stainless steel," *Mater. Sci. Technol.*, vol. 12, pp. 126–131, 1996.
- [45] J. Charles, J. D. Mithieux, P. O. Santacreu, and L. Peguet, "The ferritic stainless steel family : the appropriate answer to nickel volatility," *Rev. Métallurgie*, vol. 106, no. 3, pp. 124–139, 2009.
- [46] Y. Murata, M. Kamiya, T. Kunieda, A. M. Abdel-Daiem, T. Koyama, M. Morinaga, and R. Hashizume, "Dependence of solvus temperature of the Laves phase on

- (Mo+W+Re) contents in high cr ferritic steels,” *ISIJ Int.*, vol. 45, no. 1, pp. 101–106, 2005.
- [47] C.-C. Hsieh and W. Wu, “Overview of intermetallic sigma phase precipitation in stainless steels,” *ISRN Metall.*, vol. 2012, no. 4, pp. 1–16, 2012.
- [48] W. Xu, D. San Martin, P. E. J. Rivera Díaz del Castillo, and S. van der Zwaag, “Modelling and characterization of chi-phase grain boundary precipitation during aging of Fe-Cr-Ni-Mo stainless steel,” *Mater. Sci. Eng. A*, vol. 467, no. 1–2, pp. 24–32, 2007.
- [49] D. M. Escriba, E. Materna-Morris, R. L. Plaut, and A. F. Padilha, “Chi-phase precipitation in a duplex stainless steel,” *Mater. Charact.*, vol. 60, no. 11, pp. 1214–1219, 2009.
- [50] K. W. Chan and S. C. Tjong, “Effect of secondary phase precipitation on the corrosion behavior of duplex stainless steels,” *Materials (Basel)*, vol. 7, no. 7, pp. 5268–5304, 2014.
- [51] R. L. Fleischer and J. H. Westbrook, *Intermetallic compounds - Principles and practice, volume 3: Progress*. Chichester, UK: John Wiley & Sons, Ltd, 2002.
- [52] C. T. Liu, J. H. Zhu, M. P. Brady, C. G. McKamey, and L. M. Pike, “Physical metallurgy and mechanical properties of transition-metal Laves phase alloys,” *Intermetallics*, vol. 8, no. 9–11, pp. 1119–1129, Sep. 2000.
- [53] K. W. Andrews, D. J. Dyson, and S. R. Keown, *Interpretation of Electron Diffraction Patterns*, 1st ed. Boston, MA: Springer US, 1967.
- [54] E. L. Brown, M. E. Burnett, P. T. Purtscher, and G. Krauss, “Intermetallic phase formation in 25Cr-3Mo-4Ni ferritic stainless steel,” *Metall. Trans. A*, vol. 14, no. 4, pp. 791–800, Apr. 1983.
- [55] A. Malfliet, F. Mompiau, F. Chassagne, J.-D. Mithieux, B. Blanpain, and P. Wollants, “Precipitation in Nb-stabilized ferritic stainless steel investigated with in-situ and ex-situ transmission electron microscopy,” *Metall. Mater. Trans. A*, vol. 42, no. 11, pp. 3333–3343, Jun. 2011.
- [56] G. M. Sim, J. C. Ahn, S. C. Hong, K. J. Lee, and K. S. Lee, “Effect of Nb precipitate coarsening on the high temperature strength in Nb containing ferritic stainless steels,” *Mater. Sci. Eng. A*, vol. 396, no. 1–2, pp. 159–165, 2005.
- [57] D. G. Morris, M. A. Muñoz-Morris, and C. Baudin, “The high-temperature strength of some Fe₃Al alloys,” *Acta Mater.*, vol. 52, no. 9, pp. 2827–2836, 2004.
- [58] N. Fujita, K. Ohmura, and A. Yamamoto, “Changes of microstructures and high temperature properties during high temperature service of niobium added ferritic stainless steels,” *Mater. Sci. Eng. A*, vol. 351, no. 1–2, pp. 272–281, 2003.
- [59] G. Speich, “Precipitation of Laves phases from iron-niobium (columbium) and iron-titanium solid solutions,” *Trans. Met. Soc. AIME*, vol. 224, no. 8, pp. 850–858, 1962.
- [60] G. J. Cocks and D. W. Borland, “The orientation relationship and morphology of Fe₂Nb precipitates in ferrite,” *Met. Sci.*, vol. 9, no. 1, pp. 384–389, Jan. 1975.
- [61] A. H. Cottrell, “Symposium on relation of properties to microstructure,” 1954, p. 131.
- [62] O. D. Turnbull, “Impurities and imperfections,” in *36th metal congress and*

- exposition, 1955, pp. 121–44.
- [63] J. P. Hirth and J. Lothe, *Theory of dislocations*, 2nd ed. New York: Wiley, 1982.
- [64] R. W. Hertzberg, *Deformation and fracture mechanics of engineering materials*, 3rd ed. Hoboken, New Jersey: Wiley, 1989.
- [65] N. J. Cracknell, A., Petch, “Frictional forces on dislocation arrays at the lower yield point in iron,” *Acta Metall.*, vol. 3, no. 2, pp. 186–189, 1955.
- [66] D. Hull and D. J. Bacon, *Introduction to Dislocations*, 5th ed. Elsevier, 2011.
- [67] R. L. Fleischer, “Substitutional solution hardening,” *Acta Metall.*, vol. 11, no. 3, pp. 203–209, Mar. 1963.
- [68] M. Z. B. Feltham, “Solid-solution hardening,” *J. Mater. Sci.*, vol. 28, no. 10, pp. 2557–2576, 1993.
- [69] A. J. E. Foreman and M. J. Makin, “Dislocation movement through random arrays of obstacles,” *Philos. Mag.*, vol. 14, no. 131, pp. 911–924, Oct. 1966.
- [70] U. F. Kocks, “A statistical theory of flow stress and work-hardening,” *Philos. Mag.*, vol. 13, no. 123, pp. 541–566, Mar. 1966.
- [71] G. I. Taylor, “The mechanism of plastic deformation of crystals. Part I. Theoretical,” *Proc. R. Soc. A Math. Phys. Eng. Sci.*, vol. 145, no. 855, pp. 362–387, Jul. 1934.
- [72] F. F. Lavrentev, “The type of dislocation interaction as the factor determining work hardening,” *Mater. Sci. Eng.*, vol. 46, no. 2, pp. 191–208, Dec. 1980.
- [73] K. M. Davoudi and J. J. Vlassak, “Dislocation evolution during plastic deformation: equations vs. discrete dislocation simulations,” no. 1934, pp. 1–23, 2014.
- [74] S. J. Basinski and Z. S. Basinski, “Plastic deformation and work hardening,” in *Dislocations in solids*, 1st ed., F. R. N. Nabarro and J. P. Hirth, Eds. Amsterdam: Elsevier B.V., 2004, pp. 261–363.
- [75] E. J. Mittemeijer, *Fundamentals of materials science*, 1st ed. Berlin: Springer-Verlag Berlin Heidelberg, 2011.
- [76] J. Čadek, *Creep in metallic materials*, 2nd ed. Oxford: Elsevier science & technology, 1989.
- [77] S. J. Zinkle and G. E. Lucas, “Deformation and fracture mechanisms in irradiated FCC and BCC metals,” Oak Ridge, 2003.
- [78] H. J. Frost and M. F. Ashby, *Deformation-mechanism maps: the plasticity and creep of metals and ceramics*, 1st ed. Amsterdam: Pergamon Press, 1982.
- [79] H. J. Frost and M. F. Ashby, “Deformation-mechanism maps for pure iron, two austenitic stainless steels, and a low-alloy ferritic steel,” in *Fundamental Aspects of Structural Alloy Design*, R. I. Jaffee and B. A. Wilcox, Eds. Boston, MA: Springer US, 1977, pp. 27–65.
- [80] ASTM E112-12, *Standard Test Methods for Determining Average Grain Size*. West Conshohocken: ASTM International, 2012.
- [81] D. Rojas, J. Garcia, O. Prat, C. Carrasco, G. Sauthoff, and A. R. Kaysser-Pyzalla, “Design and characterization of microstructure evolution during creep of 12% Cr heat resistant steels,” *Mater. Sci. Eng. A*, vol. 527, no. 16–17, pp. 3864–3876, Jun. 2010.
- [82] A. Schneider and G. Inden, “Simulation of the kinetics of precipitation reactions in

- ferritic steels,” *Acta Mater.*, vol. 53, no. 2, pp. 519–531, Jan. 2005.
- [83] J. D. Verhoeven, *Fundamentals of physical metallurgy*, 1st ed. Michigan: John Wiley & Sons, Ltd, 1975.
- [84] D. Ouden, F. J. Vermolen, L. Zhao, C. Vuik, and J. Sietsma, “Mathematical modelling of NbC particle nucleation and growth in an HSLA steel under elastic deformation,” *Solid State Phenom.*, vol. 172–174, pp. 893–898, 2011.
- [85] B. Willenberg and LA Dempere, “Overview of microanalysis techniques for the characterization of concrete and cement materials,” *Microsc. Microanal.*, vol. 16, no. S2, pp. 944–945, Jul. 2010.
- [86] ASTM E963 - 95, *Standard practice for electrolytic extraction of phases from Ni and Ni-Fe base superalloys using a hydrochloric-methanol electrolyte*. West Conshohocken: ASTM International, 2000.
- [87] S. R. E. Williamson G. K., “Dislocation densities in some annealed and cold-worked metals from measurements on the X-ray Debye-Scherrer spectrum,” *Philos. Mag.*, vol. 1, no. 1, pp. 34–46, 1956.
- [88] H. M. Rietveld, “A Profile refinement method for nuclear and magnetic structures,” *J. Appl. Crystallogr.*, vol. 2, no. 2, pp. 65–71, Jun. 1969.
- [89] S. J. Lee and Y. K. Lee, “Quantitative analyses of ferrite lattice parameter and solute Nb content in low carbon microalloyed steels,” *Scr. Mater.*, vol. 52, no. 10, pp. 973–976, 2005.
- [90] F. Yin, T. Hanamura, O. Umezawa, and K. Nagai, “Phosphorus-induced dislocation structure variation in the warm-rolled ultrafine-grained low-carbon steels,” *Mater. Sci. Eng. A*, vol. 354, no. 1–2, pp. 31–39, 2003.
- [91] A. G. Kostryzhev, A. Al Shahrani, C. Zhu, J. M. Cairney, S. P. Ringer, C. R. Killmore, and E. V. Pereloma, “Effect of niobium clustering and precipitation on strength of an NbTi-microalloyed ferritic steel,” *Mater. Sci. Eng. A*, vol. 607, pp. 226–235, 2014.
- [92] F. Yin, T. Hanamura, T. Inoue, and K. Nagai, “Fiber texture and substructural features in the caliber-rolled low-carbon steels,” *Metall. Mater. Trans. A*, vol. 35, no. February, pp. 665–677, 2004.
- [93] T. Ono, Y. Tomota, P. Lukas, D. Lugovy, D. Neov, N. Tsuchida, and K. Nagai, “In situ neutron diffraction during tensile straining of fine grained ferrite - pearlite steel,” *Mater. Sci. Technol.*, vol. 20, no. 1, pp. 121–125, Jan. 2004.
- [94] A. G. Kostryzhev, M. Strangwood, and C. L. Davis, “Mechanical property development during UOE forming of large diameter pipeline steels,” *Mater. Manuf. Process.*, vol. 25, no. 1–3, pp. 41–47, 2010.
- [95] EN 10 002-1, *Tensile testing of metallic materials. Method of test at ambient temperature*. London: BSI, 2001.
- [96] Y. Kato, M. Ito, Y. Kato, and O. Furukimi, “Effect of Si on precipitation behavior of Nb-Laves phase and amount of Nb in solid solution at elevated temperature in high purity 17%Cr-0.5%Nb steels,” *Mater. Trans.*, vol. 51, no. 9, pp. 1531–1535, 2010.
- [97] P. Klug, Harold and E. Alexander, Leeroy, *X-ray diffraction procedures for*

- polycrystalline and amorphous materials*. New York: John Wiley & Sons, 1974.
- [98] B. D. Cullity and S. R. Stock, *Elements of X-ray Diffraction*, 3rd ed. New York: Prentice-Hall, 2001.
- [99] V. Kuzucu, M. Aksoy, M. H. Korkut, and M. M. Yildirim, "The effect of niobium on the microstructure of ferritic stainless steel," *Mater. Sci. Eng. A*, vol. 230, no. 1–2, pp. 75–80, 1997.
- [100] D. I. Bardos, K. P. Gupta, and P. A. Beck, "Ternary Laves phases with transition elements and silicon," *Trans. Met. Soc. AIME*, vol. 221, pp. 1–2, 1961.
- [101] A. Iseda, H. Teranishi, and K. Yoshikawa, "Effects of silicon and molybdenum on long-term heating embrittlement and precipitation of Laves phase of high chromium ferritic heat resistant steels," *Tetsu-to-Hagane*, vol. 76, no. 12, pp. 2190–2197, 1990.
- [102] A. F. Padilha, I. F. Machado, and R. L. Plaut, "Microstructures and mechanical properties of Fe–15% Cr–15% Ni austenitic stainless steels containing different levels of niobium additions submitted to various processing stages," *J. Mater. Process. Technol.*, vol. 170, no. 1–2, pp. 89–96, Dec. 2005.
- [103] N. Boutarek, S. Mansour, S. E. Amara, and R. Kesri, "Phase transition in the Fe–V system," *Int. J. Mater. Res.*, vol. 99, no. 3, pp. 301–306, Mar. 2008.
- [104] "JCPDS Databases." International Centre for Diffraction Data, Newtown Square, PA, 2000.
- [105] S. S. M. Tavares, J. A. de Souza, L. F. G. Herculano, H. F. G. de Abreu, and C. M. de Souza, "Microstructural, magnetic and mechanical property changes in an AISI 444 stainless steel aged in the 560°C to 800°C range," *Mater. Charact.*, vol. 59, no. 2, pp. 112–116, 2008.
- [106] K. Östman, M. Isakov, T. Nyssönen, and V. Kuokkala, "Temperature and strain rate effects on the mechanical behavior of ferritic stainless steels," in *Conference proceedings of the society for experimental mechanics series*, 2014, pp. 161–166.
- [107] A. Yilmaz, "The Portevin–Le Chatelier effect: a review of experimental findings," *Sci. Technol. Adv. Mater. 12 063001 Sci. Technol. Adv. Mater.*, vol. 12, no. 6, pp. 1–16, 2011.
- [108] S. Takaki, K. Kawasaki, Y. Futamura, and T. Tsuchiyama, "Deformation behavior of ultrafine grained iron," *Mater. Sci. Forum*, vol. 503–504, pp. 317–322, 2006.
- [109] K. Takeda, N. Nakada, T. Tsuchiyama, and S. Takaki, "Effect of interstitial elements on Hall–Petch coefficient of ferritic iron," *ISIJ Int.*, vol. 48, no. 8, pp. 1122–1125, 2008.
- [110] J. H. Schneibel, M. Heilmaier, W. Blum, G. Hasemann, and T. Shanmugasundaram, "Temperature dependence of the strength of fine- and ultrafine-grained materials," *Acta Mater.*, vol. 59, no. 3, pp. 1300–1308, 2011.
- [111] L. Jian, S. Fuyu, and X. WenChong, "On the evaluation of yield strength for microalloyed steels," *Scr. Metall. Mater.*, vol. 24, no. 7, pp. 1393–1398, Jul. 1990.
- [112] Y. Bergström, Y. Granbom, and D. Sterkenburg, "A dislocation-based theory for the deformation hardening behavior of DP steels: impact of martensite content and ferrite grain size," *J. Metall.*, vol. 2010, pp. 1–16, 2010.
- [113] H. Abrams, G. Maniar, D. Nail, and H. Solomon, "Session, summary—stainless

- steels,” in *MiCon 78: optimization of processing, properties, and service performance through microstructural control*, 1979, pp. 261–262.
- [114] D. Brunner and J. Diehl, “The effect of atomic lattice defects on the softening phenomena of high-purity α -Iron,” *Phys. status solidi*, vol. 160, no. 2, pp. 355–372, Apr. 1997.
- [115] A. Seeger, “The flow stress of high-purity refractory body-centred cubic metals and its modification by atomic defects,” *J. Phys. Iv*, vol. 5, no. C7, pp. 45–65, 1995.
- [116] P. L. Raffo, “Yielding and fracture in tungsten and tungsten-rhenium alloys,” *J. Less Common Met.*, vol. 17, no. 2, pp. 133–149, Feb. 1969.
- [117] C. Prudhomme, P.-O. Santacreu, I. Evenepoel, and B. Proutl, “Thermomechanical fatigue behaviour of ferritic stainless steel grades for high temperatures applications,” *MATEC Web Conf.*, vol. 165, p. 16003, May 2018.
- [118] EN ISO 148-1:2016, “Charpy pendulum impact test — Part 1: Test method,” in *Metallic materials*, 2nd ed., Geneva: ISO, 2009, p. 26.

Original publications

- I Juuti, T.J., Karjalainen, L.P., & Heikkinen, E.-P., (2012) Precipitation of Si and its influence on mechanical properties of type 441 stainless steel, *Advanced Materials Research*, 409, 690-695.
- II Juuti, T., Karjalainen, P., Rovatti, L., Heikkinen, E.-P. & Pohjanne, P. (2011) Contribution of Mo and Si to laves-phase precipitation in type 444 steel and its effect on steel properties, In *Proceedings: 7th European Stainless Steel Conference – Science and Market, Como, Italy 21 – 23.9.2011* Associazione Italiana di Metallurgia AIM.
- III Juuti, T., Rovatti, L., Mäkelä, A., Karjalainen, L.P., & Porter D., (2014) Influence of long heat treatments on the laves phase nucleation in a type 444 ferritic stainless steel, *Journal of Alloys and Compounds*, 616, 250-256.
- IV Juuti, T., Rovatti, L., Porter, D., Angella, G., & Kömi, J., (2018) Factors controlling ambient and high temperature yield strength of ferritic stainless steel susceptible to intermetallic phase formation, *Materials Science and Engineering A*, 726, 45-55.
- V Juuti, T., Manninen, T., Uusikallio, S., Kömi, J., & Porter, D., (2019) New ferritic stainless steel for service temperatures up to 1050 °C utilizing intermetallic phase transformation, *Metals*, 9(6), 664.

Reprinted with permission from Trans Tech Publications Ltd. (I), Associazione Italiana Di Metallurgia AIM (II), Elsevier B.V. (III and IV) and under Creative Commons CC BY license from Authors (V).

Original publications are not included in the electronic version of the dissertation.

725. Bergna, Davide (2019) Activated carbon from renewable resources : carbonization, activation and use
726. Nuottila, Jouko (2019) Flexibility in agile projects : contracting practices and organisational arrangements
727. Adesanya, Elijah D. (2019) A cementitious binder from high-alumina slag generated in the steelmaking process
728. Hannila, Hannu (2019) Towards data-driven decision-making in product portfolio management : from company-level to product-level analysis
729. Saastamoinen, Ari (2020) Processing and microstructure of direct-quenched and tempered ultra-high strength steels
730. Ashraf, Muhammad Ikram (2019) Radio resource management in device-to-device and vehicle-to-vehicle communication in 5G networks and beyond
731. Elbamby, Mohammed S. (2019) Flexible duplexing and resource optimization in small cell networks
732. Ruokamo, Henna (2019) Time-gating technique for a single-photon detection-based solid-state time-of-flight 3D range imager
733. Piñero, Pablo (2019) The metabolism of socio-economic systems : combination of input-output analysis and material flow accounting for footprint-type indicators
734. Mahmood, Shahriare (2020) The substantive approach for managing demand and supply sustainably in fashion industry
735. Laukka, Alekski (2020) The effects of microalloying on the scale formation of AISI 304 stainless steel in walking beam furnace conditions
736. Ali, Samad (2020) Learning-based predictive resource allocation for machine type communications
737. Vatjus-Anttila, Jarkko (2020) Energy efficient rendering of extensible 3D virtual environments on mobile devices
738. Wijewardhana, Uditha (2020) Sparse recovery algorithms for streaming and multidimensional signals
739. Li, Panpan (2020) Deep eutectic solvents in the production of wood-based nanomaterials
740. Nuortimo, Kalle (2020) Public acceptance in energy technology development and deployment : Opinion mining case study

S E R I E S E D I T O R S

A
SCIENTIAE RERUM NATURALIUM
University Lecturer Tuomo Glumoff

B
HUMANIORA
University Lecturer Santeri Palviainen

C
TECHNICA
Postdoctoral researcher Jani Peräntie

D
MEDICA
University Lecturer Anne Tuomisto

E
SCIENTIAE RERUM SOCIALIUM
University Lecturer Veli-Matti Ulvinen

E
SCRIPTA ACADEMICA
Planning Director Pertti Tikkanen

G
OECONOMICA
Professor Jari Juga

H
ARCHITECTONICA
University Lecturer Anu Soikkeli

EDITOR IN CHIEF
University Lecturer Santeri Palviainen

PUBLICATIONS EDITOR
Publications Editor Kirsti Nurkkala

ISBN 978-952-62-2565-4 (Paperback)
ISBN 978-952-62-2566-1 (PDF)
ISSN 0355-3213 (Print)
ISSN 1796-2226 (Online)